Lee waves and wake generated by a steady current passing over a spherical cap, comparing linear, numerical and experimental approaches

Cruz Garcia Molina

THÈSE

Pour obtenir le grade de

DOCTEUR DE L'UNIVERSITÉ GRENOBLE ALPES

Spécialité : Océan, Atmosphère, Hydrologie

Arrêté ministériel : 25 mai 2016

Présentée par

Cruz GARCIA MOLINA

Thèse dirigée par **Chantal STAQUET**, Professeur

préparée au sein du **Laboratoire Laboratoire des Ecoulements Géophysiques et Industriels**
dans **l'École Doctorale Terre, Univers, Environnement**

Ondes de relief et sillage générés par un courant passant au-dessus d'une calotte sphérique : approches linéaire, numérique et expérimentale

Lee waves and wake generated by a steady current passing over a spherical cap, comparing linear, numerical and experimental approaches

Thèse soutenue publiquement le **4 septembre 2020**,
devant le jury composé de :

Madame CHANTAL STAQUET
PROFESSEUR DES UNIVERSITES, UNIVERSITE GRENOBLE ALPES, Directrice de thèse
Madame CAROLINE MULLER
CHARGE DE RECHERCHE HDR, CNRS ILE-DE-FRANCE GIF-SUR-YVETTE, Rapportrice
Monsieur PATRICE LE GAL
DIRECTEUR DE RECHERCHE, CNRS DELEGATION PROVENCE ET CORSE, Rapporteur
Monsieur HENRI-CLAUDE NATAF
DIRECTEUR DE RECHERCHE, CNRS DELEGATION ALPES, Président
Monsieur JULIEN LE SOMMER
CHARGE DE RECHERCHE CNRS, CNRS DELEGATION ALPES, Examinateur

Acknowledgments

First, I thank the people who have been there since the beginning: my parents. Thanks for pushing me to dream and for encouraging me to pursue those dreams. You are kind of my friends, but you don't waste a chance to teach me right from wrong. Thanks for that! To my sweet young sister, we lived many crazy-good things together, didn't we? I thank you for teaching me how to enjoy a joke, and how to see life as one.

I thank the person who is responsible for most of my good days and who helps me find my way in the gray ones: my lovely wife, Perla. Now that my family has grown, I have a new motivation to keep moving forward. To my little boy: no matter what happens, your smile, your hugs, and your big wet baby kisses make my day. Thanks, Crucito.

I want to make an especial mention to: my Granny, thanks for teaching us how to live every second of life. Hey Marco: we enjoyed, played, fought, joked a lot; but it was not enough! I thank all my aunts and uncles for always being there. Uncle Cesar... I miss you... Hey! aunt Mily, thanks for helping me improve my bad English. I thank you, and my aunt Ana not only for being my aunts but for being my friends.

To all my friends: Thibault, Géraldine, Miguel, Julian, Laura, Lucas, Enzo, Christophe, Sara, Kristen, Sarah, Luis, Ivan M., Stefan, Vincent, Ivan R., Ian, Adriana, Flavia, Pierrot, Paula, Elena, Keshav, Lucy, Lio, Chris, Nadia, Jorge, Ixchel, Laura, Diana, David, Jessica. thanks for all these scientific and/or funny conversations we had, the meals, coffees, and of course for les bières, le vin et le fromage. I thank you all for making France my home.

I thank my supervisor Chantal Staquet, and I thank the people who were open to having scientific discussions, especially: Joel Sommeria and Bruno Voisin. Without your help, your time, and your patience this thesis wouldn't be possible. I thank the reviewers Caroline Müller and Patrice Le Gal, and my jury members Henri-Claude Nataf and Julien Le Sommer, for your interest, your time, your feedback, and for the very interesting discussions we had. I thank Cyrille Bonamy and Guillaume Roullet, for all your help and all these codding sessions we had.

I thank everybody in LEGI who helped me in so many different ways. Thank you for taking the time to chat, to help me find solutions for all sorts of problems. I want to make a special mention to the professors Achim, Martin, Christophe, Francis, and Henda. I thank Julie, Cecile, Lafiyatou, Johan, Stephan. You made my day more than once, I hope I made yours at least once.

I gratefully acknowledge the scholarship from CONACyT-Gobierno Francés 2016 to pursue my PhD studies.

Abstract

Large scale ocean circulation transports mass and heat all around the planet with a key role in Earth's climate [Clark et al., 2002, Woods, 1985]. Internal gravity waves play a major role in momentum transport in the ocean interior [Munk and Wunsch, 1998]. Up to the beginning of the millennium, the main sources of internal gravity waves in the ocean were thought to be the tide, by interaction with bottom topography, and surface wind stress. Field campaigns in the deep Southern Ocean have revealed that the interaction of the Antarctic Circumpolar Current with bottom topography can radiate internal gravity waves, referred to as lee waves, as it does the wind blowing over a mountain in the atmosphere [Naveira-Garabato et al., 2004, Nikurashin and Ferrari, 2010b]. The field measurements suggest that, over rough topography, these lee waves play a key role in momentum transport and fluid mixing through their breaking [Polzin et al., 1995]. As oceanic topographic flows occur at scales too small to be solved by current global oceanic circulation models, it is necessary to parameterize their effects in larger scale numerical models [Vosper et al., 1999]. For instance, the momentum balance associated with the waves can be expressed in terms of a wave drag. In order to be able to run long term climate simulations, having a good [Trossman et al., 2013] time-dependent parametrization of the wave drag is determinant [Lefauve et al., 2015]. However, deep ocean measurements are sparse, so the understanding of the oceanic momentum balance is still incomplete. Additionally, the impact of rotation in wave emission and propagation plays a key role in the momentum balance [Nikurashin and Ferrari, 2010b]. If bottom topography partially blocks the current, part of the current may flow around the topography, producing a wake, with possibly little -or even no- energy transferred to the wave field [Nikurashin et al., 2013]. Nevertheless, most of the numerical analysis to parametrize the wave drag are either 2D analysis or they do not consider the effect of rotation.

The drag force estimates the amount of energy/momentum of current dissipated by the wake or waves. This problem has never been addressed before and is the subject of the present work. This thesis is a continuation of the experimental study done by [Sommeria et al., 2016], where through comparisons with 3D numerical simulations and linear theory we give an estimate for the drag force induced by the topography over the flow. As this study is done with and without rotation, we were able to study the impact of rotation in the relative sinks of the energy of the mean flow due to the emission of a lee wave field and to the formation of a wake behind the topography.

Résumé

La circulation océanique à grande échelle transporte la masse et la chaleur tout autour de la planète, ce qui joue un rôle clé dans le climat de la Terre [Clark et al., 2002, Woods, 1985]. Les ondes internes de gravité jouent un rôle majeur dans le transport de quantité de mouvement à l'intérieur des océans [Munk and Wunsch, 1998]. Jusqu'au début du millénaire, on pensait que les principales sources d'ondes de gravité interne dans l'océan étaient la marée, par interaction avec la topographie du fond, et le stress du vent de surface. Des campagnes de terrain dans les profondeurs de l'océan Austral ont révélé que l'interaction du courant circumpolaire antarctique avec la topographie du fond peut irradier des ondes internes de gravité, appelées "ondes sous le vent", par analogie avec le vent qui souffle sur une montagne dans l'atmosphère [Naveira-Garabato et al., 2004, Nikurashin and Ferrari, 2010b]. Les mesures sur le terrain suggèrent que, sur une topographie accidentée, ces ondes sous le vent jouent un rôle clé dans le transport du quantité de mouvement et le mélange des fluides grâce à leur rupture [Polzin et al., 1995]. Comme les flux océaniques topographiques se produisent à des échelles trop petites pour être résolus par les modèles actuels de circulation océanique globale, il est nécessaire de paramétrer leurs effets dans des modèles numériques à plus grande échelle [Vosper et al., 1999]. Par exemple, le bilan de quantité de mouvement associé aux ondes peut être exprimé en termes de traînée d'onde. Afin de pouvoir effectuer des simulations climatiques à long terme, une bonne paramétrisation [Trossman et al., 2013] en fonction du temps de la traînée d'onde est déterminante [Lefauve et al., 2015]. Cependant, les mesures en eaux profondes sont rares, de sorte que la compréhension du bilan de quantité de mouvement océanique est encore incomplète. En outre, l'impact de la rotation dans l'émission et la propagation des ondes joue un rôle clé dans le bilan de quantité mouvement [Nikurashin and Ferrari, 2010b]. Si la topographie du fond bloque partiellement le courant, une partie du courant peut circuler autour de la topographie, produisant un sillage, avec peut-être peu - ou même pas - d'énergie transférée au champ d'onde [Nikurashin et al., 2013]. Néanmoins, la plupart des analyses numériques visant à paramétrer la traînée d'onde sont soit des analyses en 2D, soit elles ne tiennent pas compte de l'effet de la rotation.

La force de traînée estime la quantité d'énergie/quantité de mouvement de courant dissipée par le sillage ou les ondes. Ce problème n'a jamais été abordé auparavant et fait l'objet du présent travail. Cette thèse est une continuation de l'étude expérimentale faite par le laboratoire [Sommeria et al., 2016], où par des comparaisons avec des simulations numériques 3D et la théorie linéaire nous donnons une estimation de la force de traînée induite par la topographie sur l'écoulement. Comme cette étude est faite avec et sans rotation, nous avons pu étudier l'impact de la rotation dans les puits relatifs de l'énergie de l'écoulement moyen dû à l'émission d'un champ d'ondes sous le vent et à la formation d'un sillage derrière la topographie.

Notation and abbreviates

$N = \sqrt{-\frac{g}{\rho(z)}\frac{d\rho}{dz}}$	Buoyancy or Brunt-Väisälä frequency (Ocean/Atmosphere $N \sim 10^{-2}s$).
ϱ	Characteristic density of the fluid.
$\mathcal{L}$	Characteristic length scale of the fluid.
$\mathcal{U}$	Characteristic velocity.
$f = 2\Omega$	Coriolis frequency.
$F = f/\rho_0$	Coriolis frequency per unit mass.
DSL	Dividing Stream Line.
$C_{D_{\text{total}}}$	Total drag coefficient.
$C_{D_{\text{wake}}}$	Drag coefficient induced by the wake.
$C_{D_{\text{waves}}}$	Drag coefficient induced by the waves.
p	Dynamic pressure.
FFT	Fast Fourier Transform.
iFFT	inverse Fast Fourier Transform.
U_0	Flow rate (mean).
ρ	Fluid density variations.
Ω	Frequency, rotation.
$Fr = \frac{U_0}{Nh}$	Froude Number.
$\vec{c}_g$	Group velocity.
IOs	Inertial Oscillations.
IGWs	Internal Gravity Waves.
ν	Kinematic viscosity.
LT	Linear Theory.
LT+DSL	Linear Theory with Dividing Streamline hypothesis.
μ	Molecular viscosity.
NHM	Non-Hydrostatic Model.
$\nabla = \left(\frac{\partial}{\partial x}, \frac{\partial}{\partial y}, \frac{\partial}{\partial z}\right)$	Operator Divergence.
$\nabla_H = \left(\frac{\partial}{\partial x}, \frac{\partial}{\partial y}, 0\right)$	Operator Horizontal-Divergence.
PIV	Particle Image Velocimetry.
$\vec{r} = (x, y, z)$	Position vector.
$Pr = \frac{\nu}{\kappa}$	Prantl number.
$Re = \frac{Uh}{\nu}$	Reynolds number.
$Ro = \frac{U}{Lf}$	Rossby number.
$R = 40$ cm	Sphere's radius.
$St = \frac{f_{\text{vortex}}d}{U_0}$	Strouhal number.
d	Topography's diameter
h	Topography's height.
$\vec{u} = (u, v, w)$	Velocity vector.
u	Velocity, x-component.
v	Velocity, y-component.
w	Velocity, z-component.
f_{vortex}	Vortex shedding frequency.

Contents

1 Introduction

Climate is defined as the general weather conditions usually found in a particular place. Accordingly, Earth's climate is an average of all the world's atmospheric conditions. Since the ocean covers most of the Earth's surface and water has a high heat capacity compared to air, ocean has a strong impact in Earth's climate, driving heat all around the world through oceanic currents [Clark et al., 2002, Woods, 1985].

Additionally to heat, oceanic currents drive pollutants [Howell et al., 2012], nutrients and living organisms [Reid et al., 1978, MacKinnon, 2013] leading to biodiversity and plastic islands. These currents can be either superficial, deep or both, as tidal currents [Arbic et al., 2018]. Understanding the oceanic currents and their energy budget plays a key role in understanding biological and climate processes at the global scale.

Just like the land's surface, the oceanic floor is conformed by complex topographic structures like valleys, abyssal zones and mountains. Like the atmosphere, the ocean is stratified in density due to temperature gradients and salinity concentrations [Ferrari and Boccaletti, 2004], i.e. oceanic density varies continuously with depth [Wurtele et al., 1993]. So, the deep ocean currents interact with this complex topography like the wind currents interact with land's topographic structures, modifying the flow in different ways, depending on the flow energy and the topographic shape and size [Sutherland, 2010]. These interactions might lead to the production of a turbulent wake and internal gravity waves (IGWs) [Smith, 1989, Baines, 1995]. As the boundary layer which is modeled with a bottom drag, the energy extracted by the waves can be also modeled with a wave drag coefficient [Shriver et al., 2012]. The total induced drag produces a drag force on the flow which can be as intense that it can balance the wind forcing on the surface, as is the case in the Bering Strait [Roach et al., 1995].

The IGWs might break near the topographic obstacle or they can travel thousands of kilometers away [Zhao et al., 2016] and break in the ocean interior. Thus, a fraction of the waves energy is transferred to the ocean interior through the generation of turbulence in overturning events [Dossmann et al., 2016b, Munk and Wunsch, 1998, Polzin et al., 1997].

This transfer of momentum and energy, via mixing, has a crucial role in the meridional overturning circulation and in the oceanic dynamics [Nikurashin et al., 2013, Couto et al., 2020]. Although what physics drives the enhanced mixing in ocean is an open question [Nikurashin and Ferrari, 2010b], the Antarctic Circumpolar current is recognized as the main source of ocean mixing with a strong production of IGWs by the bottom topography. These waves produced in the lee of the topographic obstacle are called lee waves. There are lee waves induced by the interaction of eddies with smaller scale lateral topographies, at such scales, the bottom velocities vary slowly and thus, these waves are quasi-steady.

The geostrophic eddies in the Southern Ocean must dissipate either in the ocean interior or through interaction with the bottom topography [Nikurashin et al., 2013]. The interaction of the Antarctic Circumpolar Current with rough bottom topography can radiate IGWs and transfer their momentum above the topography [Naveira-Garabato et al., 2004], or these waves can propagate and break away from the topography and transfer their momentum in the ocean interior [Polzin et al., 1995] accelerating or damping the oceanic currents [Sutherland and Linden, 2002].

However, even though IGWs have a non-negligible impact upon large scale geophysical flows, the processes by which internal waves are generated, propagate, interact and break are not well understood beyond linear theory [Sutherland and Linden, 2002]. Additionally, as the wave production occurs at scales too small to be solved by global oceanic circulation models, it is necessary to parameterize their effects in larger scale numerical models [Vosper et al., 1999]. Thus, different scenarios that produce wave breaking have been explored experimentally and numerically. Wave breaking might occur due to focusing of internal gravity waves with particular geometries such as torus [Ermanyuk et al., 2017] or because of oblique reflections of wave beams over planes [Leclair et al., 2019]. IGW's breaking has been observed as well in 2D numerical simulations for an idealized sinusoidal topography, due to resonant interactions of IGWs [Nikurashin and Ferrari, 2010b]. Non linear interactions between waves have been studied using paddles to generate Bessel function waves patterns [Boury et al., 2019].

Fluid behaves differently for 3D topographies. If the Froude number $Fr = \frac{U_0}{Nh}$ is smaller than 1, this means that the flow has not enough kinetic energy to rise over the topography of height h (here U_0 is the upstream velocity and N the buoyancy frequency) [Sommeria et al., 2016] thus, there is a portion of fluid flowing around the topography with quasi-horizontal motion and a portion flowing above it, exciting a lee wave. These two sections are separated by a dividing streamline (DSL) [Sheppard, 1956] at a vertical level such that the remaining height h_{eff} of the cap above corresponds to a Froude number $\frac{U_0}{Nh_{\text{eff}}} = 1$: in other words it is defined by $h_{\text{eff}} = hFr$ (for $Fr < 1$) [Sommeria et al., 2016]. On the other hand, if $Fr > 1$ the whole topography height h is involved in the wave emission. This behavior has been studied in the context of atmospheric dynamics and several laboratory experiments in a linearly stratified fluid [Baines, 1995, Dalziel et al., 2011].

Voisin wrote two [Voisin, 1994, Voisin, 2007] reviews focused on the theoretical aspects

of the generation of internal gravity waves by the flow of a density-stratified fluid. The most recent one discusses two limit cases: weak or strong stratification, corresponding to large or small internal Froude number, respectively. An original model is proposed for strong stratification, based on the DLS concept and elaborating on earlier ideas by [Newley et al., 1991], [Greenslade, 1992, Greenslade, 2000] and [Hunt et al., 1997]. Similar models have been proposed independently by [Hunt et al., 2006] and [Dalziel et al., 2011].

For a rotating fluid, most of the literature considers geostrophic flow, i.e. Taylor columns, and leaves inertial waves aside. For these, the surfaces of constant phase have been calculated by [Lighthill, 1967] and [Redekopp, 1975], based on the dispersion relation. [Hide et al., 1968] and [Lighthill, 1970] did a first attempt to describe the relation between the Taylor column and the waves, nevertheless they were wrong. [Cheng, 1977] and [Stewartson and Cheng, 1979] made a calculation of the waves. They developed a new analysis for thin topography, of small slope $\epsilon \ll 1$, in a rapidly rotating flow, of small Rossby number $Ro \ll 1$. The analysis was quasi-geostrophic, replacing the horizontal accelerations by their geostrophic values in the equations of motion. This is a low-frequency approximation, akin to the hydrostatic approximation for internal waves. It led Stewartson & Cheng to identify the waves and the Taylor column as two separate components of the flow.

The approach was extended later by [Johnson, 1982] and [Cheng and Johnson, 1982] to viscous flow, in two and three dimensions, respectively. Johnson showed the linearization for thin topography to remain valid, in two dimensions, for bluff topography; specifically, he proved the linearization to require $\epsilon \ll 1$ in three dimensions and $\epsilon Ro \ll 1$ in two dimensions. The waves, visible in earlier experiments by [Maxworthy, 1977] for a two-dimensional ridge and simulations by [Mason and Sykes, 1981] for a three-dimensional obstacle, were measured by [Heikes and Maxworthy, 1982] for cylindrical ridges and spherical caps, showing, in particular, that the quasi-geostrophic approximation is not always valid. The topic was recently revived by [Machicoane et al., 2018], who developed an approach devoid of the quasi-geostrophic approximation and compared it with high-precision PIV measurements for a translating circular cylinder.

In an attempt to parametrize the wave drag, [Trossman et al., 2013] found that this wave drag cannot be mimicked by artificially increasing the quadratic bottom drag because the energy dissipation rates associated with bottom drag are not spatially correlated with those associated with wave drag where the latter are small. Additionally, the wave drag is not a local sink of energy whereas the bottom drag is.

On the other hand, topographic and island wakes extract an important amount of energy from the flow [Perfect et al., 2020]. For instance, these wakes might even induce instabilities in the flow as observed [Dong and McWilliams, 2007]. In order to be able to run a model which includes a full coupling between wind power, eddies and geostrophic circulations, stratification, and lee-wave drag and induced mixing it is required to have a state-dependent, time-evolving parameterization for the effects of lee waves [MacKinnon et al., 2017].

[Dossmann et al., 2016a, Dossmann et al., 2016b] found experimentally that the eddy

diffusivity $K_{T,<\rho w>}$ is enhanced by breaking IGWs due to a triadic resonance instability process. Using idealized 2D numerical simulations and linear theory [Nikurashin and Ferrari, 2010b, Nikurashin et al., 2013]. The numerical configuration of [Nikurashin and Ferrari, 2010b] was considered again by [Labreuche, 2015] to analyze the growth of inertial oscillations and their impact on fluid mixing. [Richet et al., 2018] did a realistic 2D numerical simulations showing that the rough bottom topography plays an important role in the wind momentum transfer to enhance abyssal mixing in the ocean via IGWs.

Motivated by the numerical results of [Labreuche, 2015] for an idealized 2D topography, laboratory experiments were done by [Sommeria et al., 2016] using a spherical cap topography in a linearly stably stratified fluid in the CORIOLIS platform located in LEGI. This thesis is done as a continuation of these experimental measurements, and its aim is to have a better understanding (i) of the relative sinks of the energy of the mean flow due to the emission of a lee wave field and to the formation of a wake behind the topography and (ii) of the role that rotation plays in the total induced drag by the topography over the flow.

The system is studied with three different approaches: 1) an analysis of the PIV experimental measurements, 2) a theoretical study in the linear theory approximation and 3) three-dimensional numerical simulations done using the NHM model (Non-Hydrostatic Model) developed by [Aiki and Yamagata, 2004]. The results of all the three methods are compared and discussed along the thesis document which is organized as follows:

A general description of the experimental and numerical setups is done in chapter 2. This chapter is subdivided into two main sections: section 2.2 where the experimental setup is presented only to make a self-consistent document, nevertheless all the experimental measurements were done by Ajayi Adekunle for his master's thesis [Ajayi, 2016]. Then, in section 2.4 are included the numerical model's description, its validation and the 3D numerical configuration.

The results obtained with these three methods are presented and analyzed in three different chapters as follows: In chapter 3, a theoretical description of the produced internal gravity waves in a linearly stable-stratified fluid with buoyancy frequency N is done in the linear lee wave theory approximation. In this chapter the impact of the dividing streamline hypothesis (DSL) is considered and evaluated by a comparison with the PIV experimental measurements with the whole field computed numerically using the iFFT FORTRAN's intrinsic subroutine. In this chapter, we present as well an algebraic solution in the far field approximation done by [Voisin, 2016] which is in a very good agreement with the compared PIV experimental results and the numerically iFFT computed results. In chapter 4 the results for the non-rotating configurations obtained from the 3D numerical simulations are compared with the results obtained from the PIV measurements. In chapter 5 the effect of rotation is considered for a non-zero Coriolis frequency, $f = 0.19$ s^{-1} ($f/N = 0.4$), through the comparison of the 2D and 3D numerical simulations with the PIV measurements. Then a sensibility study, keeping $N = 0.48$ s^{-1} fixed, is done for different rotation rates with $f/N = 0.1$, $f/N = 0.2$, $f/N = 0.3$, $f/N = 0.5$, and $f/N = 0.8$. Finally the conclusions and

perspectives are presented in chapter 6.

2

Numerical and experimental setup

2.1 Introduction

Motivated by the numerical results of [Labreuche, 2015] for an idealized 2D topography, a set of experimental measurements were done by [Sommeria et al., 2016] for horizontal PIV planes in the CORIOLIS platform localized in LEGI. A description of the experimental setup is presented in section 2.2, and its results are presented and analyzed in chapter 4 and chapter 5. It is important to remark that the experimental setup is presented in this chapter in order to make a self-consistent document, nevertheless all the experimental measurements were done by Ajayi Adekunle for his master's thesis [Ajayi, 2016].

As described in the general introduction, a set of 2D and 3D numerical simulations were done to have a better understanding of the [Sommeria et al., 2016] experimental results. These simulations were done using the NHM model (Non-Hydrostatic Model) developed by [Aiki and Yamagata, 2004]. The code's validation, the 2D and 3D numerical setups are described in section section 2.4 and the results are shown and analyzed in chapter 4 and chapter 5.

2.2 Experimental Setup

In the context of the Antarctic Circumpolar Current (ACC), PIV experimental measurements were performed by [Ajayi, 2016, Sommeria et al., 2016]. These experimental measurements were done in a rotating cylindrical tank of diameter $D = 13$ m known as CORIOLIS platform[1] located in LEGI, Grenoble. The CORIOLIS platform was filled with a $H = 91.5$ cm water layer. The water's density is linearly-stratified by salinity using the slip under method introduced by [Fortuin, 1960]. The stratification is made by filling the tank from the bottom with increasingly salty water, obtained by computer-controlled mixing from two underground tanks with specified salinity.

[1] See https://my.matterport.com/show/?m=CXxXSbTXREB for a CORIOLIS platform virtual visit

The ACC is characterized by a buoyancy frequency of $N = 7 \times 10^{-4}$ s^{-1} and a speed of $U_0 = 10$ cm/s in the deep ocean and a Coriolis parameter of $f = 1.5 \times 10^{-4}$ s^{-1}, so that $f/N = 0.2$ (see e.g. [Nikurashin et al., 2013]). The experimentally chosen Froude numbers that go from 0.31 to 1.25 correspond to topographic heights $h = \frac{U_0}{NFr}$ in the range of $460 - 115$ m with a base diameter of $1600 - 400$ m, if the same topographic aspect ratio $d/h = 3.5$ is maintained. However, given the f/N ratio is half that of the experiment, a better agreement with ACC measurements is expected for a topography that is twice as flat, with a base diameter of $3200 - 800$ m. In fact, in the hydrostatic approximation, the relevant similarity parameter $(f/N)(d/h)$ is used to compare situations with different aspect ratios. Our rotation experiments are representative of the effect of circular seamounts a few kilometers in diameter and a few hundred meters in height. The Reynolds number $Re = U_0 h/\nu$ is in the range of $0.6 - 2.4 \times 10^4$, which is of course smaller than in the ocean, but is sufficient to achieve instability and turbulent processes.

The considered topography consists of a spherical cap, which is fixed on the horizontal flat bottom of the tank. The cap has a curvature radius $R = 40$ cm, a height of $h = 20$ cm and a diameter of $d = 69$ cm at its base (see figure 2.2). It is placed at a distance of 200 cm from the wall of the tank, at a distance $r_0 = 450$ cm from the center of the tank, as shown in figure 2.2 so that the lateral confinement of the wake is marginal.

Thus, two different sets of experiments are done (see figure 2.1): with and without rotation. The density stratification is such that the buoyancy frequency is set to $N = 0.48$ s^{-1} for all the experiments (corresponding to $\delta\rho/\rho = 2.15\%$ above the water level H). For the rotating case, the linear stratification is done while the tank is rotating at a constant rotation speed $\Omega = 0.095$ s^{-1}. This imposes a Coriolis parameter $f = 0.19$ s^{-1} and $f/N = 0.4$. Once the water column reaches the desired depth $H = 91.5$ cm, a small sudden change $\Delta\Omega$ is imposed in the platform's rotation rate producing a counter-rotating current of speed $U_0 = r_0\Delta\Omega$. For the non rotating case, the tank is filled up with the platform at rest ($f = 0$ s^{-1}) and then it is suddenly set into rotation with a constant rotation speed Ω_2, creating a counter rotating current $U_0 = r_0\Omega_2$.

In both cases there is a water current which persists by inertia throughout the duration of the experiment (around 15 min) with quasi-steady properties. The changes in the rotation rate are done in such way that the incoming flow velocity at the center of the topography is either 3 cm/s, 6 cm/s, 9 cm/s or 12 cm/s. Then, the experiments' Froude number $Fr = U_0/(Nh)$ ranges from 0.31 to 1.25.

Velocity fields are measured by using Particle Image Velocimetry method (PIV) in horizontal planes at different depths. The laser sheets are produced by a rapidly oscillating mirror (100 Hz) from a continuous 6 watt Yag laser placed at the center of the tank. Polystyrene particles with a diameter of 0.2 mm are sorted by density in the fluid, to provide a uniform concentration at different heights. The vertical density profiles are measured before and during the experiment by two motorized profilers equipped with conductivity probes.

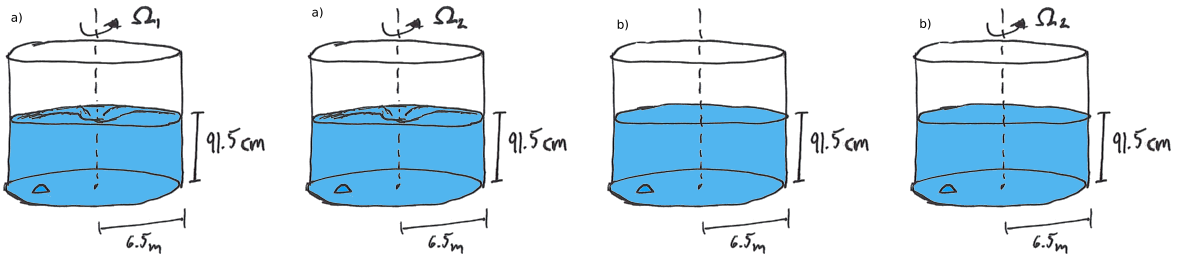

Figure 2.1: Sketch of the experimental setup preparation. Two different sets of experiments were done: a) With rotation (see the two figures in the left) while the basin was rotating at a constant frequency Ω_1, it was filled up with a $H = 91.5$ cm stratified water layer, the tank's rotating rate was suddenly changed to a constant rotation frequency Ω_2, producing a current that lasted during the whole experiment. b) Without rotation (see the two last figures on the right) while the basin was in rest, it was filled up with a $H = 91.5$ cm stratified water layer, suddenly the tank was put into rotation to a constant rotation frequency Ω_2, producing a current that lasted the whole experiment.

The PIV's acquisition is done by a set of three cameras, covering an area of 2 m wide by 7 m of the periphery field. The covered area is centered on the radius $r_0 = 4.5$ m (see figure 2.2). The acquisition process is done either at a fixed depth or scanning different depths during the same experiment. The scanning method consists of acquiring a set of 100 images (typically 25 s) per level at ten different levels. In this method, the domain is scanned by sections either at the top, to explore the wave behavior, or at the bottom, to explore the wake dynamics. Thus, the experiments are repeated twice to cover the whole domain.

2.3 Equations of fluid motion in the Boussinesq approximation

2.3.1 Equations of motion

The Euler equations [Landau and Lifshitz, 1986] for an inviscid fluid of density ϱ, pressure P and velocity $\vec{u} = (u, v, w)$ in a system of Cartesian coordinates $(x, y, z) = x\hat{\imath} + y\hat{\jmath} + z\hat{k}$ with the z axis pointing upwards, are:

$$\varrho\left(\frac{Du}{Dt}\right) = -\frac{\partial P}{\partial x}, \tag{2.1a}$$

$$\varrho\left(\frac{Dv}{Dt}\right) = -\frac{\partial P}{\partial y}, \tag{2.1b}$$

$$\varrho\frac{Dw}{Dt} = -\frac{\partial P}{\partial z} - g\varrho. \tag{2.1c}$$

If the fluid is in a rotating frame of reference with angular velocity vector $\vec{\Omega} = \Omega\hat{k}$, then

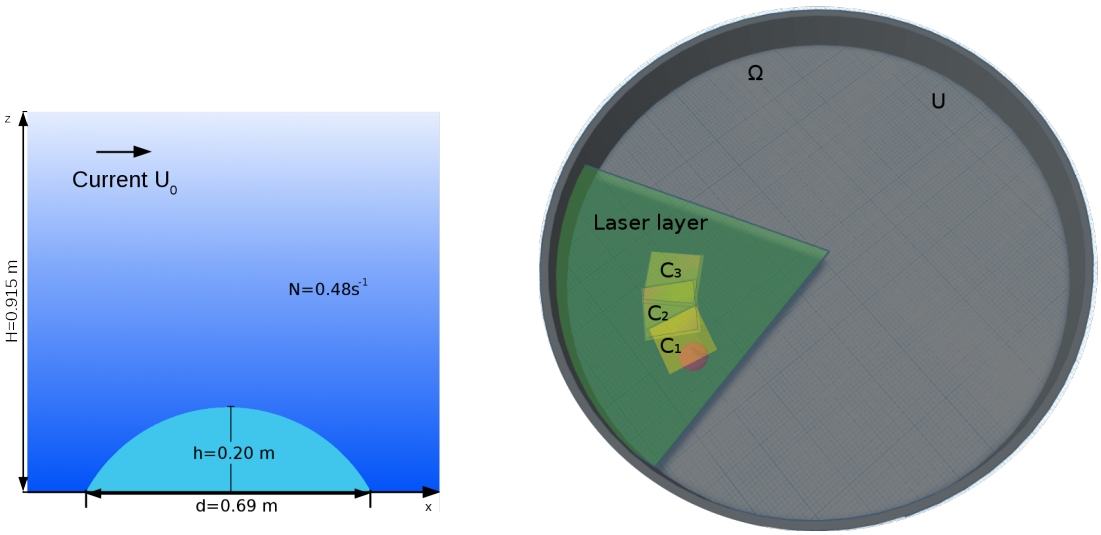

Figure 2.2: Sketch of the experimental setup. A spherical cap of diameter $d = 69$ cm is immersed in a $H = 91.5$ cm linearly density stratified water layer with bouyancy frequency $N = 0.48$ s^{-1} which is flowing at a constant ratio $U_0 = 3$ cm/s, 6 cm/s, 12 cm/s, with and without rotation. As observed in the figure on the right, PIV measurements are done using a green laser layer and 3 CCD cameras.

the Coriolis force $2\vec{u} \times \Omega$ shall be considered in the left-hand side of Euler's equation as follows [Landau and Lifshitz, 1986]:

$$\varrho\left(\frac{Du}{Dt} - fv\right) = -\frac{\partial P}{\partial x}, \tag{2.2a}$$

$$\varrho\left(\frac{Dv}{Dt} + fu\right) = -\frac{\partial P}{\partial y}, \tag{2.2b}$$

$$\varrho\frac{Dw}{Dt} = -\frac{\partial P}{\partial z} - g\varrho. \tag{2.2c}$$

with $f = 2\Omega$ the Coriolis parameter.

This system of partial differential equations, expressing the conservation of momentum, is complemented by the equation of continuity,

$$\frac{\partial}{\partial t}\varrho + \nabla\cdot(\varrho\vec{u}) = \frac{D\varrho}{Dt} + \varrho\nabla\vec{u} = 0, \tag{2.3}$$

expressing the conservation of mass, and the incompressible equation of state,

$$\frac{D\varrho}{Dt} = 0. \tag{2.4}$$

expressing the conservation of energy. Using equation (2.4) into equation (2.3),

$$\nabla\cdot\vec{u} = 0 \tag{2.5}$$

As the oceanic water has a very low compressible ratio, for small depth variations its density can be modeled as a constant value [Staquet, 2005]. However, this approximation, does not allow the description of some phenomenons which occur in the ocean, like internal waves. In these cases, the density of the fluid varies a little over the depth of the fluid, leading to the Boussinesq approximation [Sutherland, 2010]. The pressure P and density ϱ are separated into background values $p(z)$ and $\rho(z)$, respectively, related by the hydrostatic balance

$$\frac{dp}{dz} = -\rho g, \tag{2.6}$$

and the perturbations p' and ρ', respectively, with

$$P = p + p' \qquad\qquad \varrho = \rho + \rho' \tag{2.7}$$

The background density profile $\rho(z)$ is separated into a constant reference value ρ_0 and variations $\Delta\rho(z)$, such that,

$$\rho(z) = \rho_0 + \Delta\rho(z). \tag{2.8}$$

The Boussinesq approximation consist in assuming

$$|\rho'| \ll |\Delta\rho| \ll \rho_0$$

such that the variations $\Delta\rho$ and ρ' may be neglected except in the expression of buoyancy forces.

The Euler equations become,

$$\rho_0 \left(\frac{Du}{Dt} - fv \right) = -\frac{\partial p'}{\partial x}, \tag{2.9a}$$

$$\rho_0 \left(\frac{Du}{Dt} + fu \right) = -\frac{\partial p'}{\partial y}, \tag{2.9b}$$

$$\rho_0 \frac{Dw}{Dt} = -\frac{\partial p'}{\partial z} - g\rho'. \tag{2.9c}$$

while the continuity equation remains unchanged as

$$\nabla \cdot \vec{u} = 0. \tag{2.10}$$

where, imposing the fluid incompressibility is equivalent to considering that the sound is much faster than the internal waves propagation velocity [Sutherland, 2010]. In other words, the sound waves have been filtered out.

The equation of state writes,

$$\frac{D\rho'}{Dt} = -w\frac{d\rho}{dz}, \tag{2.11}$$

which in terms of the buoyancy frequency

$$N(z) = \sqrt{-\frac{g}{\rho_0}\frac{d\rho}{dz}}$$

becomes

$$\frac{D\rho'}{Dt} = \rho_0 \frac{N^2}{g} w \tag{2.12}$$

The equations for the approximation of Boussinesq for the laws of conservation of momentum, internal energy and mass equations (2.9), (2.10) and (2.12) respectively. For motion in three dimensions, these form a coupled set of five equations in the five fields of velocity $\vec{u} = (u, v, w)$, dynamic pressure p', and fluctuation density ρ'.

A consequence of the Boussinesq equations is that they are invariant upon reflection in z if the background density gradient ρ is symmetric in z. In particular, this is the case in a uniformly stratified fluid for which ρ is constant. Thus there is no dynamical distinction between upward and downward-propagating Boussinesq internal waves [Sutherland, 2010].

The equations of motion for a fluid at rest, for small amplitude perturbations in velocity $\vec{u}$, pressure p' and density ρ' simplify to:

$$\rho_0 \left(\frac{\partial u}{\partial t} - fv \right) = -\frac{\partial p'}{\partial x},$$

$$\rho_0 \left(\frac{\partial u}{\partial t} + fu \right) = -\frac{\partial p'}{\partial y},$$

$$\rho_0 \frac{\partial w}{\partial t} = -\frac{\partial p'}{\partial z} - g\rho',$$

$$\nabla \cdot \vec{u} = 0.$$

This set of equations has a solution a plane monochromatic wave of frequency ω and wavevector $\vec{k} = (k_x, k_y, k_z)$, in which $\vec{u}$, p' and ρ' vary as:

$$e^{i(k_x x + k_y y + k_z z - \omega t)},$$

satisfy the dispersion relation

$$\omega^2 = N^2 \frac{k_H^2}{k^2} + f^2 \frac{k_z^2}{k^2}$$

where $k^2 = k_x^2 + k_y^2 + k_z^2$ and $k_H^2 = k_x^2 + k_y^2$.

The group velocity,

$$\vec{c}_g = \left(\frac{\partial \omega}{\partial k_x}, \frac{\partial \omega}{\partial k_y}, \frac{\partial \omega}{\partial k_z} \right),$$

with which the energy propagates, is given by

$$\vec{c}_g = \frac{N^2 - f^2}{\omega} \left(\frac{k_x k_z^2}{k^2}, \frac{k_y k_z^2}{k^2}, -\frac{k_z k_H^2}{k^2} \right).$$

Let us define θ as the angle that the group velocity $\vec{c}_g$ makes with the horizontal, then, the dispersion relation can be rewritten as,

$$\omega^2 = N^2 \sin^2\theta + f^2 \cos^2\theta \tag{2.14}$$

The group velocity is perpendicular to the wavevector $\vec{k}$, implying that the phase and the waves energy propagate at a right angle to each other. In the ocean the buoyancy frequency N is usually larger than the Coriolis parameter f, so the wavevector and group velocity have horizontal components of identical signs and vertical components of opposite sign when the frequency ω is positive. In the other hand, when the frequency ω is negative, the wavevector and the phase velocity have horizontal components with opposite sings and vertical components with identical signs.

2.4 Numerical simulations

In this section, the numerical setups of the simulations done using the NHM model are presented. First, the model is validated by the reproduction of the numerical results obtained by [Nikurashin et al., 2013, Labreuche, 2015] for an idealized sinusoidal topography. This setup and its results are shown in section 2.4.2. Then, the 2D numerical setup for the central vertical section of a spherical cap is described in section 2.4.3. Finally, in section 2.4.4, a 3D setup for a spherical cap as the one described in section 2.2 is presented as a generalization of the 2D configuration.

2.4.1 Description of the numerical model

The Non-hydrostatic Ocean Model for the Earth Simulator (NHOES) was written in FORTRAN 90 by Hidenori Aiki. A prototype of this code was used in [Aiki and Yamagata, 2004, Aiki et al., 2006]. This code has two available versions NHOES has two versions: NHM (Non-Hydrostatic Model) and NRM (Non-Hydrostatic Rectangular Model). The here presented results were obtained using the NRM version. User's interface was significantly improved by Bach Lien Hua and Sylvie Le Gentil (IFREMER)

The basic formulation is based on [Marshall et al., 1997] nonhydrostatic, incompressible Boussinesq equations discretized with Arakawa's C-grid some differences with MITgcm, as given in README file of NHM, are:

1. parallelization is the first priority in coding
2. non-hydrostatic pressure is solved by BiCGSTAB2 method
3. free sea surface solved by splitting external/internal modes
4. a vector-invariant form is adopted for momentum equations

5. a leap-frog scheme is used for time integration

6. 3-dimensional biharmonic operator for the subgrid-scale mixing

7. all binary output (i.e. snapshot and restart files) can be done in either the NetCDF or GrADS format.

The following variables are solved in the model [Aiki and Yamagata, 2004]:

$\vec{u} = (u, v, w)$	velocity vector in Cartesian coordinates.
$\rho,\ T$	passive tracer
p	pressure

Here, p is the pressure written as the sum of three terms,

$$p = p_s + p_{hy} + p_{nh} \tag{2.15}$$

where, p_s is the surface pressure $p_s = g\nu/\rho_0$, with reference density ρ_0, gravity acceleration g and the free surface height η. The second term is the hydrostatic pressure $p_{hy} = \int_0^z -g\frac{\rho}{\rho_0}dz$ and the last term is the non-hydrostatic pressure p_{nh}.

The solved equations are the following:

$$\frac{\partial \vec{u}}{\partial t} = -\nabla p - \vec{u}\nabla\vec{u} + \vec{f} \times \vec{u} - \vec{F}, \tag{2.16}$$

where $\vec{f} = (2\Omega v, -2\Omega u, 0)$ is the Coriolis vector, with Coriolis parameter $\vec{f} = 2\Omega$; $\vec{F}$ is the i-component of an external forcing on the i-momentum equation.

And the continuity equation:

$$\nabla \cdot \vec{u} = 0 \tag{2.17}$$

In this code exist the possibility to solve the equations for three different passive tracers, in this case, it was solved for the Temperature (T) and density ρ:

$$\frac{\partial \vec{u}}{\partial t} = -\vec{u} \cdot \nabla T + \vec{F}^T \tag{2.18}$$

where $\vec{F}^T$ is a forcing term on the tracer advection equation.

$$\frac{\partial \vec{u}}{\partial t} = -\vec{u} \cdot \nabla \rho + \vec{F}^\rho \tag{2.19}$$

where $\vec{F}^\rho$ is a forcing term on the tracer advection equation.

2.4.2 Validation of the model with a sinusoidal topography

The model is validated by a reproduction of the 2D simulation (in a vertical plane) performed by [Nikurashin et al., 2013, Labreuche, 2015]. The generation of lee waves by a geostrophic flow over a topography in a stably-stratified rotating medium was studied in this simulation.

The flow configuration, as well as the physical and numerical parameters, are described below.

2.4.2.1 Physical parameters

The fluid viscosity is $\nu = 10^{-2}\, m^2/s$ with Prandtl number $Pr = 10$, so the thermal diffusivity is $\kappa = 10^{-3}$ m^2/s. Prandtl number in ocean is around 7 [Thorpe, 2005]. The fluid is linearly stratified with a buoyancy frequency $N = 1 \times 10^{-3}$ s^{-1} and rotating with Coriolis parameter frequency $f = 1.0 \times 10^{-4}$ s^{-1}. A mean flow U_0 is applied along the horizontal axis with $U_0 = 0.1$ m/s.

2.4.2.2 Size of the physical domain

A 2D simulation area discretized into 160×1000 grid points in the x and z directions, respectively, is considered. The spatial resolution along the x-direction is $\Delta x = 12.5$ m and $\Delta z = 5$ m along the vertical direction. Thus, the area measures $L_x \times L_z = 2$ km $\times$ 5 km in the x and z directions respectively.

2.4.2.3 Boundary conditions

Periodic boundary conditions are imposed along the horizontal direction. Along the vertical direction, a free-slip topography is imposed at the bottom of the domain and a sponge layer is imposed at the top. The characteristics of the topography and of the sponge layer are explained below.

Topography

The topography is sinusoidal, and its height $h_t(x)$ is given by the following expression:

$$h_t(x) = \frac{h_{max}}{2}\left(1 - \cos\left[2\pi \min\left(\left|\frac{x - L_x/2}{L_x}\right|, 1\right)\right]\right)$$

where $h_{max} = 80$ m is the topography height and z is upwards positive such that $z = 0$ at the bottom.

Sponge layer

Choosing the proper boundary conditions plays a key role in the problem's solution. In fluid numerical simulations, the domain is usually cut off artificially, and the walls of the system might create undesirable effects which would perturb the system. A simple solution is to introduce an artificial damping force, known as sponge term, in the Navier-Stokes equations, near the boundaries [Mani, 2012] which leads the flow out of the simulation cell without any spurious effect in the system.

This sponge layer is a localized restoring force imposed at the top of the domain, between the fluid and the top wall, to relax the velocity field to a desired reference value. The velocity's u-component is relaxed to the geostrophic current U_0, the v-component to zero

and, due to the continuity equation, the vertical velocity w is relaxed to zero in the sponge layer. This restoring force is therefore of the form: $(-\lambda(u - U_0), -\lambda v, 0)$ with λ defined as:

$$\lambda(z) = I_s \max\left\{\frac{e^{\frac{C}{H_s}(z-L_z)} - e^{-C}}{1 - e^{-C}}, 0\right\}$$

where $I_s = 10^{-3}$, $H_s = 3000$ m and $C = ln(100)$ is a parameter. As shown by figure 2.3, the sponge layer acts from a height of 2000 m above the ground slowly increasing in intensity up to the top of the domain.

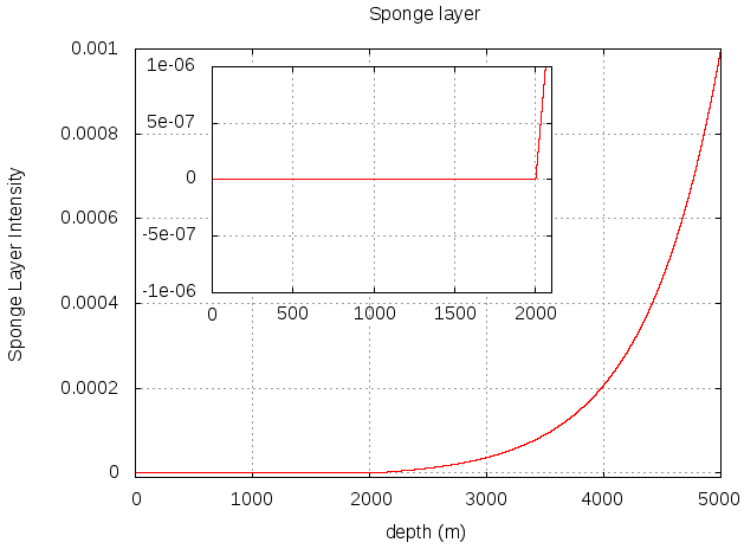

Figure 2.3: Sponge layer model [Labreuche, 2015]

2.4.2.4 Initial condition

The fluid is at rest with a linear density profile of constant buoyancy frequency $N = 10^{-3}\,\mathrm{s}^{-1}$.

2.4.2.5 Flow Forcing

In order to avoid the generation of inertial oscillations from the initial time, the geostrophic flow is imposed using a ramp function, such that it increases from 0 to U_0 within a day. The forcing is in the momentum equation for in the momentum equation for u, the x-component of the flow velocity $\vec{U} = (u, v, w)$, of the form (including the sponge layer for clarity):

$$F_u = \begin{cases} -\frac{1}{\tau_f}(u - U_0) - \lambda(u - U_0), & \text{if } t \leq 24 \text{ hours} \\ -\lambda(u - U_0), & \text{otherwise} \end{cases}$$

where $\tau_f = 1/3$ hours is the relaxation time.
Since the geostrophic current satisfies $fU_0 = -(1/\rho_0)\partial P/\partial y$, it is maintained by imposing a forcing $f\,U_0$ in the momentum equation for v, the y-component of the flow velocity $\vec{U} = (u, v, w)$, as follows:

$$F_v = \begin{cases} U_0 f - \frac{1}{\tau_f} v - \lambda v, & \text{if } t \leq 24 \text{ hours} \\ U_0 f - \lambda v, & \text{otherwise.} \end{cases}$$

Time step

With the parameters of the problem, stability is ensured with a time step equal to 10 s.

2.4.2.6 Results

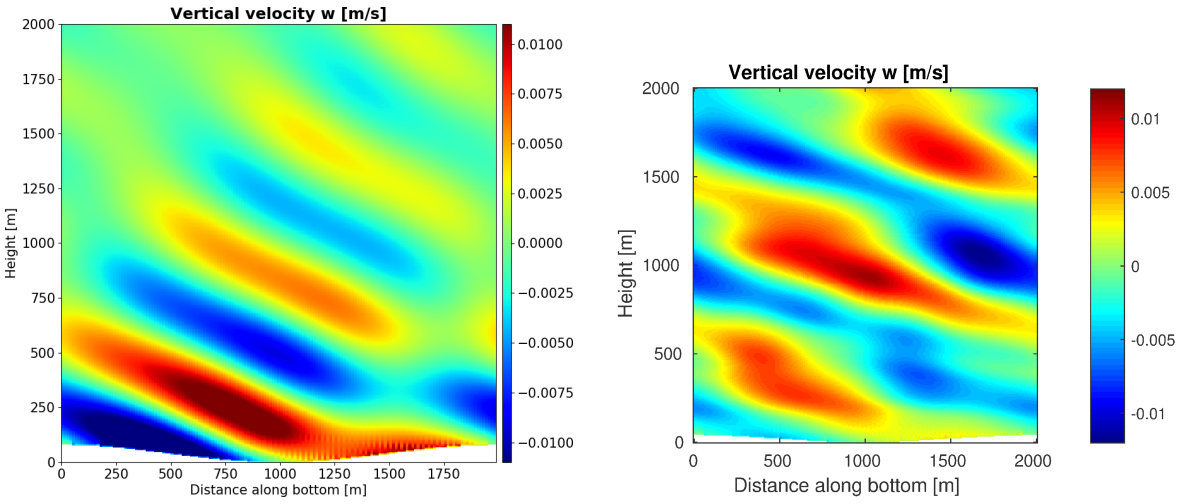

(a) Vertical velocity after 2.15 inertial periods.

(b) Vertical velocity after 7 inertial periods.

Figure 2.4: Snapshots of the vertical velocity using NHM model for a 40 m height sinusoidal topography: (a) after 2.15 inertial periods; (b) after 7 inertial periods. The (a) frame shows an internal lee wave pattern above the sinusoidal topography. The (b) frame shows that the wave pattern has evolved into a turbulent field via a braking process.

At the beginning of the simulation, a stationary internal wave pattern is produced above the topography as shown in figure 2.4. In this figure a monochromatic wave is shown, this wave transports energy away the topography with a well defined group velocity. The propagation direction of this group velocity is perpendicular to the wavevector $\vec{k}$, which is tilted an angle θ with respect the vertical line. The wave frequency of such wave packet and the modulus of the propagation vector are related by the dispersion relation given for Inertia Gravity Waves given by equation (2.14).

After 8 inertial periods, the wave pattern develops into a turbulent field. The same scenario was observed by [Labreuche, 2015] his 2D numerical simulations as shown in figure 2.5.

Figure 2.5(b) shows a non-linear effect and turbulence near the topography, non-linear effects can be observed as well in the figure 2.4(b). Also figure 2.4(a) shows a well defined lee wave pattern as figure 2.5(a) does.

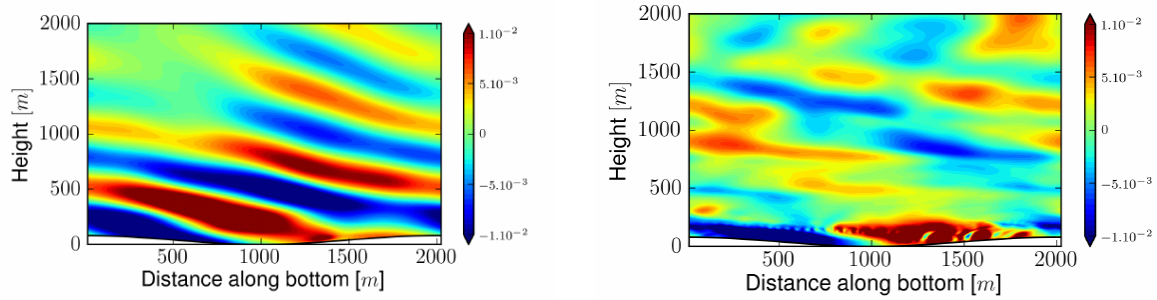

(a) Vertical velocity for H=80 m after one inertial period

(b) Vertical velocity for H=80 m after seven inertial periods

Figure 2.5: Snapshots of the vertical velocity for the 2D numerical experiment for a periodic sinusoidal topography of height $H = 80$ m. The same colorbar is used for the two panels, but the maximum value is about three times higher in frame (b) than in frame (a). The frame (a) shows a quasi-linear regime, where internal lee waves can clearly be seen to radiate from the topography upwards. The frame (b) shows a strongly non-linear regime, with turbulent behavior near the bottom. [Labreuche, 2015]

2.4.3 2D cylindrical ridge

Using as a starting point the test showed previously for a sinusoidal topography, a first 2D numerical configuration (in the central vertical plane) was designed. This 2D configuration was only used as an intermediate step to set up the 3D numerical configuration. The flow configuration, as well as the physical and numerical parameters are described below.

2.4.3.1 Physical parameters

The fluid viscosity is $\nu = 10^{-4}$ m^2/s with Prandtl number $Pr = 10$, so the thermal diffusivity is $\kappa = 10^{-5}$ m^2/s. The fluid is linearly stratified with a buoyancy frequency $N = 4.8 \times 10^{-1}$ s^{-1} and rotating with Coriolis parameter frequency $f = 0.0$ s^{-1} and $f = 1.9 \times 10^{-1}$ s^{-1}. A mean flow U_0 is applied along the horizontal axis with $U_0 = 3$ cm/s, $U_0 = 6$ cm/s and $U_0 = 12$ cm/s.

2.4.3.2 Size of the physical domain

A 2D simulation volume conformed by 1000×100 grid points in the $x-$ and $z-$directions, respectively, is considered. The spatial resolution along the x and $z-$directions is $\Delta x = \Delta z = 1$ cm. Thus, the simulation volume measures $L_x \times L_z = 10$ m $\times$ 1 m in the x and z directions, respectively.

Grid stretching

In order to prepare the 3D numerical simulation and to save computer time, a grid-stretching is imposed in the sponge-layer zone along the vertical direction as shown in figure 2.6. The code's modifications in the vertical coordinates can be seen in detail in appendix A.1.

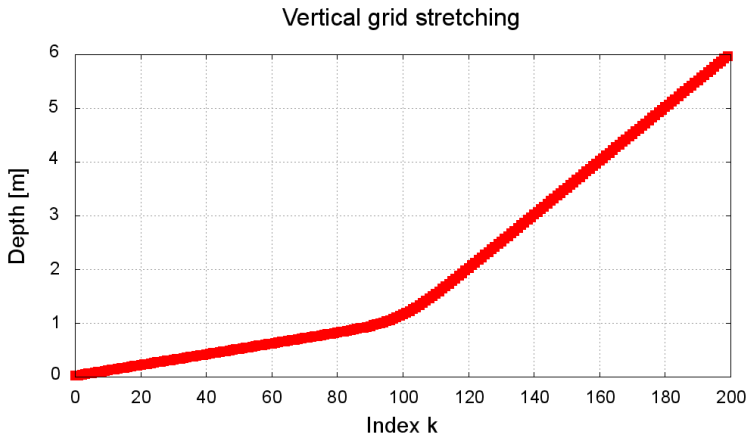

Figure 2.6: Vertical grid-stretching: Depth as a function of the index k

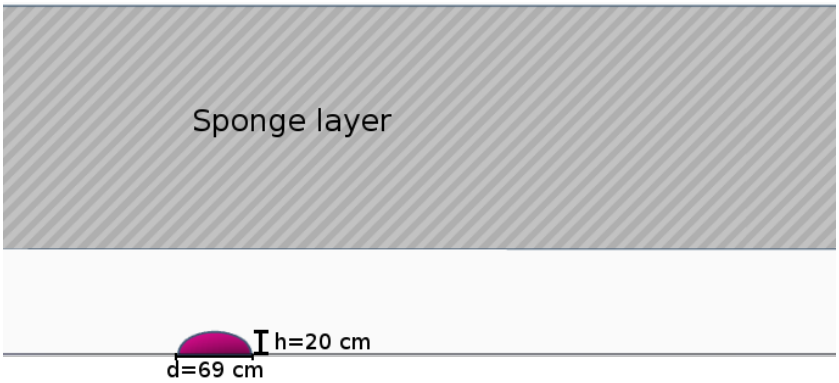

Figure 2.7: Sketch of the 2D numerical simulation configuration. The topography, shown at the bottom, is a bump of semi-circular section of height $h = 20$ cm and base $d = 69$ cm. A physical domain of 1 m depth is considered with a 4 m sponge layer above it.

2.4.3.3 Boundary conditions

Periodic boundary conditions are applied in the $x-$direction. On the topography, the boundary condition is of the free-slip type.

Topography

A single impenetrable semi-circular bump is considered as topography of height $h_t(x)$, given by the following expression:

$$h_t(x) = \begin{cases} \max\left\{\sqrt{R^2 - x^2} - (R - h), 0\right\}, & \text{if } -R \leq x \leq R \\ 0, & \text{otherwise} \end{cases}$$

where $R = 40$ cm is the sphere's radius, $h = 20$ cm is the topography's height and the z-axis is upwards positive such that $z = 0$ at the bottom (see figure 2.7).

Sponge layer

The same sponge layer model as 2.4.2 is used. Here, as shown in figure 2.8, the sponge layer acts from a height of 1 m above the ground slowly increasing in intensity up to the top of the domain at 6 m from the bottom.

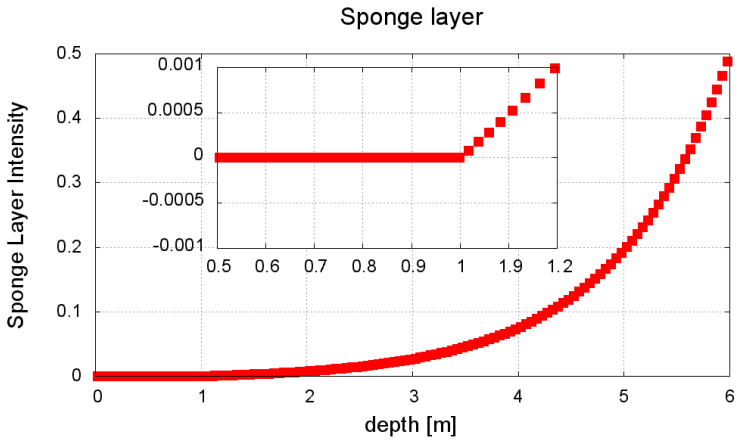

Figure 2.8: Vertical sponge layer: Intensity of the vertical sponge layer as function of depth

Initial condition

The fluid is at rest with a linear density profile of constant buoyancy frequency $N = 0.48\ \mathrm{s}^{-1}$.

Flow Forcing

The same forcing as in section 2.4.2 is used.

Time step In order to satisfy the CFL condition, time step should be $\Delta t_{U_0=3\ \mathrm{cm/s}} = 3.66 \times 10^{-3}$ s, $\Delta t_{U_0=6\ \mathrm{cm/s}} = 1.83 \times 10^{-3}$ s and $\Delta t_{U_0=12\ \mathrm{cm/s}} = 9.15 \times 10^{-4}$ s for $U_0 = 3$ cm/s, $U_0 = 6$ cm/s and $U_0 = 12$ cm/s, respectively.

2.4.4 3D Spherical cap

The system is modeled in a 3D configuration, solving numerically the Bousinessq approximation of the Navier-Stokes equations of the system. Instead of doing the simulation of the whole domain, the equations are solved for a representative section of the system (simulation cell), which consists of the whole vertical domain but just a section of the horizontal one. The whole domain is constructed by imposing periodic boundary conditions in the horizontal direction. For the vertical component, an impenetrable spherical cap topography is fixed on the bottom of the simulation cell and a sponge layer is imposed on the top to avoid spurious wave reflections into the physical domain. The flow departs from the rest $\vec{u}(x, y, z)|_{t=0} = 0$ and its velocity is increased with a momentum forcing flow velocity U_0 by an external forcing in the Bousinessq approximation for the Navier-Stokes equations.

A set of 3D numerical simulations are done with the physical parameters described in section 2.2, using the NHM model (Non-Hydrostatic Model) developed by [Aiki and Yamagata, 2004]. The considered 3D simulation cell has a size of $l_x = 10$ m $\times$ $l_y = 4$ m in the horizontal direction and $l_z = 0.98$ m in the vertical direction with a resolution of $\Delta x = \Delta y = \Delta z = 1$ cm.

The same physical parameters, same initial condition, forcing and time step than in section 2.4.3 are used.

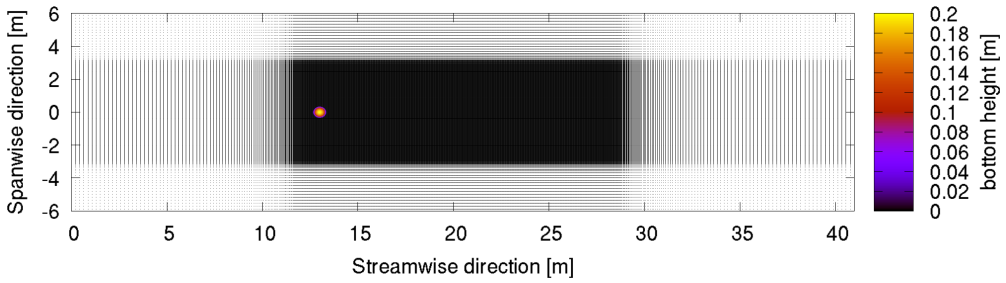

Figure 2.9: Distribution of the grid points at the bottom of the 3D numerical configuration.

2.4.4.1 Size of the physical domain

The 3D simulation volume is conformed by $1000 \times 200 \times 100$ grid points in the x, y and z directions respectively. Periodic boundary conditions are considered along the horizontal directions. The spatial resolution along the x, y and z-directions is $\Delta x = \Delta y = \Delta z = 1$ cm respectively. Thus, the simulation volume measures $L_x \times L_y \times L_z = 10$ m $\times$ 4 m $\times$ 1 m in the x, y and z directions respectively.

Grid stretching

In this configuration, a grid-stretching is applied in all directions. The same vertical grid-stretching is applied as in the 2D configuration. And along the horizontal directions an additional grid-stretching is imposed as can be seen in figure 2.9. The domain's total length along the streamwise direction is $L_x = 42$ m and along the spanwise-direction is $L_y = 6$ m.

2.4.4.2 Boundary conditions

Periodic boundary conditions are applied in the $x-$ and $y-$directions. On the topography, the boundary condition is free-slip.

Topography

Consistently with section 2.2, an impenetrable, uniform, flat bottom with an isolated impenetrable spherical cap placed at the center of the y-domain and at 1 m right of the x-domain's left border is considered as an isolated mountain at the bottom of the domain.

The profile $\eta(x, y)$ of the isolated topography is given by the following expression:

$$eta(x,y) = \begin{cases} \max\left\{\sqrt{R^2 - (x^2+y^2)} - (R-h), 0\right\}, & \text{if } -R \leq \sqrt{x^2+y^2} \leq R \\ 0, & \text{otherwise} \end{cases}$$

where $R = 40$ cm is the sphere's radius, $h = 20$ cm is the topography's height and the z-axis is upwards positive such that $z = 0$ at the bottom (see figure 2.10).

Sponge layer

Along the vertical direction, the same sponge-layer as in 2.4.3 is considered. But an additional sponge layer is imposed along the horizontal direction as described below.

In the experimental configuration, a current is imposed in a cylindrical tank of 13 m diameter. When the fluid flows over the topography, placed at $r_0 = 2$ m from the edge, it

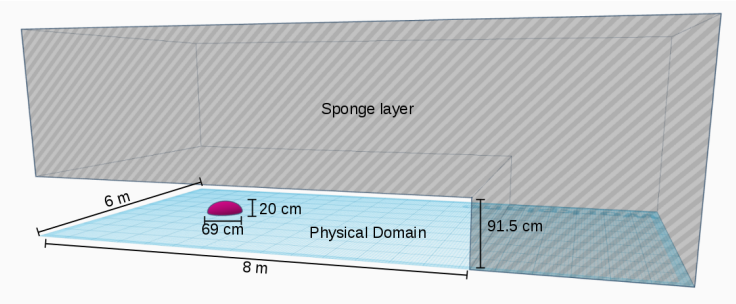

Figure 2.10: Diagram of the 3D numerically simulated setup. The magenta semi-spherical section corresponds to the $h = 20$ cm height, $d = 69$ cm base topography placed on the center of the spanwise direction and at 100 cm from the left streamwise border. The volume colored in gray corresponds to the volume where a sponge layer is acting and the volume comprised between the blue bottom and the gray section corresponds to the simulated physical domain.

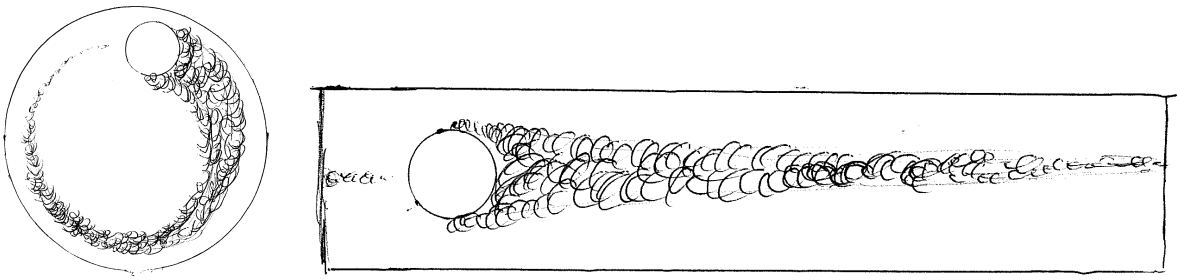

Figure 2.11: Sketch of the numerical setup boundary conditions selection. At the left hand the experimental basic configuration is observed on the right the numerical configuration is observed.

gets perturbed. These perturbations propagate at a speed $U_0 + v'$ downstream. Due to the shape of the tank, after a time $t = \frac{\pi d}{U_0+v'} = \frac{\pi 11m}{U_0+v'}$, these perturbations modify the "new" incoming flow as shown in figure 2.11. To be consistent with experiments, a combination of periodic boundary conditions and an 8 m thick imperfect "filtering force" is applied to the outgoing-incoming flow in order to modulate the incoming streamwise flow as shown in figure 2.10.

2.4.5 Configuration for $U_0 = 12$ cm/s

As it was said in section 2.4.2.5, in order to get the desired flow rate, the flow was started from rest until it gradually reached a speed of U_0. This mechanism acts as a sponge-layer for each time step t: $e^{\frac{(u-U_0)t}{\tau}}$, forcing equally all fluid points. When removed, the flow relaxes the steady-state values.

In steady-state, there are sections of space in which the flow is reversed, so it has deviations $\Delta U = -2U_0$ from the mean flow U_0. Abruptly removing the forcing ramp can cause a shock wave due to the gradient ΔU producing a violation of the CFL condition. To prevent this effect, the ramp was gradually removed in cases of $U_0 = 3$ cm/s and $U_0 = 6$ cm/s.

However, for $U_0 = 12$ cm/s, the time needed to remove the forcing was not numerically viable.

The solution adopted to run the $U_0 = 12\ cm/s$ simulation was to rescale the physical system. The flow rate was reduced from $U_0 = 12$ cm/s to $U_0 = 6$ cm/s keeping the dimensionless parameters constant, i.e. the Froude number $Fr = \frac{U_0}{Nh}$, the Rossby number $Ro = \frac{U_0}{Lf}$ and the Reynolds number ($Re = \frac{U_0 h}{\nu}$).

To preserve the dimensionless ratios constant, if the speed U_0 is halved, then the size of the topography should be halved $L_{12} = \frac{L}{2}$ and $h_{12} = \frac{h}{2}$, the value of the viscosity ν should be reduced to a quarter of its initial value and the values of f and N should be kept constant. Having done this, and because the differences with the speed values at the end of the ramp were smaller, the simulation for 12 cm/s was modified this way. The results shown in the results sections are properly rescaled.

2.5 Pre-analysis of the results

As described in section 2.4.4, it is considered a constant flow $\vec{U}_0 = (U_0, 0, 0)$ flowing over a topography. The flow is perturbed by the interaction with the topography producing velocity deviations $\vec{u}'$. The object of study of this chapter is centered in the velocity deviations $\vec{u}'$ around this constant flow. Nevertheless, the velocity fields obtained from the PIV measurements and from the 3D-NHM simulations are the whole velocity fields, thus, the deviations should be extracted from them.

The components of the total velocity along the vertical and spanwise directions, correspond to the velocity deviations, because the vertical and spanwise velocity components of the incoming flow $\vec{U}_0$, are zero. Along the streamwise direction, the velocity deviations u' are computed by subtracting the incoming streamwise velocity from the total streamwise velocity. In order to do so, the incoming streamwise velocity is computed for each time and depth from a streamwise average over one topography's diameter ($d = 69$ cm) at $1.5d$ ($103\ cm$) at the left of the edge of the topography. Then the incoming velocity is subtracted from the streamwise velocity giving the value of $u'(x, y, z, t)$. Finally, this quantity is time averaged over 20 buoyancy periods ($b.p.$) $\langle u'(x, y, z, t)\rangle_t$. To simplify the notation, in the following chapters, the time-averaged quantity is represented with $u'(x, y, z)$.

3

Linear lee wave theory

3.1 Introduction

When a stratified fluid flows over a solid obstacle, internal gravity waves are emitted in the lee part of the obstacle, such waves are called lee waves; if the obstacle is a mountain range these waves are called mountain waves [Wurtele et al., 1993]. These waves may generate a cascade of energy and break near the topography or can be stable enough to travel and break away the topography. In any of these cases, understanding breaking could be interesting either because of the influence on the obstacle or in the mean-flow.

Linear theory can predict the general behavior of internal gravity waves, but it does not when non-linearities become important. These non-linearities may become important due to (i) amplification produced by a decrease in density, as goes upwards in the fluid, (ii) mountain range, and (iii) dynamically singular levels in the fluid field. The non-linearities produce a complicated behavior such as a large departure of the streamlines from their equilibrium levels, strong winds, generation of small scales, turbulence, etc. These imply a hazard to aircraft and can interact with the mean flow having an impact over global weather forecasts and climatological momentum balance [Wurtele et al., 1993].

Linear theory assumes the height h of the hills is small compared with their horizontal extent λ_T [Sutherland and Linden, 2002], so the linear approximation can be taken in $\vec{u} \cdot \nabla(z - h) = 0$ to be $w(x, y, z = h \approx 0) = U\frac{\partial h}{\partial x}$ [Dalziel et al., 2011]. When the topographic object satisfies this aspect ratio, it is said to be a "flat topography" [Voisin, 2007]. Nevertheless, this condition is not sufficient to guarantee linearity: for a high flow speed: steep large-amplitude waves might be generated and turbulence may cause boundary layers to thicken to non-negligibly size [Baines and Hoinka, 1985].

As said in the previous section, the main objective of this work is to describe the interaction between an isolated topography and constant-uniform flow with velocity U_0, which flows over an isolated flat mountain. For the Froude numbers described in section 2.2, both a wake and a wave field are emitted. In this chapter, a theoretical description of the pro-

duced internal gravity waves is done in the linear lee wave theory approximation. As an improvement to linear theory, the dividing stream line hypothesis (DSL) is considered. The obtained velocity fields are compared with PIV experimental results in order to evaluate the validity of the DSL.

The velocity fields are computed for the topography described in chapter 2 with and without rotation. For the non-rotating case, two different approaches are adopted: on the one hand, the velocity fields are numerically computed using the inverse Fast Fourier Transform (iFFT) FORTRAN's intrinsic subroutine. On the other hand, the inverse Fourier transform was analytically computed in the far-field approximation by Bruno Voisin. His results are here included and compared with the ones obtained numerically in section 3.3.1. In this section, the validity of the dividing streamline hypothesis and the far-field approximation are studied by comparing with the experimental results.

For the rotating case, the velocity fields are computed numerically using as well the FORTRAN's iFFT and its results are analyzed and compared with the experimental results in section 3.3.2. In this section, the impact rotation in the IGW field's structure is analyzed. Finally, the conclusions and perspectives are presented at the end of this chapter.

3.2 Internal gravity waves

A stably stratified fluid with vertical density profile $\rho(z)$ is considered. Let us consider a fluid element at a depth z_0 with density $\rho(z_0)$, as the fluid around it has the same density, we can define its potential buoyancy energy as 0 at this depth. If we move adiabatically vertically this fluid element to a new depth $z_0+\epsilon$, this fluid element would be subjected to a buoyancy force associated to a potential energy $U(z_0+\epsilon) = [\rho(z_0+\epsilon) - \rho(z_0)]\, g\epsilon$. If $\epsilon < 0$, then, $\rho(z_0+\epsilon) > \rho(z_0)$, the potential energy would increase. Now, if $\epsilon > 0$, $\rho(z_0+\epsilon) < \rho(z_0)$ so the potential energy would also increase. That is, the position z_0 is the stable equilibrium position and any disturbance would produce an oscillation around this equilibrium position [Landau and Lifshitz, 1970]. As the restoring force $-\frac{U(z_0+\epsilon)-U(z_0)}{\epsilon} = [\rho(z_0+\epsilon) - \rho(z_0)]\, g$ is the buoyancy force or the reduced gravity, the oscillation frequency $N = \sqrt{\frac{g}{\rho_0}\frac{\delta\rho}{\delta z}}$ is known as buoyancy frequency and the waves which are produced through this mechanism are called gravity waves [Wurtele et al., 1993]. Additionally, as these waves occur in the fluid's interior, they are called internal gravity waves [Sutherland, 2010,Brekhovskikh and Goncharov, 1993].

Some times the production of gravity waves might be undesirable, one example is the dead water effect, which appears that a ship moving in the ocean spends a considerable part of its power for gravity waves generation [Brekhovskikh and Goncharov, 1993]. This effect was reproduced experimentally by [Mercier et al., 2011] with a toy ship that moves with a fixed power[1]. Here, a boat moving at fixed power is considered. This boat increases its velocity producing gravity waves, up to a maximum value. Then, the ship velocity decreases and becomes nearly zero. When the ship stops, there is no production of gravity waves. So,

[1]Follow this link https://www.youtube.com/watch?v=bzcgAshAg2o to see a video of the experiment.

the amount of energy spent in generating gravity waves decreases as well, and the velocity increases again.

3.2.1 Linear lee waves

Lee waves are one kind of internal gravity waves, that form in the lee part of a topographic obstacle when a stably stratified fluid flows over this topography. We consider that this fluid is flowing at a constant velocity U_0 over a single isolated topography η of height h and diameter d where $h \ll d$. Because of the chosen topographic aspect ratio, the topography is said to be flat [Voisin, 2007] and it can be described as a Monge surface $\eta = \eta(x, y)$ [Struik, 1961].

Choosing a Cartesian system of coordinates with the $x-axis$ aligned with the incoming flow direction, so, $\vec{U_0} = (U_0, 0, 0)$. Writing the fluid velocity as $\vec{u} = \vec{u'} + \vec{U_0}$ with $\vec{u'} = (u', v', w')$. Assuming that $|\vec{u'}| \ll U_0$, the system of equations (2.9) can be linearized at first order for the steady lee wave field [Voisin, 2007, Dalziel et al., 2011] as follows,

$$\rho_0 U_0 \frac{\partial u'}{\partial x} = -\frac{\partial p'}{\partial x} + f v' \rho_0, \tag{3.1a}$$

$$\rho_0 U_0 \frac{\partial v'}{\partial x} = -\frac{\partial p'}{\partial y} - f u' \rho_0, \tag{3.1b}$$

$$\rho_0 U_0 \frac{\partial w'}{\partial x} = -\frac{\partial p'}{\partial z} - \rho g, \tag{3.1c}$$

and the equation (2.12),

$$U_0 \frac{\partial \rho'}{\partial x} = \rho_0 \frac{N^2}{g} w', \tag{3.2}$$

$$\frac{\partial u'}{\partial x} + \frac{\partial v'}{\partial y} + \frac{\partial w'}{\partial z} = 0. \tag{3.3}$$

One additional equation should be included to consider the topographic effect. In the frame of reference attached to the fluid, the topography is moving backward at a velocity $-\vec{U_0} = (-U_0, 0, 0)$. Considering that the mountain is impenetrable, the boundary condition at the topographic surface is

$$w'(x, y, z = \eta(x, y)) = \frac{D\eta(x, y)}{Dt} = (u' + U_0) \frac{\partial \eta}{\partial x}(x, y).$$

As previously commented in chapter 2, it is considered a flat topography ($h \ll d$) immersed in a water layer of a depth $H = 1$ m, which is $H \gg h$. Under these assumptions, applying the impenetrability boundary condition at the topographic surface $z = \eta(x, y)$ is, at first order in h, equivalent to apply it at $z = 0$, so

$$w'(x, y, z = 0) \approx w'(x, y, z = \eta) = (u' + U_0) \frac{\partial \eta}{\partial x}(x, y).$$

In the linear approximation, $|\vec{u}'| \ll U_0$, the velocity perturbations u' are neglectable compared with the incoming flow velocity U_0, then,

$$w'(x, y, z = 0) \approx U_0 \frac{\partial \eta}{\partial x}(x, y). \tag{3.4}$$

In order to simplify notation, from now on $u \equiv u'$, $v \equiv v'$, $w \equiv w'$, $p \equiv p'$ and $\rho \equiv \rho'$.

To easily deal with the derivatives, the system will be studied by using the Fourier space. We consider a differentiable and integrable function $\Phi(\vec{r})$ which vanishes at infinity $\lim_{|\vec{r}|\to\infty} \Phi(\vec{r}) = 0$, then the 3D-Fourier transform of Φ is defined as:

$$\hat{\Phi}(\vec{k}) = \int_{-\infty}^{\infty} \Phi(\vec{r}) e^{-i\vec{k}\cdot\vec{r}} d^3\vec{r}, \tag{3.5}$$

and the inverse Fourier transform,

$$\Phi(\vec{r}) = \frac{1}{(2\pi)^3} \int_{-\infty}^{\infty} \hat{\Phi}(\vec{k}) e^{i\vec{k}\cdot\vec{r}} d^3\vec{k}, \tag{3.6}$$

the Fourier Transform of the partial derivative with respect to $x_l \in \{x, y, z\}$ of the function $\Phi(\vec{r})$ is given by [Arfken and Weber, 2005]:

$$\widehat{\frac{\partial \Phi(\vec{r})}{\partial x_l}} = i k_l \hat{\Phi}(\vec{k}). \tag{3.7}$$

To solve the problem in the Fourier space, an equivalent problem is solved. Here the domain is extended onto the whole $z-$axis by adding the topography's mirror image $z = -\eta(x, y)$ at $z = 0$. The boundary condition on either side of the plane $z = 0$

$$w(x, y, z = \pm 0) = \pm U_0 \frac{\partial \eta}{\partial x}(x, y)$$

induces a velocity adding a source term in the equation of continuity, [Voisin, 2007]:

$$\frac{\partial u}{\partial x} + \frac{\partial v}{\partial y} + \frac{\partial w}{\partial z} = \left[w(z = 0_+) - w(z = 0_-)\right] \delta(z) = q(x, y, z), \tag{3.8}$$

where $q(x, y, z) = 2U_0 \frac{\partial \eta(x,y)}{\partial x} \delta(z)$

Using equation (3.7), the equations (3.1) can be written in the Fourier space as

$$i\rho_0 U_0 k_x \hat{u} = -ik_x \hat{p} + f\hat{v}\rho_0, \tag{3.9a}$$

$$i\rho_0 U_0 k_x \hat{v} = -ik_y \hat{p} - f\hat{u}\rho_0, \tag{3.9b}$$

$$i\rho_0 U_0 k_x \hat{w} = -ik_z \hat{p} - \hat{\rho} g, \tag{3.9c}$$

in the same way, equation (3.2) can be rewritten as,

$$iU_0 k_x \hat{\rho} = \rho_0 \frac{N^2}{g} \hat{w}, \tag{3.10}$$

and for equation (3.3),

$$ik_x \hat{u} + ik_y \hat{v} + ik_z \hat{w} = \hat{q}, \tag{3.11}$$

with $\hat{q}(\vec{k}) = 2iU_0 k_x \hat{\eta}(k_x, k_y)$.

This system of equations can be represented in matrix notation as

$$\begin{bmatrix} -iU_0k_x\rho_0 & f\rho_0 & 0 & -ik_x & 0 \\ -f\rho_0 & -iU_0k_x\rho_0 & 0 & -ik_y & 0 \\ 0 & 0 & -iU_0k_x\rho_0 & -ik_z & -g \\ 0 & 0 & -N^2\rho_0/g & 0 & iU_0k_x \\ ik_x & ik_y & ik_z & 0 & 0 \end{bmatrix} \begin{bmatrix} \hat{u} \\ \hat{v} \\ \hat{w} \\ \hat{p} \\ \hat{\rho} \end{bmatrix} = \begin{bmatrix} 0 \\ 0 \\ 0 \\ 0 \\ \hat{q} \end{bmatrix},$$

Using the Gauss-Jordan method, with $k_H^2 = k_x^2 + k_y^2$ and $k^2 = k_x^2 + k_y^2 + k_z^2$, the formal solution is given by

$$\begin{bmatrix} \hat{u} \\ \hat{v} \\ \hat{w} \\ \hat{p} \\ \hat{\rho} \end{bmatrix} = \frac{-i\hat{q}}{U_0 k_x (N^2 k_H^2 + f^2 k_z^2 - k^2 (U_0 k_x)^2)} \begin{bmatrix} (U_0 k_x^2 - i f k_y)(N^2 - U_0^2 k_x^2) \\ (U_0 k_x k_y + i f k_x)(N^2 - U_0^2 k_x^2) \\ U_0 k_x k_z (f^2 - U_0^2 k_x^2) \\ \rho_0 (f^2 - U_0^2 k_x^2)(N^2 - U_0^2 k_x^2) \\ -iN^2 \rho_0 k_z (f^2 - U_0^2 k_x^2)/g \end{bmatrix}. \tag{3.12}$$

To compute the velocity field it is necessary to compute the inverse Fourier transform of the first three components of (3.12),

$$u = -\frac{i}{(2\pi)^3} \int \frac{1}{\frac{U_0^2 k_x^2 - N^2}{U_0^2 k_x^2 - f^2} k_H^2 + k_z^2} \left(\frac{U_0^2 k_x^2 - N^2}{U_0^2 k_x^2 - f^2} \right) \left(k_x - i \frac{f k_y}{U_0 k_x} \right) \hat{q} e^{i\vec{k}\cdot\vec{x}} d^3k, \tag{3.13a}$$

$$v = -\frac{i}{(2\pi)^3} \int \frac{1}{\frac{U_0^2 k_x^2 - N^2}{U_0^2 k_x^2 - f^2} k_H^2 + k_z^2} \left(\frac{U_0^2 k_x^2 - N^2}{U_0^2 k_x^2 - f^2} \right) \left(k_y + i \frac{f}{U_0} \right) \hat{q} e^{i\vec{k}\cdot\vec{x}} d^3k, \tag{3.13b}$$

$$w = -\frac{i}{(2\pi)^3} \int \frac{k_z}{\frac{U_0^2 k_x^2 - N^2}{U_0^2 k_x^2 - f^2} k_H^2 + k_z^2} \hat{q} e^{i\vec{k}\cdot\vec{x}} d^3k. \tag{3.13c}$$

As the spectrum $\hat{q}(\vec{k})$ does not depend on the vertical wavenumber k_z, we compute the integral along the vertical wavenumber k_z by the application of Cauchy's theorem and Jordan's lemma. For this purpose, we retain the pole:

$$k_{z_0} = i \left[\frac{(U_0 k_x - i\epsilon)^2 - N^2}{(U_0 k_x - i\epsilon)^2 - f^2} \right]^{1/2} k_H \ \mathrm{sgn}(z), \tag{3.14}$$

where $0 \lesssim \epsilon \ll 1$, giving

$$\sqrt{N^2 - U_0^2(k_x - i\epsilon)^2} = \begin{cases} \sqrt{|N^2 - U_0^2 k_x^2|}, & \left(|k_x| < \frac{N}{U_0}\right) \\ i\sqrt{|N^2 - U_0^2 k_x^2|}\ \mathrm{sgn} k_x, & \left(|k_x| > \frac{N}{U_0}\right) \end{cases}$$

and

$$\sqrt{U_0^2(k_x - i\epsilon)^2 - f^2} = \begin{cases} \sqrt{|U_0^2 k_x^2 - f^2|}\ \mathrm{sgn} k_x, & \left(|k_x| > \frac{f}{U_0}\right) \\ -i\sqrt{|U_0^2 k_x^2 - f^2|}, & \left(|k_x| > \frac{f}{U_0}\right) \end{cases}$$

so that,

$$k_{z_0} = \begin{cases} i\sqrt{\left|\frac{U_0^2 k_x^2 - N^2}{U_0^2 k_x^2 - f^2}\right|} k_H\ \mathrm{sgn} k_z, & \left(|k_x| > \frac{N}{U_0} \quad \text{or} \quad |k_x| < \frac{f}{U_0}\right) \\ \sqrt{\left|\frac{N^2 - U_0^2 k_x^2}{U_0^2 k_x^2 - f^2}\right|} k_H\ \mathrm{sgn} k_z\ \mathrm{sgn} k_x, & \left(\frac{f}{U_0} < |k_x| < \frac{N}{U_0}\right) \end{cases}$$

For $|k_x| > \frac{N}{U_0}$ or $|k_x| < \frac{f}{U_0}$ only evanescent waves exist vanishing as $|z| \to \infty$. These waves were not taken into account in the iFFT numerically computed fields by setting to zero their amplitudes. For $\frac{f}{U_0} |k_x| < \frac{N}{U_0}$, the radiation condition is satisfied, so propagating waves exist.

In the frame of reference where the flow is at rest, the topographic obstacle generates the waves by moving at the velocity $-U_0 \hat{\imath}$ and satisfies the Doppler relation $\omega = -U_0 k_x$. We choose the pole k_{z_0} in such a way that the group velocity points away from the topography, upwards for $z > 0$, and downwards for $z < 0$, in the fictitious plane. The equation (3.14) gives the dispersion relation for lee waves under rotation

$$\omega^2 = \frac{k_H^2 N^2 + k_z^2 f^2}{k^2}, \tag{3.15}$$

if we set $f = 0\ \mathrm{s}^{-1}$ in this equation, the result is consistent with that reported for lee-waves [Lighthill, 1978].

Integrating equations (3.13) over k_z, gives

$$u = \frac{1}{2(2\pi)^2} \int \sqrt{\frac{N^2 - U_0^2 k_x^2}{U_0^2 k_x^2 - f^2}} \left(\frac{k_x}{k_H} + i\frac{f k_y}{U_0 k_x k_H}\right) \hat{q} e^{i\sqrt{\frac{N^2 - U_0^2 k_x^2}{U_0^2 k_x^2 - f^2}} k_H z + i\vec{k}_H \cdot \vec{x}_H} dk_x dk_y, \tag{3.16a}$$

$$v = \frac{1}{2(2\pi)^2} \int \sqrt{\frac{N^2 - U_0^2 k_x^2}{U_0^2 k_x^2 - f^2}} \left(\frac{k_y}{k_H} - i\frac{f}{U_0 k_H}\right) \hat{q} e^{i\sqrt{\frac{N^2 - U_0^2 k_x^2}{U_0^2 k_x^2 - f^2}} k_H z + i\vec{k}_H \cdot \vec{x}_H} dk_x dk_y, \tag{3.16b}$$

$$w = \frac{1}{2(2\pi)^2} \int \hat{q} e^{i\sqrt{\frac{N^2 - U_0^2 k_x^2}{U_0^2 k_x^2 - f^2}} k_H z + i\vec{k}_H \cdot \vec{x}_H} dk_x dk_y, \tag{3.16c}$$

where $k_x = k_x + i\epsilon$ with $\epsilon \ll 1$.

The set of integrals (3.16) can be obtained for the non-rotating case by taking $f = 0\ \mathrm{s}^{-1}$. The integral formal structure for the vertical velocity for the rotating case is the same as

the non-rotating case. There is only one difference: the value of k_{z_0} in the argument of the exponential. From here, to have propagating waves, their frequency $\omega = U_0 k_x$ should satisfy $f < \omega < N$. This is as well consistent with the non-rotating case, where to have propagating internal gravity waves $0 < \omega < N$. To compute such integrals, it is necessary to choose a specific topography shape. We choose a particular shape in the following section 3.3, where the integrals are computed for the topography considered in chapter 2.

3.3 Application to an isolated spherical cap topography

Up to this point, we have considered a flat, arbitrary shaped topography $\eta(\vec{r}_H, t)$, which exerts a unitary force $q(\vec{r}, t)$ per unit volume, per unit time over the fluid, with a well-defined Fourier transform $\hat{q}(\vec{k}, \omega)$. From now on, we will choose the same physical parameters as in [Sommeria et al., 2016]. In both cases, periodic boundary conditions are applied along the streamwise direction. But, here we consider an infinite radius of curvature, $R_{curv} = \infty$, instead of the radius of curvature of the rotating tank, $R_{curv} = 6.5$ m, in such a way that the unperturbed non-rotating streamwise current lines would be always aligned with the x-axis of the Cartesian coordinate system fixed to the topography. The system's rotation is included in the movement equations by the Coriolis parameter f.

As we described in chapter 2, we consider an spherical cap of topographic profile $\eta(x, y)$, height $h = 20$ cm and radius of curvature $R = 40$ cm, placed on a fully flat bottom. We choose the system of coordinates in such a way that the origin is vertically placed at the domain bottom and is horizontally centered at the topography's center. Thus, the topographic profile can be represented with the following expression:

$$\eta(x, y) = \left(\sqrt{R^2 - r_H^2} - R + h\right) \Theta\left(\sqrt{R^2 - r_H^2} - R + h\right), \tag{3.17}$$

with $\vec{r}_H = (x, y, 0)$, $r_H = |\vec{r}_H|$ and $\Theta(x)$ the Heaviside function defined by

$$\Theta(x) = \begin{cases} 1, & \text{if } x \geq 0 \\ 0, & \text{if } x < 0 \end{cases}$$

In this chapter, we consider the three different flow rates considered in chapter 2: $U_0 =$ 3 cm/s, 6 cm/s and 12 cm/s corresponding to the Froude numbers $Fr = \frac{U_0}{Nh}$; $Fr_{3\ \text{cm/s}} = 0.31$, $Fr_{6\ \text{cm/s}} = 0.62$ and $Fr_{12\ \text{cm/s}} = 1.25$. The system is studied with ($f = 0.19\ \text{s}^{-1}$, $\frac{f}{N} = 0.39$) and without rotation ($f = 0\ \text{s}^{-1}$, $\frac{f}{N} = 0$).

When a density stratified fluid flows over a topography, all or part of the current can flow around it. As previously commented in section 3.2, in the considered stratified fluid, a vertical displacement δz of a fluid volume of density ρ_0 requires a work $\delta W = -g\delta\rho_0'(\delta z)^2$, with $\delta\rho_0' = \rho_0(\delta z) - \rho(0)$. If the flow has not enough kinetic energy to rise over the topography

of height h, a portion of the fluid flows around the topography with quasi-horizontal motion and does not produce internal waves. There is still a portion of the fluid that flows above it, exciting a lee wave field [Sommeria et al., 2016].

These two sections are separated by a dividing streamline [Sheppard, 1956] (DSL) at a vertical level such that the kinetic energy has the same value as the potential energy, so, at this level, $Fr_{\text{local}} = 1$. From the Froude number definition, the above remaining effective height h_{eff} of the cap that is involved in the wave emission is: $h_{\text{eff}} = \frac{U_0}{N}$. But, if all the fluid has enough kinetic energy to pass over the topography, $Fr > 1$, then the whole topography height h is involved in the wave emission [Voisin, 2007, Dalziel et al., 2011, Baines, 1995].

As we already mentioned, the DSL hypothesis establishes that for $Fr < 1$, there is only a section of the topography involved in the wave emission: the section above the horizontal plane at a height $h_s = (1 - Fr)h$. This means that the topographic effective height for the wave production is $h_{\text{eff}} = hFr$. Taking into account the DSL hypothesis, h should be replaced by h_{eff}, the effective topographic profile is

$$\eta(x, y) = \left[(R^2 - r_H^2)^{1/2} - R + hFr\right] \Theta\left(-r_H^2 + 2hRFr - (hFr)^2\right), \tag{3.18}$$

and it is applied at $z = h_{\text{s}}$

The profiles for the different Froude numbers considered in this work are presented in figure 3.1. The green line located at $h_{\text{s}} = 13.8$ cm indicates the DSL for $Fr = 0.31$, and the red line located at a height $h_{\text{s}} = 7.6$ cm, indicates the DSL for $Fr = 0.62$. Thus, the effective size of the topography h_{eff} corresponds to the part of the topography above this line being $h_{\text{eff}} = 6.2$ cm and $h_{\text{eff}} = 12.4$ cm, for $Fr = 0.31$ and $Fr = 0.62$, respectively.

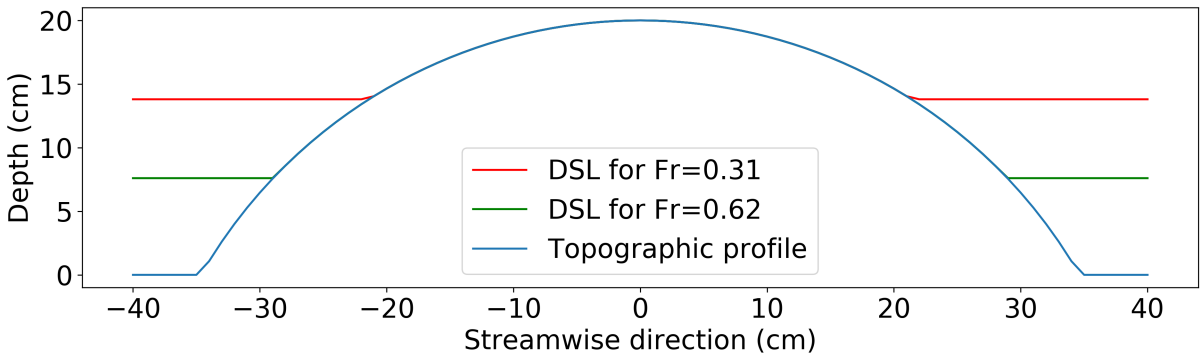

Figure 3.1: Diagram of topography and the levels of the DSL for each considered velocity. The DSL height for $Fr = 0.31$ is $h_{\text{s}} = 13.8$ cm and for $Fr = 0.62$ is $h_{\text{s}} = 7.6$ cm with effective sizes of $h_{\text{eff}} = 6.2$ cm and $h_{\text{eff}} = 12.4$ cm, respectively.

There are two differences between modeling the effective topography (using the DSL hypothesis) and the topography considered in the preceding section. Firstly, the topography is no longer located on the ground $z = 0$, but it is located on the DSL $z = h_{\text{s}}$. Secondly, this plane does not behave like the rigid ground at $z = 0$, in the sense that it does not reflect waves, it absorbs them instead. Given this, purely horizontal motions exist below the DSL,

thus, the boundary conditions at the plane $z = h_s$ are:

$$\begin{aligned} w(\vec{r}_H, z = h_{s_+}) &= U_0 \frac{\partial \eta}{\partial x}(\vec{r}_H), \\ w(x, y, z = h_{s_-}) &= 0, \end{aligned}$$

giving,

$$q(\vec{x}) = U_0 \frac{\partial \eta}{\partial x}(\vec{r}_H)\delta(z - h_s), \quad \hat{q}(\vec{k}) = iU_0 k_x \hat{\eta}(\vec{k}_H) e^{-ik_z h_s}$$

This is the phenomenological streamline model introduced by [Voisin, 2007].

For $Fr < 1$, $r_H \sim (2hFrR)^{1/2} \ll R$ so, $\eta(x, y) \sim hFr - \frac{r_H^2}{2R}\Theta\left[(2RhFr)^{1/2} - |r_H|\right]$, the source becomes,

$$q(\vec{r}) = -U_0 \frac{x}{R}\Theta\left[(2RhFr)^{1/2} - |r_H|\right]\delta(z - h_s) \tag{3.19}$$

and its Fourier transform,

$$\hat{q}(\vec{k}) = 4\pi i h U_0 Fr \frac{J_2\left[k_H R(2Fr)^{1/2}\right]}{k_H} \frac{\vec{k}_x}{k_H} e^{-ik_z h_s}, \tag{3.20}$$

where $J_2(x)$ is the second order Bessel function of the first kind. Equation (3.20) represents the source of waves in the system in Fourier space.

We computed the set of integrals (3.16) and the corresponding equations for the case without rotation for the physical parameters above described to obtain the velocity field. This set is computed by using two different methods: Analytically, by Bruno Voisin, in the far-field approximation, and numerically using the intrinsic FORTRAN iFFT subroutine. The numerical solution is computed from the iFFT of equation (3.19) then its result is used to express equations (3.16). Finally, the iFFT of these integrals are computed and presented in 1) section 3.3.1. In this figure, the case without rotation is computed using the iFFT and compared with the experimental results obtained with the configuration described in the previous chapter 2. These numerically computed integrals are as well compared with the analytically computed solution in the far-field approximation done by Bruno Voisin. And in 2) section 3.3.2, the iFFT numerically computed solutions for these integrals are shown and compared with the experimental results. As the equations become unmanageable for the rotating case, we do not present a far-field approximation for the rotating case.

3.3.1 Non-rotating case

In this subsection, the set of integrals shown in equation (3.16) with (3.20) are computed for the non rotating case. We compare two different approaches: the results of the iFFT numerically computed integrals and the analytically computed ones. The iFFT numerically computed results are computed for two cases: with and without the DSL hypothesis.

Figure 3.2 shows the streamwise velocity field computed numerically along the vertical

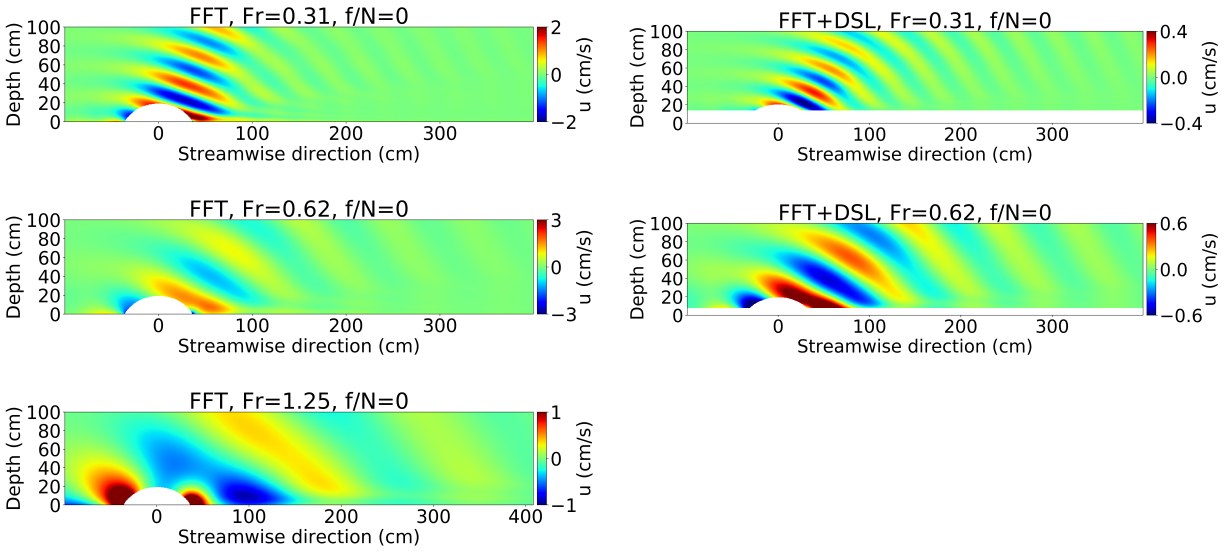

Figure 3.2: Vertical cross-section along the central-streamwise axis of the streamwise velocity field 1) on the left: iFFT computed 2) on the right: iFFT computed +DSL. In the first row $Fr = 0.31$, in the second row $Fr = 0.62$, and in the third row $Fr = 1.25$. The wave amplitude observed without DSL is five times larger than the one obtained with DSL.

plane aligned over the central-streamwise axis. On the left hand is the computation without the DSL and on the right hand are the results with the DSL hypothesis. As a first remark is observed that the non-DSL wave amplitude is $u' \sim \frac{U_0}{2.5}$, while the wave amplitude observed for $FFT + DSL$ is $u' \sim \frac{U_0}{10}$. A second remark is that, as was expected, the group wave vector seems to not be affected by the inclusion or exclusion of the DSL hypothesis.

In order to determine the validity of the DSL hypothesis, we compare the PIV experimental results. For this purpose a horizontal cut of the velocity field observed in figure 3.2 at $3h = 60$ cm is done and compared with the same cut of the PIV results of the experiments described in chapter 2; these cuts are shown in figure 3.3.

The fact that the introduction of the dividing streamline hypothesis involves a significant correction to the amplitude of the waves can be explained in terms of the boundary condition. The amplitude of the waves is fixed through the boundary condition in the topography for the vertical component of the velocity $w \sim U_0 h_{\text{eff}}$. From this we see that not including the dividing streamline height in linear theory implies an overestimation of the wave amplitude by a factor of $1/Fr$. Specifically, for $Fr = 0.31$, the wave amplitude calculated without dividing streamline would be ~ 3 times greater than the real value, which is precisely the case.

In figure 3.3 is observed that the theoretical solution which includes the DSL hypothesis has a better agreement with the experimental results than the theoretical results which do not. Using the DSL hypothesis in the linear theory computation produces an important correction to the amplitude of the waves and a small correction to the measured wavelength. A bigger impact is observed for $Fr = 0.31$ because in this case only one-third of the topography height is associated with the lee wave production. For $Fr = 0.62$ and $Fr = 1.25$, linear

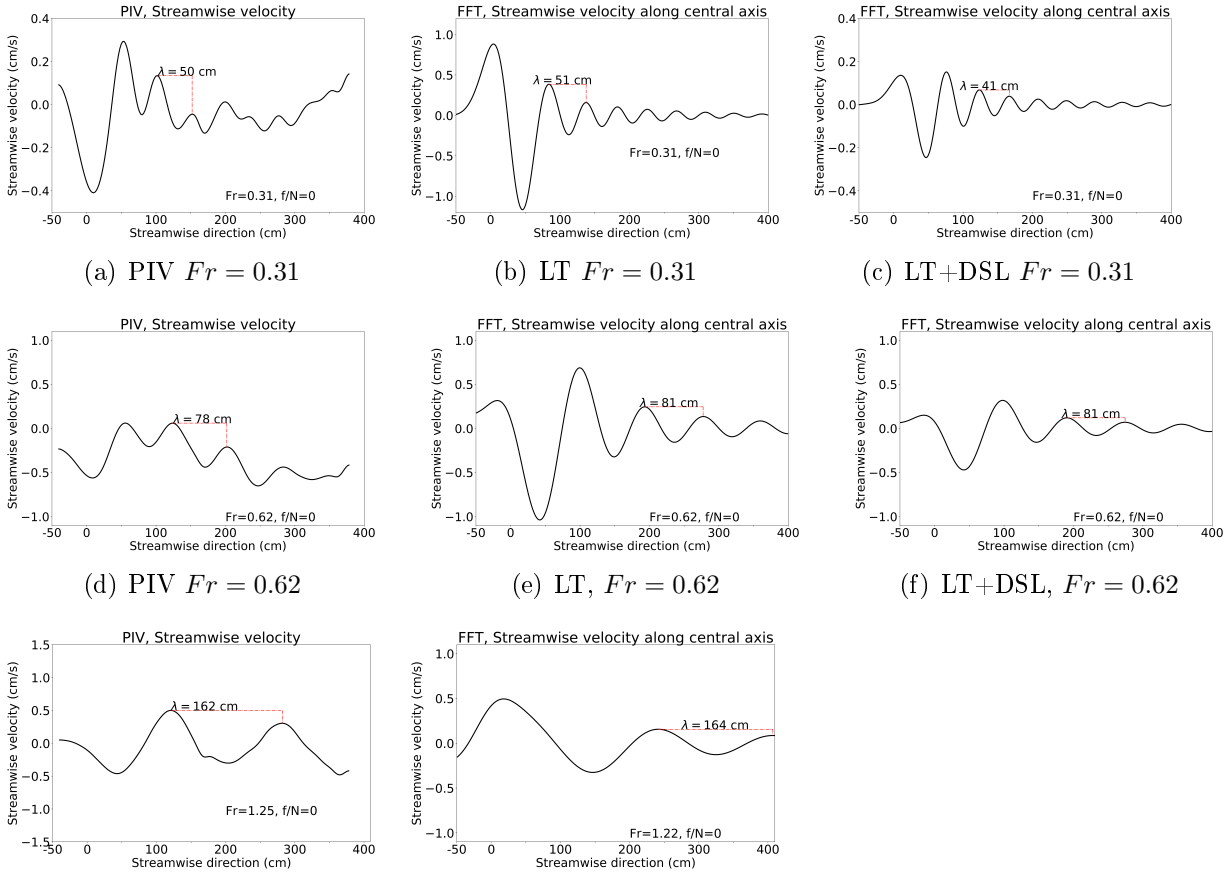

(a) PIV $Fr = 0.31$ (b) LT $Fr = 0.31$ (c) LT+DSL $Fr = 0.31$

(d) PIV $Fr = 0.62$ (e) LT, $Fr = 0.62$ (f) LT+DSL, $Fr = 0.62$

(g) PIV $Fr = 1.25$ (h) LT, $Fr = 1.25$

Figure 3.3: Stream-wise velocity along the central-streamwise axis at the topography axis at $z = 60$ cm (3 topography heights) above the bottom, for $Fr = 0.31$ (first row), $Fr = 0.62$ (second row), and $Fr = 1.25$ (bottom). The PIV experimental measurements done by [Sommeria et al., 2016] are shown in the left column. Linear theory results are shown in the central column. Linear theory results considering the DSL hypothesis are shown in the right column. We recall that, there is no DSL for $Fr > 1$.

theory also provides a good description of the measured wave amplitude and wavelength as observed in figure 3.3. Because including the DSL hypothesis provides an important correction to the wave amplitudes, from now on all the theoretical results here presented include this hypothesis.

In the far-field $\frac{Nr}{U_0} \gg 1$ for the non-rotating case ($f/N = 0$), an analytical expression for the wave field was obtained by [Voisin, 2007] which in spherical coordinates (r, θ, ϕ) defined by

$$x = r\cos\theta, \quad y = r\sin\theta\cos\phi, \quad z = h_s + r\sin\theta\sin\phi, \tag{3.21}$$

can be written as:

$$\vec{u} = \frac{2U_0^2}{Nr}\Theta(x)J_2\left\{\left[\frac{2+2\cot^2\theta\cos^2\phi}{Fr\frac{h}{R}}\right]^{1/2}\cos\theta\sin\phi\right\}\frac{(\tan\theta\csc\phi,-\cot\phi,-1)}{(1+\cot^2\theta\cos^2\phi)^{1/2}}\sin\left(\frac{Nr}{U_0}\sin\phi\right), \tag{3.22}$$

where $\Theta(x)$ is the Heaviside function.

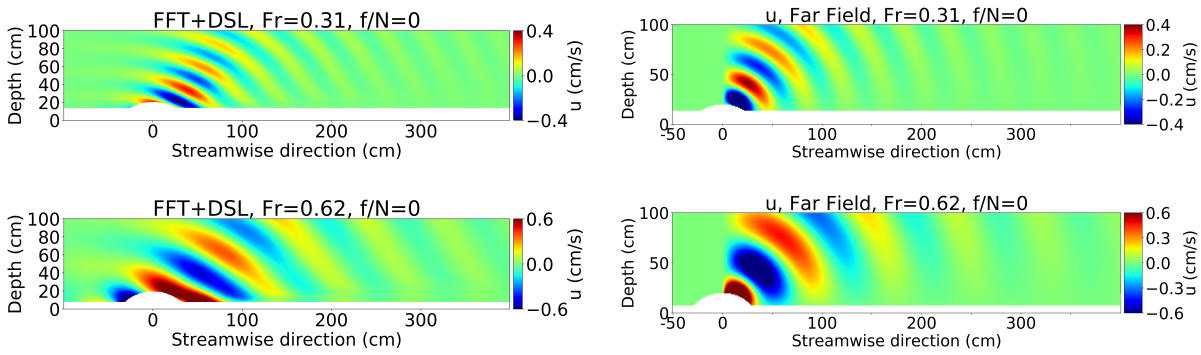

Figure 3.4: Vertical cross-section along the central-streamwise axis of the streamwise velocity field 1) on the left: iFFT computed 2) on the right: analytically computed in the far field approximation. In the first row $Fr = 0.31$ and in the second row $Fr = 0.62$.

Because of the criteria $\frac{Nr}{U_0} \gg 1$, the observation distance should be much bigger than 6.25 cm, 12.5 cm and 25 cm, for $Fr = 0.31$ ($U_0 = 3$ cm/s), $Fr = 0.62$ ($U_0 = 6$ cm/s) and $Fr = 1.25$ ($U_0 = 12$ cm/s), respectively. As the system has a total depth of 100 cm, we only consider this solution for the two lower Froude numbers. The streamwise component of the equation (3.22) is plotted for $Fr = 0.31$ and $Fr = 0.62$ in figure 3.4 and the vertical component is plotted in figure 3.5. The corresponding iFFT numerically computed solutions are plotted as well in these figures. Since the physical domain that is below the DSL cannot be computed, this region is masked in white for all the figures.

Figure 3.4 shows the wave field from the deviations of the streamwise component velocity. On the left hand is shown the numerical solution, and on the right hand, the analytically obtained field in the far-field approximation. These figures show that the far-field approximation provides with a good agreement in the general structure of the waves and agrees with the amplitude for distances of the order of $3h$. The wave field computed from the far-field does not provide a prediction for the upstream wave field whereas the iFFT numerically computed field does. We observe as well that the group velocity vector makes the same angle with the vertical axes and the prediction of the far-field approximation is in better agreement for the case with $Fr = 0.31$ than for the case with $Fr = 0.62$, as expected from the criteria $\frac{Nr}{U_0} \gg 1$.

Figure 3.5 shows the vertical velocity field which is phase-shifted $\frac{\pi}{2}$ with the wave field observed from the streamwise velocity. This figure shows a good agreement between the far-field approximation and the iFFT numerically computed field. In the iFFT numerically computed field, the waves are strongly damped near the DSL zone, but in the far-field

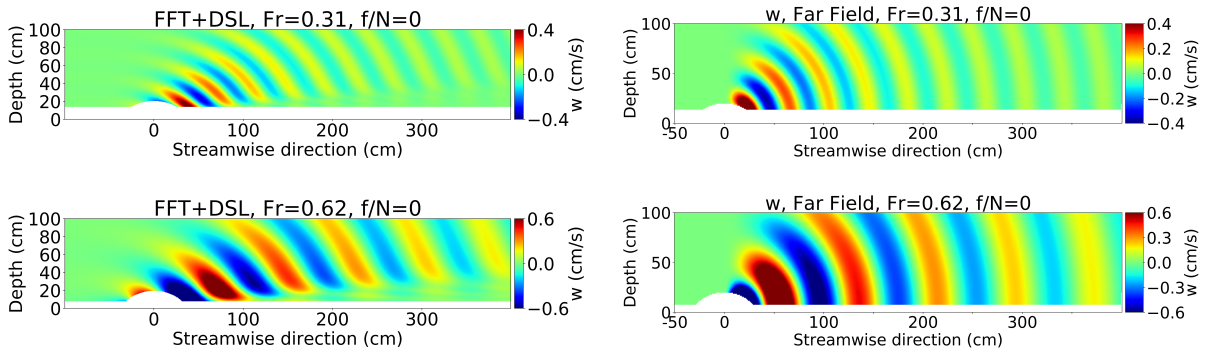

Figure 3.5: Vertical plane cut of the vertical velocity field analytically computed in the far field approximation along the central-streamwise axis. At the top $Fr = 0.31$ and at the second line $Fr = 0.62$.

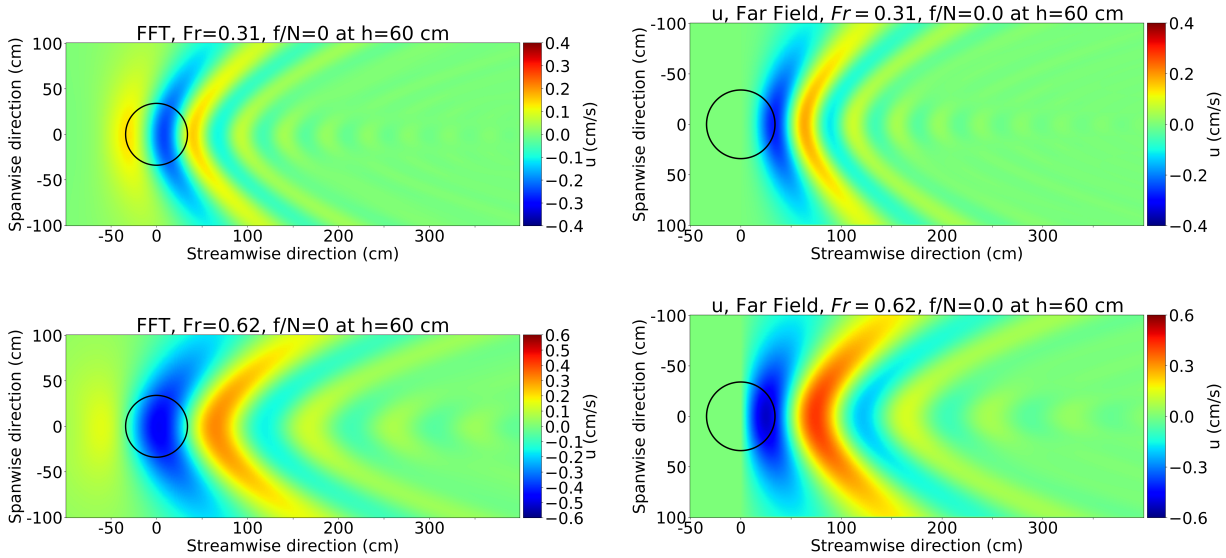

Figure 3.6: Horizontal cross-section at $z = 60$ cm above the bottom of the streamwise velocity field. On the left side the field computed using the FFT and on the right side the field analytically computed in the Far Field Approximation. At the top $Fr = 0.31$ and at the second line $Fr = 0.62$.

approximation, the waves keep a radially constant amplitude. The far-field approximation plots show a wave structure that seems to be consistent with a wave beam produced by a spherical source of waves, along a cone with its vertex in the center of the topographic obstacle. On the other hand, the field computed numerically shows a non-symmetric wave beam

To have a vision of the 3D structure of the waves, a horizontal cut at $3h = 60$ cm above the domain bottom of the streamwise velocity component is computed and shown in figure 3.6. In these figures, we indicate the topographic position and its size with a black circumference. At $3h$ above the bottom, we observe a parabolic shaped wave pattern. As previously commented, we found a better agreement between the iFFT numerically computed and the far-field for $Fr = 0.31$ than the one for $Fr = 0.62$. Also, the $Fr = 0.62$

parabolic shape is narrower than the parabolic shape found for $Fr = 0.31$.

Also, we observe that the wave amplitude for $Fr = 0.62$ is the four times the wave amplitude for $Fr = 0.31$. This is expected from the boundary condition $w(x, y, z = 0) \sim U_0 h_{\text{eff}}$ with $h_{\text{eff}} = U_0/N$: as the velocity U_0 is doubled, the effective height of the topography is doubled as well, which accounts for the factor four between the wave amplitude found for $Fr = 0.31$ and the one found for $Fr = 0.62$. This can be also observed in figure 3.7, which is a plot done from a cut along the central axis of the streamwise component shown in figure 3.6.

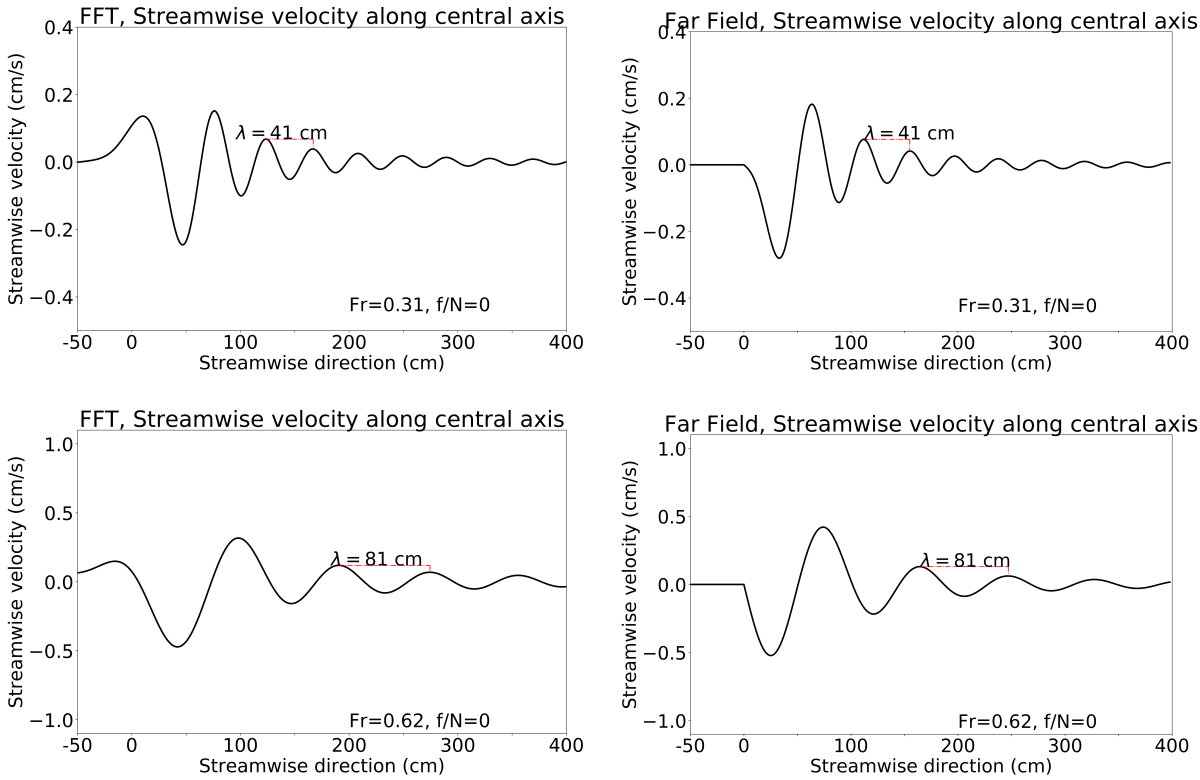

Figure 3.7: Horizontal cross-section of the streamwise velocity field at $3h = 60$ cm above the bottom. In the left column the field computed with the FFT and on the right the analytically computed field in the Far Field Approximation. At the top $Fr = 0.31$ and at the second line $Fr = 0.62$.

In figure 3.7 the wavelength is measured for the streamwise component of the velocity field at $3h$ above the ground. The wavelength found from the iFFT numerically and the one from the analytically computed fields for $Fr = 0.31$ is $\lambda_{0.31} = 41$ cm. For $Fr = 0.62$, the wavelength found from the iFFT numerically and analytically computed fields are as well in excellent agreement, having both a measured wavelength value of $\lambda_{0.62} = 81$ cm. The analytical theory indeed predicts that it is proportional to U_0 as discussed above.

3.3.2 Rotating case

In this subsection, we analyze the iFFT numerically computed velocity fields under the influence of rotation. These velocity fields are compared with the velocity fields in the non-

rotating system to have a better understanding of the influence of rotation in the IGW's field. To have a general view of the wave field, a vertical cut along the streamwise direction of the streamwise velocity for a rotating and non-rotation system are displayed in figure 3.8.

Alike in the non-rotating system, the DSL hypothesis has been taken into account for all the rotating configurations. This means that, for the computation, we did not take into account the region for which the height is below h_s. So it has been masked in the figures, shown as a white region.

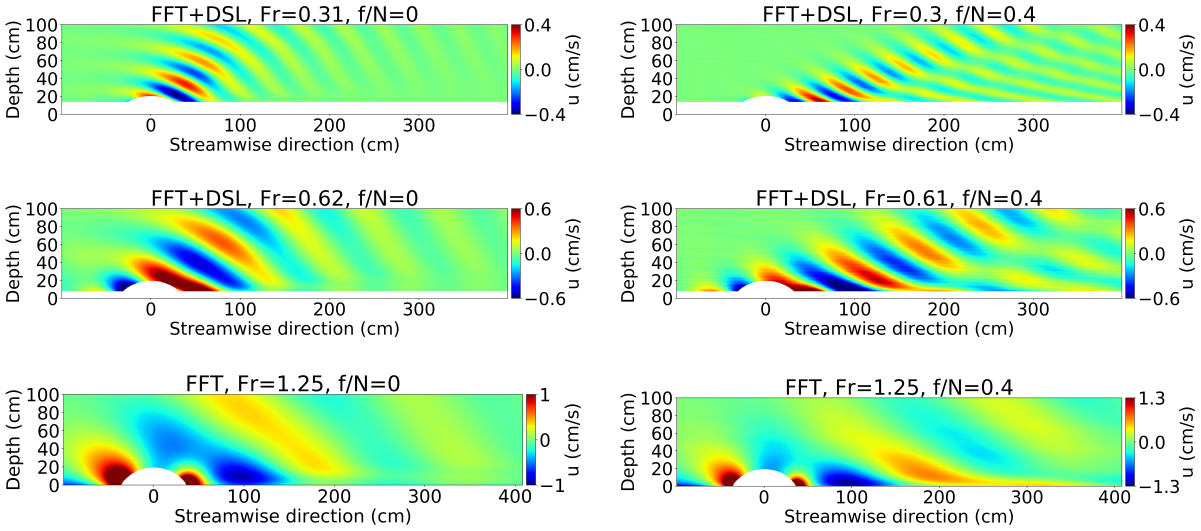

Figure 3.8: Vertical cross-section along the central-streamwise axis of the streamwise velocity field. Linear theory results without rotation are shown in the left column, and linear theory results with rotation are shown on the right. At the top $Fr = 0.31$, in the second row $Fr = 0.62$, and at the bottom $Fr = 1.25$.

In the left column of figure 3.8 are the velocity fields without the influence of rotation for $Fr = 0.31$, $Fr = 0.62$ and $Fr = 1.25$; in the first, second and third row, respectively. The right column shows the respective velocity fields for a system under the influence of rotation with $f/N = 0.4$. While there is a single beam in the non rotating cases, there are several wave beams for the rotating cases with all of their propagation vectors making a bigger angle with the vertical axis than the one obtained for the non rotating cases. This means that rotation tends to make the waves propagate more horizontally, in terms of the group velocity.

A set of horizontal cross-sections at $3h = 60$ cm above the bottom is shown in figure 3.9 in order to have an idea of the 3D structure of the wave field. Results for non-rotating cases are shown on the left, and for rotating cases, on the right. Due to the action of the Coriolis force, these cross-sections show an asymmetry in the shape of the waves in the rotating case.

In the same way as in figure 3.8, figure 3.9 shows a smaller wave amplitude for the rotating cases than the wave amplitude found for the non-rotating configurations. A displacement of the first maximum is observed with respect to the center of the topography. This might be a direct consequence of the increase of the angle that makes the propagation group velocity

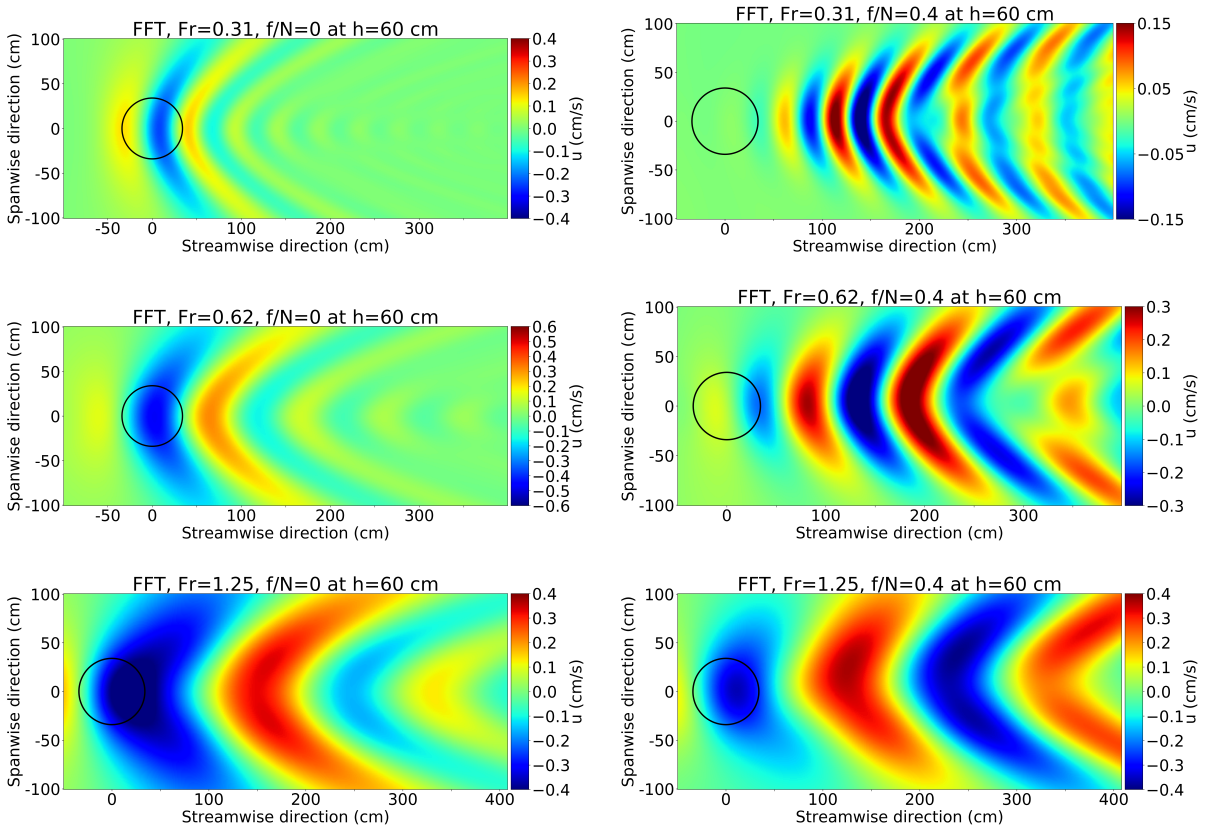

Figure 3.9: Horizontal cross-section of the streamwise velocity field at $z = 60$ cm above the bottom. The position of the topography at the bottom of the domain is indicated with a black circle. Linear theory results without rotation displayed on the left and the ones with rotation are displayed on the right. At the top $Fr = 0.31$ and at the second line $Fr = 0.62$.

vector with the vertical. No additional information is shown in the horizontal cut of the vertical velocity field, so this cut is not included here.

Figure 3.8 provides a global picture of the wave structure but does not give a quantitative approach to the wavelength changes because of the rotation. To explore the impact of rotation in the wavelength, figure 3.10 is constructed. Although this figure shows an oscillatory phenomenon, it is not possible to identify, at first sight, a single wavelength. In this case, we follow the same procedure as before by taking as wavelength the distance between the first two maximums after the steepest minimum. The wavelengths obtained with linear theory differ from those obtained with PIV by a 39% for $Fr = 0.31$ and by a 110% for $Fr = 0.62$. This figure shows that the PIV experimentally obtained waves have shorter wavelengths and weaker amplitude than the ones obtained from Linear Theory+DSL.

On the other hand, by comparing the LT+DSL waves from figure 3.10 with the respective LT+DSL waves from figure 3.7, we find shorter wavelengths for the non-rotating cases than for the rotating ones. From this comparison, we also observe that the wave amplitudes for the rotating cases are as large as for the non-rotating ones.

Although an asymptotic approximation for the far field is missing, [Redekopp, 1975] has predicted the global structure of the wave pattern by ray tracing theory, following a general

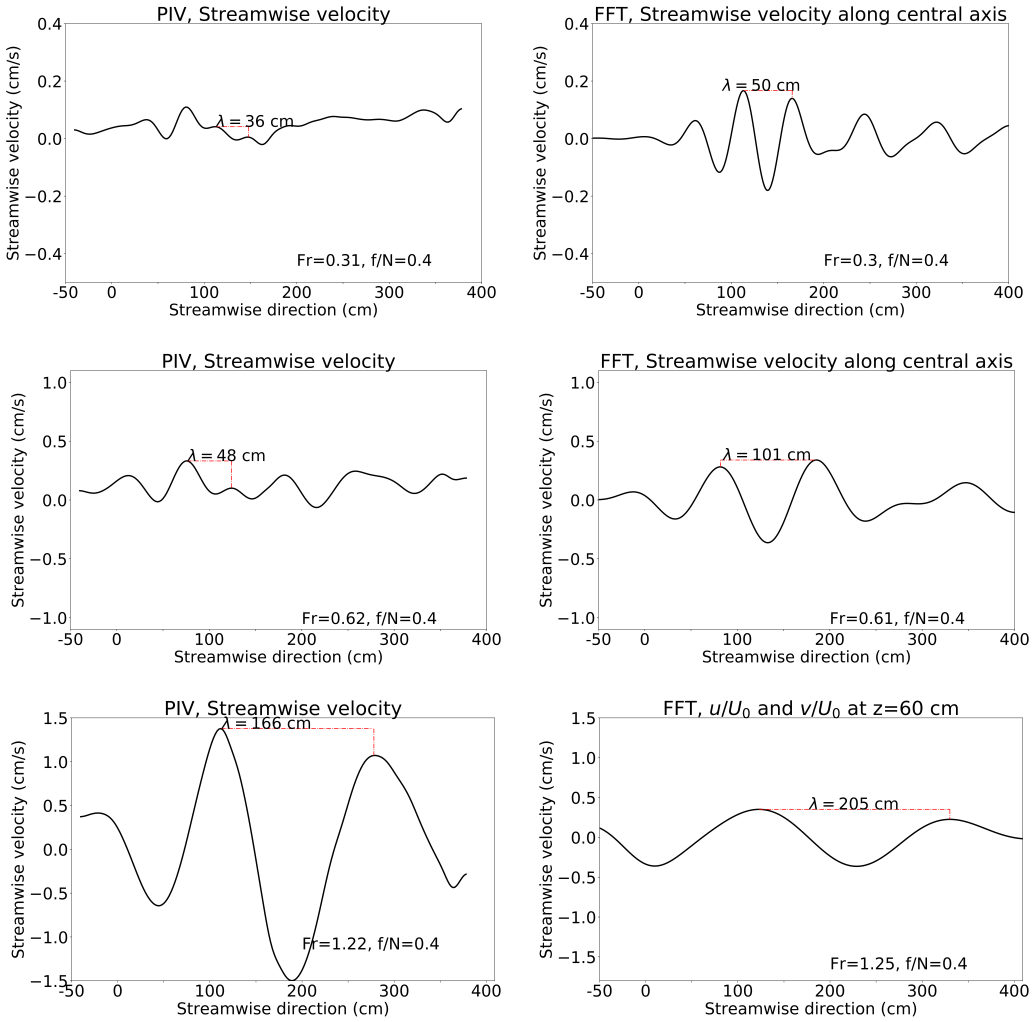

Figure 3.10: Stream-wise velocity along the central-streamwise axis with $f/N = 0.4$ along the topography axis at $z = 60$ cm (3 topography heights) from the bottom. In the first row the results for $Fr = 0.31$ are shown and in the second one the results for $Fr = 0.62$. The PIV experimental measurements done by [Sommeria et al., 2016] for 3D numerical simulation are shown in the left column. Linear theory results considering the DSL hypothesis are shown in the right column.

approach proposed by Lighthill. The source is emitting waves within a spectrum of wave vectors, each of them propagating with its own group velocity along a straight ray path. Each of these wave vectors satisfies the condition of stationarity $k_x U = \omega(\vec{k})$. In the absence of rotation, this approach yields iso-phase surfaces which cut the axial vertical plane along circles centered on the source. This fits well with the far field results shown in figure 3.11. In a horizontal plane at a given height, the iso-lines are hyperbolas. In the presence of Coriolis effects, [Redekopp, 1975] has shown that rays can be emitted only in a range of tilt angles with respect to the horizontal, with an upper bound decreasing with increasing ratio f/N. This maximum angle is indicated in figure 3.11 in our case $f/N = 0.4$. Below this boundary line, two dominant wave vectors locally dominate, with theoretical phase isolines from [Redekopp, 1975] also indicated in figure 3.11.

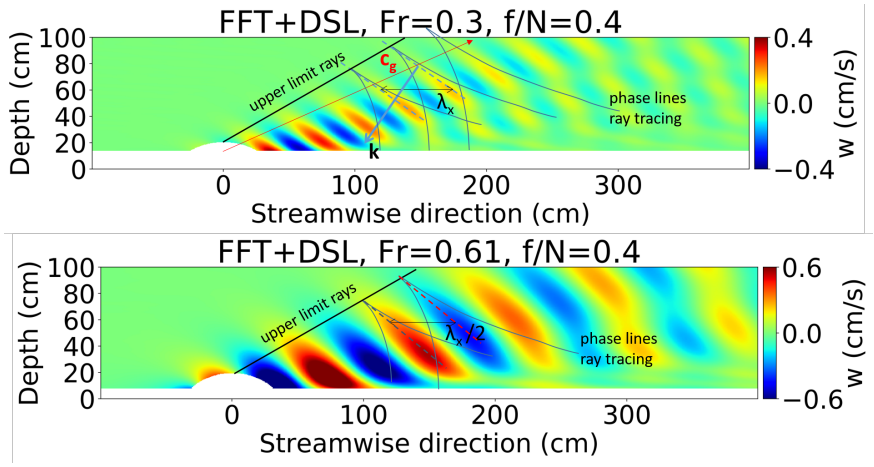

Figure 3.11: Ray analysis using method of [Redekopp, 1975] in the vertical plane cut of the vertical velocity field computed along the central-streamwise axis. At the top $U_0 =$ 3 cm/s and at the second line $U_0 = 6$ cm/s.

The wave field from the numerical integration seems indeed to be the result of the superposition of two wave patterns described by these isolines. Close to the theoretical upper boundary of the wave train, a dominant wave vector is clearly visible. The wave crests can be followed, from which a wave vector perpendicular to the crests can be drawn, as shown in figure 3.2. From that it is possible to determine the dominant wavelength λ_x and the associated wavenumber $k_x = 2\pi/\lambda_x$ as sketched in the figure. The wave vector angle θ with respect to the vertical is thus determined also. The dispersion relation $k_x U_0 = \omega = N[\sin^2\theta + f^2/N^2\cos^2\theta]^{1/2}$ can thus be checked. For $Fr = 0.31$, the numerical results are $\lambda_x = 55$ cm and $\theta = 35^o$, from which $\left|\vec{k}\right| = 0.2\text{cm}^{-1}$. This yields $k_x U_0 = 0.34$ s^{-1} while $\omega = 0.32$ s^{-1}, so the agreement is reasonable. For $Fr = 0.62$, we get similarly $\lambda_x = 102$ cm, $\theta = 39^o$,from which $\omega = 0.39\,\text{s}^{-1}$ while $k_x U_0 = 0.37$ s^{-1}, so the agreement is also reasonable.

The intrinsic group velocity $\vec{c}_g$ in the vertical plane can be calculated from these data by the formula

$$\vec{c}_g = \nabla_k \omega = \frac{N^2}{|\vec{k}|\omega}\left(1 - \frac{f}{N^2}\right)^2 \sin\theta\,\cos\theta \begin{cases} \cos\theta \\ -\sin\theta \end{cases} \tag{3.23}$$

In the absence of rotation, the far field iso-phases in the vertical plane are circular, with $|\vec{k}| = N/U_0$. Then the intrinsic group velocity reduces to $\vec{c}_g = U_0\cos\theta\,(\cos\theta, -\sin\theta)$ and, including advection, the total group velocity is $-U_0\sin\theta\,(\sin\theta, \cos\theta)$. It is therefore aligned with the wave vector (perpendicular to the iso-phase lines) at each angular position. The situation is more complex in the rotating case. For $Fr = 0.31$, the previously obtained numerical values for the selected wave vector yields $\vec{c}_g = (-1.17,\ 0.815)$ cm/s, and by adding the advection by the flow $U_0 = 3$cm/s, this yields a total group velocity (1.83,0.815) cm/s. The direction of this vector is shown in figure 3.11 and it corresponds indeed to the direction of propagation of the dominant wave.

3.4 Conclusions

In this chapter, an analysis of the internal gravity waves (IGW) field is presented in the context of the linear theory. We recall that the studied system is the one described in chapter 2. This system is a density stratified fluid with buoyancy frequency, N. The fluid flows at a constant flow rate, U_0, over an isolated spherical cap of height h. As linear theory applies for $Fr < 1$, where $Fr = \frac{U_0}{Nh}$ is the Froude number; two of the three flow rates were considered in this chapter. These are the ones corresponding to the Froude values $Fr = 0.31$ and $Fr = 0.62$. The deviations of the velocity fields were obtained for a rotating and a non-rotating system.

As an improvement to the linear theory, we introduce the dividing streamline (DSL) hypothesis. We recall that if the Froude number Fr is smaller than 1, the flow has not enough kinetic energy to rise over the topography of height h thus, there is a portion of fluid flowing around the topography with quasi-horizontal motion and a portion flowing above it, exciting a lee wave. These two sections are separated by a dividing streamline at a vertical level such that the remaining height $h_{\text{eff}} = hFr$ of the cap above corresponds to the topographic height involved in the waves emission. We take into account the DSL, by considering that our topography, the spherical cap, protrudes from the ground only the effective height h_{eff}. We evaluated the impact of the DSL through comparisons with PIV experimental measurements done by [Sommeria et al., 2016].

The study of the system is divided into four parts. Firstly, we compute the wave field from an analysis in Fourier space. The equations of movement are numerically inverted using the inverse fast Fourier transform (iFFT). We do this analysis for the system without rotation considering 1) only the linear theory, and we compare it with 2) the results of the linear theory considering the DSL hypothesis. By comparing 1 and 2 with the experimental results, we conclude that the DSL hypothesis represents a considerable improvement to the model. Although 1 predicts the wavelength correctly, it overestimates the amplitude of the waves. On the other hand, 2 provides a good estimate for both. For this reason, we decided to study the system by including the DSL hypothesis in the linear theory. 3) The study of the non-rotating system is complemented by a comparison with Bruno Voisin's results in the far-field approximation. Voisin, using linear theory and including the DSL hypothesis, found an algebraic solution in the far-field approximation for the non-rotating system. We found a good agreement between the results of 2 and 3 with the experimental results, for distances of the order of 10 times $\frac{U_0}{N}$. Finally, 4) we do the numerical analysis using linear theory, which includes the DSL for the rotating system. We find a good agreement between 4 and the corresponding experimental results.

We considered the topography as a source of waves that emits waves with the spectrum of this topography. Since we considered a spherical cap topography which has a continuous Fourier spectrum, we expect to observe a spectrum of wavelengths that satisfy the dispersion relation. However, we observed a preferred wavelength for the two Froude numbers in the

rotating and non-rotating systems.

For the non-rotating case, the value of this wavelength is set by the value: U_0/N, which is the effective height of the topography. Thus, we can conclude that the wavelength is set by the topographic size as for a sinusoidal topography. For each Froude number, these preferred wavelengths agree well with the experimentally obtained. In the case with rotation, the linear theory wavelengths agree with the experimental ones but not as well as in the non-rotational case. This might be because it was difficult to select properly the maximums and minimums from the experimental results.

The introduction of the dividing streamline hypothesis involves a significant correction to the amplitude of the waves. It can be explained in terms of the boundary condition. The amplitude of the waves is set through the boundary condition in the topography for the vertical component of the velocity $w \sim U_0 h_{\text{eff}}$. From this, we can conclude that not including the dividing streamline hypothesis in linear theory implies an overestimation of the wave amplitude by a factor of $1/Fr$.

When we make a horizontal cross-section of the wave field we observe that the waves have a parabolic shape, which becomes narrower as the Froude number increases. On the other hand, when we take the horizontal cross-section for the rotating system, the wave shape has no longer a parabolic shape, but a hyperbolic shape instead. This occurs because the rotation breaks the horizontal symmetry of the velocity. Due to the same cause, we observe that the $y-$component of the velocity is no longer zero in the rotating system whereas it is in the non-rotating one.

From the vertical cross-section of the velocity, we observe that the angle θ that the wave vector makes with the vertical increases as the Froude number increases. Now, if we consider the rotating case, we observe that θ increases as f/N increases, which agrees with the ray theory prediction. This means that the wave vector becomes more horizontal as either the mean flow or the rotation rate increase.

4

Experimental and numerical study of a flow past a spherical cap: non-rotating system

This chapter is a first draft of a paper in preparation.

4.1 Introduction

In this chapter the results of the three-dimensional numerical simulations and the PIV experimental measurements for the system described in chapter 2 are presented and analyzed, in the absence of rotation. Comparison with the linear theory is also discussed. We remind that we consider a constant flow $\vec{U_0} = (U_0, 0, 0)$ flowing over a cap. The flow is modified by the interaction with the cap leading to two different behaviors: an oscillating and a turbulent behavior. The oscillating part is composed of internal gravity waves (IGWs) propagating over the topography while the non-oscillating turbulent behavior consists of a wake forming behind the topography. The wave field is analysed in section 4.2 and the wake field analysis is presented in section 4.3. The results are discussed and summarized in section 4.4.

In the following, the *vertical center plane* refers to the vertical (x, z) plane containing the streamwise symmetry axis. We remind that the *streamwise velocity deviation* u' is the departure of the streamwise velocity u with respect to the constant flow U_0.

4.2 Analysis of the lee wave field

4.2.1 Overall flow behavior

Figure 4.1 presents a general view of the flow behavior, with the streamwise velocity deviation being displayed in the vertical center plane. This figure consists of three frames, each corresponding to a different value of the Froude number, equal to 0.31 ($U_0 = 3$ cm/s), 0.62 ($U_0 = 6$ cm/s) and 1.25 ($U_0 = 12$ cm/s) from top to bottom, respectively. Each of these three frames exhibits two different behaviors: in the upper part of the physical domain, only waves exist, while in the bottom part, a deficit in the streamwise velocity deviation is observed due to a blocking effect of the flow by the spherical cap. This blocking effect, observed for instance in wind farms [Clary et al., 2018], leads to the formation of a wake behind the object, as will be further discussed in section 4.3.

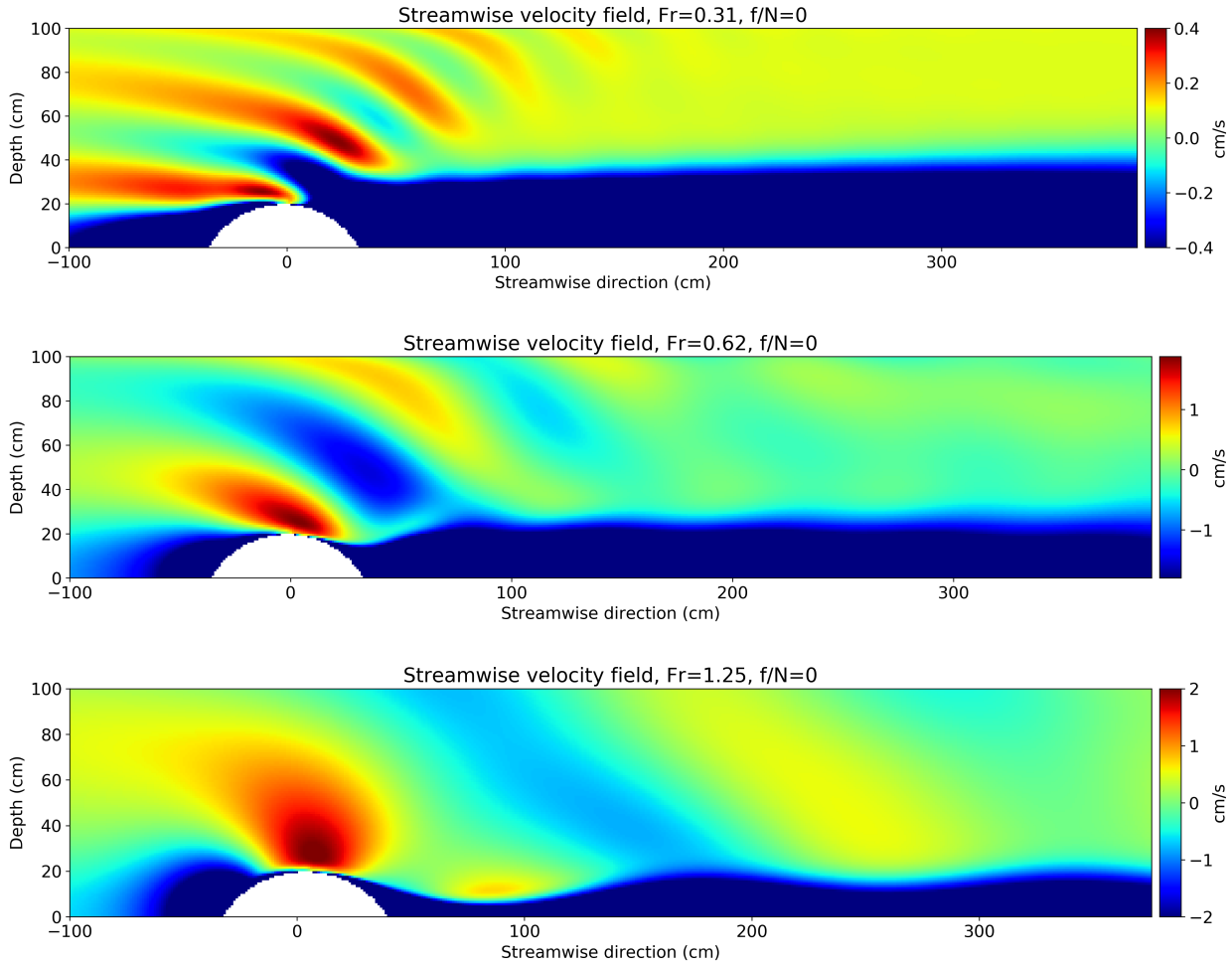

Figure 4.1: Cross-section of the streamwise velocity deviation in the vertical center plane for each of the Froude numbers we consider. In the first row, it is displayed for $Fr = 0.31$, in the middle one for $Fr = 0.62$ and in the bottom row for $Fr = 1.25$. This figure focuses on the wave field thus, the color scale is chosen accordingly. Indeed, the range of values for each frame is (in cm/s): For $Fr = 0.31$, $u' \in [-3.8, 0.4]$; for $Fr = 0.62$, $u' \in [-6.9, 1.9]$; for $Fr = 1.25$, $u' \in [-12, 2]$.

4.2.2 Structure of the three-dimensional wave field

4.2.2.1 Vertical structure of the wave field

A cross-section of the vertical velocity field in the vertical center plane is displayed in figure 4.2 for the three values of the Froude number we consider. For $Fr < 1$, the very bottom of the physical domain does not show any waves below the height of the dividing streamline (which is a plane here) that divides the flow into the wave and no-wave flow zones. We recall that the height of the dividing streamline (from the bottom plane) is given by $h_s = (1 - Fr)h$, where h is the height of the cap, so that $h_s = 13.8$ cm for $Fr = 0.31$ and $h_s = 7.6$ cm for $Fr = 0.62$. These heights are indicated with a horizontal red line in figure 4.2. Hence, waves are emitted only above the dividing streamline, in agreement with the theoretical prediction of [Voisin, 2007].

As predicted theoretically by [Long, 1955] (see also [Wurtele, 1957]), the phase lines of lee waves emitted by an obstacle have a circular form in the vertical plane in the far field approximation. This is indeed what is observed in figure 4.2 for $Fr = 0.31$ and $Fr = 0.62$ (top and middle frames, respectively), above the wake and far enough from the topography downstream. The form of the phase lines changes however in the wake, becoming more vertical for $Fr = 0.31$ and being even twisted in the opposite direction for $Fr = 0.62$. As shown in figure 4.9, the wake is associated with a recirculation zone behind the topography, which therefore induces a vertical shear (with positive vorticity along the $y-$ axis). This shear refracts the waves, which may account for the change of the form of the phase lines.

The amplitude of the velocity components u' and w vary along the circular phase lines and appear to have a non-zero value in a localized region whose tangent to the phase line makes a given angle. In other words, there is a preferred wave vector whose direction is indicated with a black line in figure 4.2. This is quite remarkable because the cap can be considered as a continuous wave source $q(\vec{k})$ which emits waves with three-dimensional wave vectors controlled by the Fourier spectrum of the shape of the cap. Yet, figure 4.2 shows that a preferred wave vector exists whatever the value of the Froude number. Therefore, this wavelength does not depend upon the shape of the topography. (We recall that, by contrast, for a sinusoidal topography, the horizontal wavelength of the waves is imposed by that of the topography, whatever the speed of the uniform flow.) It is straightforward to show that this wavelength is proportional to U_0/N, as done by [Long, 1955]. Indeed, in a frame of reference attached to the current, the wave frequency is equal to $-k_x U_0$ and satisfies the dispersion relation $N\, k_x/|\vec{k}|$ (considering a vertical plane for simplicity). This yields $|\vec{k}| = N/U_0$.

The values of the vertical velocity field in figure 4.2 range between the minimum and maximum values of that field (which are not quite symmetric about zero because of the action of the viscosity on the propagating wave field). These values are about four times larger for $Fr = 0.62$ than for $Fr = 0.31$ which can be qualitatively explained. Indeed, the amplitude of w is set by the boundary condition at the surface where the waves are emitted.

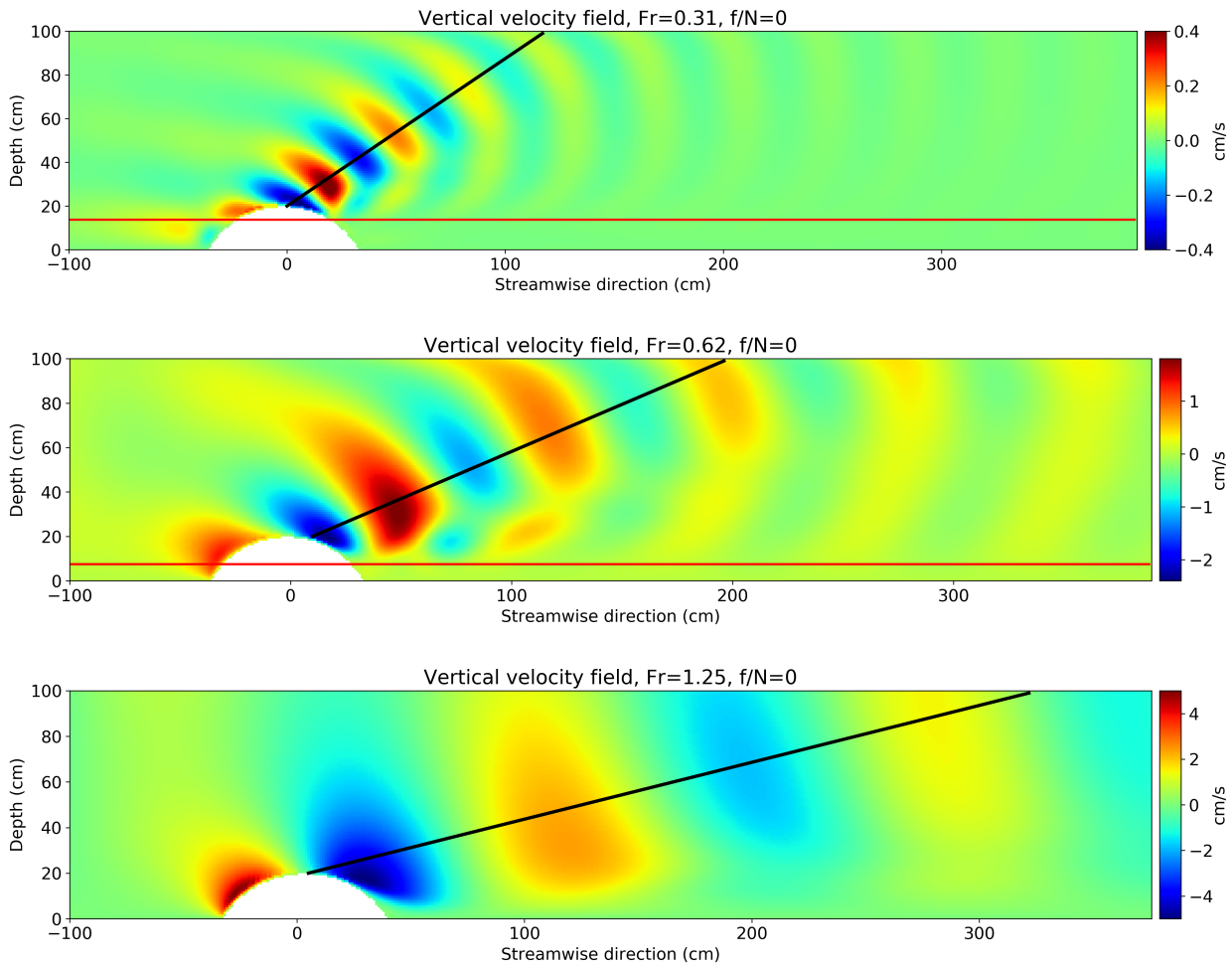

Figure 4.2: Cross-section of the vertical velocity field in the vertical center plane for a) $Fr = 0.31$, b) $Fr = 0.62$ and c) $Fr = 1.25$. The height of the dividing streamline is drawn with a red line in the frames with $Fr < 1$ (for $Fr > 1$, there is no dividing streamline). The black line is normal to phase lines and indicates that there is a preferred wave vector. The angle that this wave vector make with the vertical, denoted θ in the text, is indicated in the first frame.

Taking the dividing streamline for this surface, w is proportional to $U_0(h-h_s)$, where $h-h_s$ is the height of the fluid layer passing over the cap. As noted above, $h-h_s$ is twice larger for $Fr = 0.62$ than for $Fr = 0.31$, and so is also U_0, which accounts for the factor of 4.

The figure also shows that the wavelength of the preferred wave vector increases with U_0, consistent with the prediction by [Long, 1955] that this wavelength is proportional to U_0/N. This behavior can also be accounted for qualitatively by noting that, in the frame of reference attached to the moving fluid, the wave frequency $\omega = -k_x U_0$ should be smaller than N. The range of radiated horizontal wavelengths therefore satisfies

$$\lambda_x > 2\pi U_0/N. \tag{4.1}$$

It follows that, as U_0 increases, so should also do the horizontal wavelength of the preferred wave vector. Relation (4.1) can be verified from the angle θ that the preferred wave vector

makes with the vertical. Indeed, since the wave frequency satisfies the dispersion relation, one has:

$$U_0^2 k_x^2 = N^2 \sin^2 \theta. \tag{4.2}$$

Relation (4.2) implies that λ_x can be inferred from an estimate of θ using figure 4.2. Table 4.1 displays the values of θ estimated from that figure and λ_x using (4.2) and the lower bound $2\pi U_0/N$ is also indicated. The last two columns of the table show that relation (4.1) is indeed satisfied.

For $Fr = 0.31$, table 4.1 also shows that the angle of the beam with the vertical is about 56° and increases with the Froude number (being equal to 67° and 76° for Fr=0.62 and Fr=1.25, respectively). The same result was observed by [Dalziel et al., 2011] in a series of laboratory experiments of lee wave generation by a half-sphere obstacle with Fr ranging from 0.1 to 0.3. For $Fr = 0.3$, the same value is found for θ in these experiments, and θ increases from 44° to 56° as Fr increases from 0.1 to 0.3. We can also notice that for these low values of the Froude number, the corresponding ratio of ω/N is equal to about 0.8. This is actually a quite general result for linear internal gravity waves generated by a moving source, whatever the motion of this source, oscillating or turbulent (f.i. [Largeron et al., 2013]). An argument proposed in section 4.2.6 will help clarifying this finding.

U_0 (cm/s)	Fr	θ (rad)	$k_x = N \sin\theta / U_0$ (1/cm)	$\lambda_x = 2\pi/k_x$ (cm)	$2\pi\, U_0/N$ (cm)
3	0.31	0.99	0.1337	46	39.3
6	0.62	1.17	0.0736	85	78.5
12	1.25	1.33	0.0388	161	157

Table 4.1: Horizontal wavelength and angle with respect to the vertical of the propagating lee wave.

4.2.2.2 Horizontal structure of the wave field

To have a better view of the three-dimensional wave structure, a horizontal cross-section at 60 cm above the bottom of the domain of the streamwise velocity deviation is shown in figure 4.3. For each of the three flow rates the wave field displays a hyperbolic form which is symmetric with respect to the central-streamwise axis. This form, which is hardly visible for $Fr = 0.31$, closes as the flow rate increases and is consistent with the analytical finding of [Wurtele, 1957] for linear waves. The dependence of this form as a function of the Froude number has been studied analytically in [Sharman and Wurtele, 1983] for the case of a rigid lid (with wave modes along the vertical) and for an exponentially decaying wind. The near-field solution with viscosity has been computed for the case of a sphere by [Voisin, 2007], for a uniform flow speed and constant stratification.

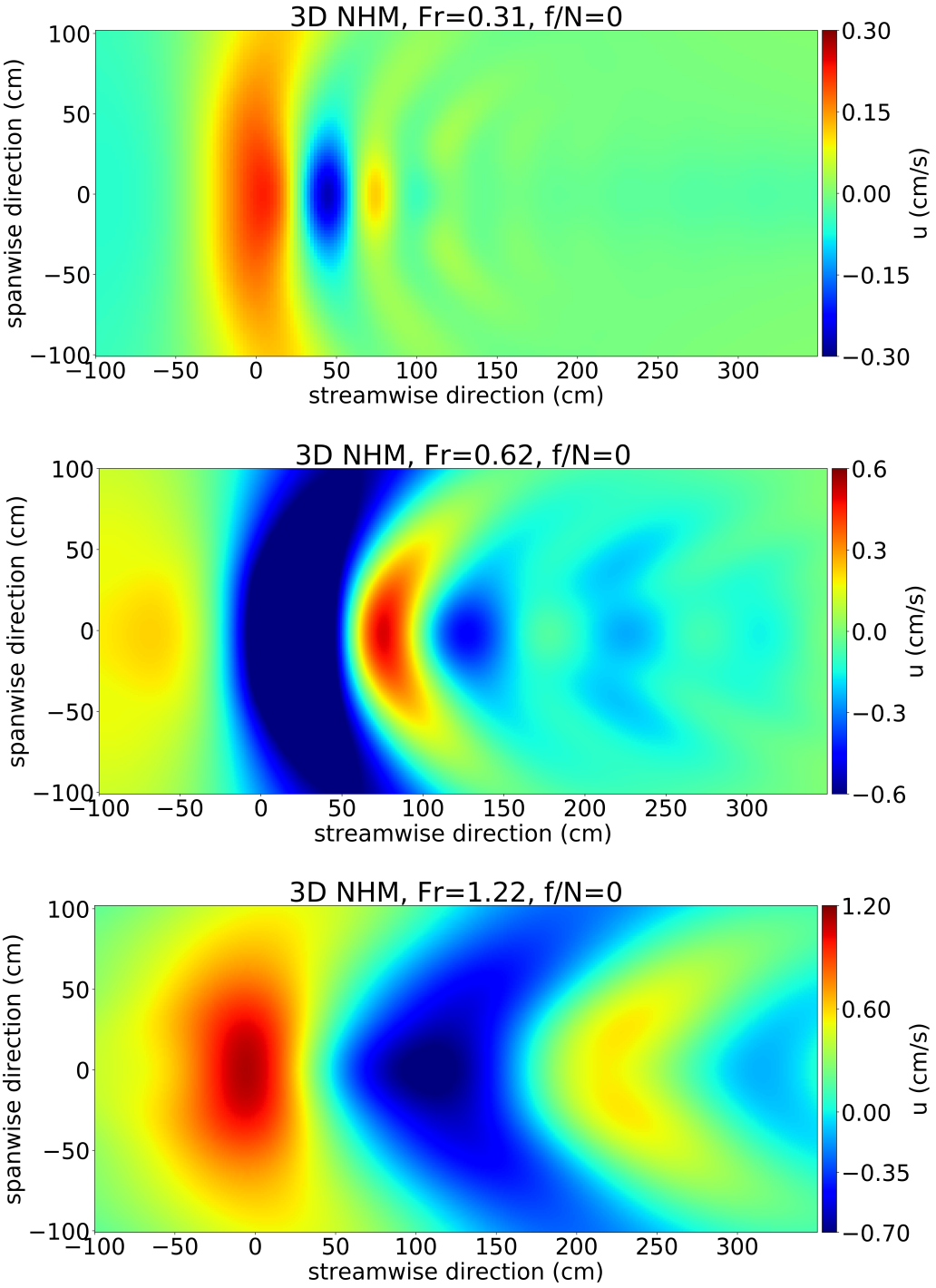

Figure 4.3: Horizontal cross-section at 60 cm above the bottom of the streamwise velocity deviation for $Fr = 0.31$ in the first row, $Fr = 0.62$ in the second row and $Fr = 1.25$ in the third row. Each field is averaged once the steady regime is reached, namely over $[40, 60]$ buoyancy periods for $Fr = 0.31$, over $[30, 50]$ buoyancy periods for $Fr = 0.62$ and over $[20, 47]$ buoyancy periods for $Fr = 1.25$.

4.2.3 About simulations in a vertical plane

It is not easy to estimate the impact of the wake on the radiated wave field by the cap. Indeed, the wake does not exist if the simulation is performed in a vertical plane but, in the latter case, the shape of the cap changes from spheroidal to cylindrical, implying that the structure of the radiated wave field should be different. However, in the theoretical modelling considered by Voisin ([Voisin, 2007]), the phase lines for the cylinder are the same as for the sphere in the vertical central plane (Voisin, private communication).

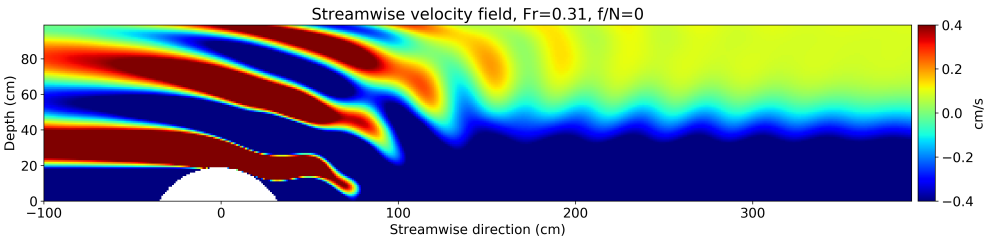

Figure 4.4: Two-dimensional simulation in a vertical plane. The streamwise velocity deviation is displayed for $Fr = 0.31$, the actual minimum and maximum values being -5 and 4.

The same problem has therefore been simulated in a vertical plane for the three flow rates we consider and only the case of the lowest flow rate is displayed in figure 4.4. Three striking (and well-known) points should be noted from these computations. First, the propagating part of the flow field also displays a specific wavelength, which increases with the flow rate (not shown) and is comparable to its three-dimensional counterpart. The second point is that the amplitude of the two-dimensional wave field is about ten times larger than that of the three-dimensional field. This can be accounted qualitatively from the conservation of energy: the energy flux is confined to a plane in the two dimensional configuration while it spreads in three dimensions, implying that the local wave-induced amplitude is larger in the former case than in the latter (in the far-field limit, the energy decays as $1/\sqrt{r}$ in two dimensions and as $1/r$ in three dimensions). This expected behavior was also noticed by [Nikurashin et al., 2014]. The third point is that the phase lines extend very far upstream, due to the blocking of the flow by the topography.

4.2.4 Comparison with the field experiments

4.2.4.1 Vertical structure of the wave field

As discussed in section 2.2, the PIV method is applied in horizontal planes, allowing to compute the horizontal velocity components. To access the vertical structure of the flow, which is controlled by the wave field above the cap, data acquisition was done by scanning the flow vertically at ten different levels. Since the wave field is best represented by the vertical velocity component and the flow is incompressible, the horizontal divergence $\nabla_H.\vec{u}$,

equal to $-\partial w/\partial z$, was used as a proxi for the wave field. This horizontal divergence was also computed in the numerical simulations.

The field $\nabla_H.\vec{u}$ is displayed in figure 4.5 as a function of the azimuth in the laboratory measurements (left column) and as a function of the streamwise coordinate in the numerical simulation (right column), for different positions along the vertical direction ranging from 25 to 45 cm and separated by 4 cm. Each curve is shifted along the vertical by an arbitrary value of 0.05 so as to have a visual representation of the wave field.

For $Fr = 0.31$, a propagating wave system above the cap is visible, whose phase lines are marked with inclined solid lines. An estimate of the vertical wavelength can be estimated from this propagating wave system, equal to about 64 cm. A few similarities and differences can be noted when comparing with the results from the numerical simulations (right column). The wave amplitude close to the generation region of the waves is similar to that observed from the laboratory experiments; however this amplitude weakens very quickly with streamwise distance from the generation region in the simulation, being very likely damped by viscous effects.

For $Fr = 0.62$, the same observations can be done for the propagating wave system, already from 25 cm for the experiments but from 45 cm or so for the simulations. A trapped wave system seems to be observed in the simulations (see the vertically-aligned maxima at the streamwise distance of about 240 cm) but not convincingly so in the experiments.

Overall, it can be concluded that a good agreement is observed between the PIV experiments and the numerical simulations when the general structure of the propagating wave field is considered.

4.2.4.2 Comparison of the preferred wavelength between the PIV experiments, numerical simulations and linear theory

In order to measure the horizontal wavelength of the preferred wave vector, the streamwise velocity deviation is displayed in figure 4.6 in the vertical center plane at 60 cm above the bottom, so as to avoid the influence of the wake, for the laboratory experiments, the three-dimensional numerical simulations and the linear theory (with dividing streamline) presented in chapter 3, for the three flow rates we consider.

All curves displayed in figure 4.6 exhibit a set of oscillations after, in most cases, a pronounced minimum after the cap. The wavelength inferred from these oscillations, and measured after this pronounced minimum, is reported in table 4.2.

U_0 (cm/s)	Fr	PIV (cm)	3D NHM (cm)	Linear theory+DSL (cm)
3	0.31	50	41	44
6	0.62	78	94	81
12	1.25	162	179	164

Table 4.2: Horizontal wavelength of the lee wave field produced in a non-rotating system.

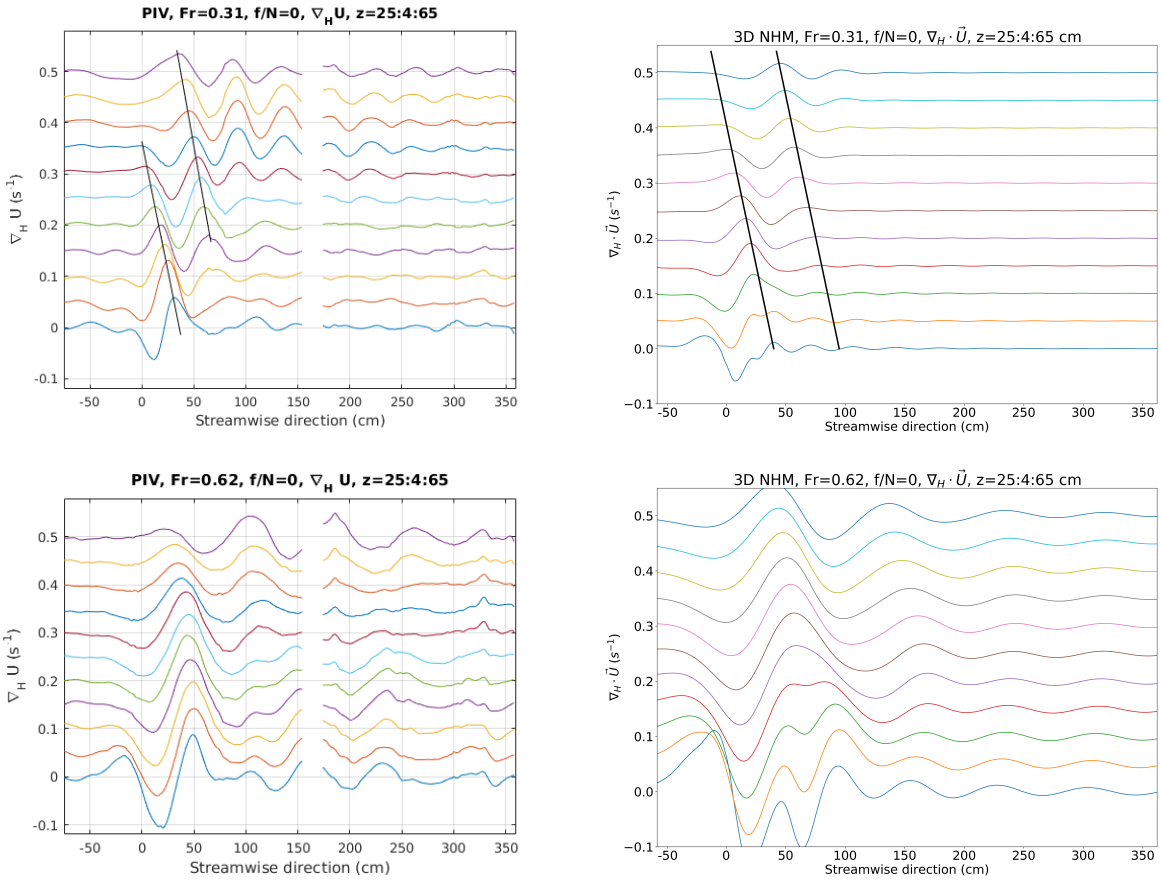

Figure 4.5: Horizontal divergence ($\nabla_H \cdot \vec{u} = -\frac{\partial w}{\partial z}$) as a function of the azimuth in the laboratory measurements (left column) and as a function of the streamwise direction in the numerical simulation (right column), for different positions along the vertical direction, ranging from 25 to 45 cm and separated by 4 cm. Each curve is shifted along the vertical by an arbitrary value of 0.05 so as to have a visual representation of the wave field. Upper row: $Fr = 0.31$, lower row: $Fr = 0.62$. Results are displayed after 120 buoyancy periods.

The key points to note are that, for a given value of the Froude number, all wavelengths satisfy inequality (4.1) and agree well with each other. Taking the value measured in the experiment as a reference value, relative differences are of 12% with the linear theory and of 18% with the three-dimensional simulation for Fr=0.31. For Fr=0.62, these relative differences are of 4% with linear theory (which is somewhat unexpected) and 21% with the three-dimensional simulation. Finally, for $Fr > 1$, the relative differences are of 1% with linear theory and of 7% with the three-dimensional simulation.

Now, if we compare the wavelengths estimated from the angle θ of the preferred wave vector, reported in table 4.1, with those estimated from figure 4.6, a relative difference of about 10% is found. The former values agree better with those found in the experiments for all Froude numbers (the relative differences being of 8%, 9% and 1% for Fr = 0.31, 0.62 and 1.25, respectively), implying that the method used to estimate the wavelength from the direction of the phase propagation in figure 4.2 appears to be better than the one used from figure 4.6.

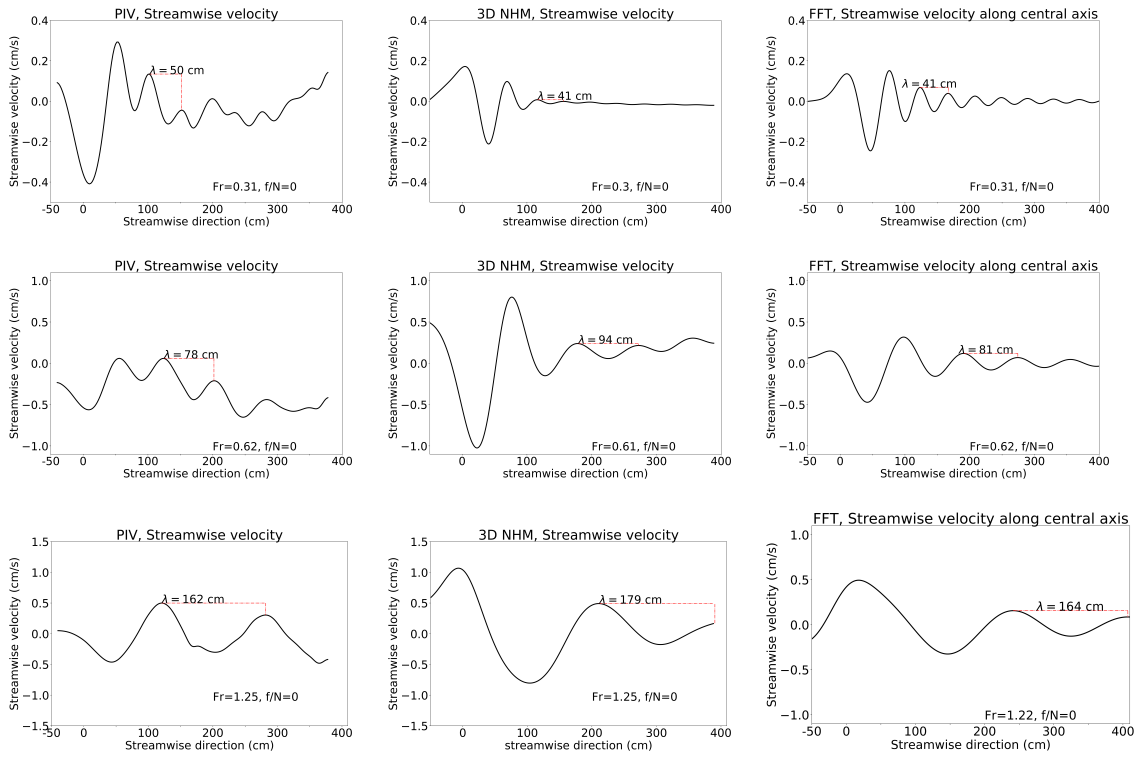

Figure 4.6: Horizontal wavelength measured at 60 cm above the bottom from three different approaches: PIV experiments in the first column, three-dimensional numerical simulations in the middle column and linear model with dividing streamline in the last column. Top row: $Fr = 0.31$, middle row: $Fr = 0.62$, bottom row: $Fr = 1.25$.

4.2.5 Momentum flux associated with the lee waves

Among the main objectives of the present PhD work stands the comparison of the momentum flux transported away by the propagating waves and that transferred to the wake. The

momentum flux transported by the waves is computed in the present section as a function of the Froude number. A complete momentum budget for the horizontal velocity component u involving the wake is presented in section 4.3.3.

In three dimensions, the expression of the wave-induced momentum flux across a horizontal surface is $< u'\vec{w}' >_{xy} = (< u'w' >_{xy}, < v'w' >_{xy})$, where $<>_{xy}$ refers to an integral over a horizontal surface. We recall that the waves are steady. The dimensions of this surface are $[-d, 3d]$ and $[-100\,\text{cm}, 100\,\text{cm}]$ along the $x-$ and $y-$directions, respectively, where d is the horizontal size of the cap at the bottom of the domain. The two components of this flux have been computed just above the cap, at $z = 23$ cm. The component $< v'w' >_{xy}$ is much smaller than $< u'w' >_{xy}$, due to the symmetry of v' in a horizontal plane, and only the latter flux is considered here. This integrated flux computed at a given time during the steady regime is reported in table 4.3 for the three flow rates we consider, for the linear model and the three-dimensional simulation. The fluxes are scaled by U_0^2 to allow for comparison between the three cases.

Table 4.3 shows that, for Fr=0.62, the value of $< u'w' >_{xy} /U_0^2$ is similar for the numerical and linear models. For $Fr = 0.31$ by contrast, this flux is 4 times smaller for the numerical model than for the linear model. Several arguments can be invoked to account for this discrepancy. Figure 4.6 shows that the amplitude of u' decays faster when predicted by the numerical model than by the linear theory, possibly because of the interaction with the wake. Also, as shown in figure 4.3, the extension of the domain along the $y-$direction accounts for a limited part of the wave field while the whole domain is considered in the linear model. Finally, the part of the cap over the dividing streamline is defined by 6 points only, owing to the vertical resolution of 1 cm. For $Fr = 1.25$, the linear model predicts a 33% smaller value than computed numerically. The limit of the validity domain of that model may be reached here as the flatness assumption of the slope of the topography is no longer valid, the maximum value of that slope being equal to 0.5.

Fr	LT+DSL (cm^2)	3DNHM at z=23 cm (cm^2)	3DNHM at z=40 cm (cm^2)
0.31	-103	-25	-10
0.62	-172	-185	-153
1.25	-72	-109	-94

Table 4.3: Wave-induced momentum flux $u'w'$ integrated horizontally over the surface $[-d, 3d]$ x $[-100\,\text{cm}, 100\,\text{cm}]$ along the $x-$ and $y-$directions, respectively and normalized by U_0^2, computed at 23 cm above the bottom by the linear model and the three-dimensional numerical model.

In table 4.3 we observe a significant decrease in the momentum transport in the numerical simulation. This phenomenon is due to two different reasons: the first is due to the numerical and physical viscosity that damps the waves, thus this decrease is more important for the shorter wavelengths. The second is due to the size of the integration surface, as the wave

propagates, the parabolic shape of the wave field becomes wider. So, if we consider a constant area of integration at different levels, as we move away from the topography, the less wave field we observe, producing an apparent decrease in the transport of the moment.

The interpretation of the momentum flux is usually done through the introduction of a drag coefficient. The momentum transported by the waves is indeed associated with a drag force at the surface, exerted by the topography on the fluid. This drag force is characterized by the drag coefficient $C'_{D_{wave}}$ defined by

$$< |u'w'| >_{xy} = C'_{D_{wave}} \frac{U_0^2}{2} S, \tag{4.3}$$

where S is the section of the obstacle facing the flow. In the present case, this section is that of the cap over the height of the dividing streamline. Its expression is

$$S = R^2 \left[\alpha/2 - (1 - \frac{h_{eff}}{R} \sin(\alpha/2)) \right], \tag{4.4}$$

with α defined by $\cos(\alpha/2) = 1 - h_{eff}/R$, where $h_{eff} = h - h_s$ (see chapter 3) and R is the diameter of the sphere of which the cap is the upper part. In the present case, $h = 20$ cm, $R = 40$ cm and $h_s = 13.8$, 7.6 and 0 cm for $Fr = 0.31$, 0.62 and 1.25, respectively (see figure 3.1).

Using the values found by the numerical model for $< |u'w'| >_{xy}$ (see table 4.3) and expression (4.4) for the section S, the values of $C'_{D_{wave}}$ are equal to 0.27, 0.75 and 0.22, for $Fr = 0.31$, 0.62 and 1.25, respectively. These values, which are reported in table 4.4, are comparable to the drag coefficient of a car, which is of order 0.25. The part of the cap over the dividing streamline (when present) therefore exerts a strong drag on the flow. We also notice that these values are similar for $Fr = 0.31$ and 1.25 but about 3 times higher for $Fr = 0.62$. The behavior of the drag coefficient as a function of the Froude number is discussed in section 4.3.3.

In order to compare the values of the drag coefficient with those for the wake, we also compute this coefficient by considering the whole surface of the cap facing the flow. This surface is obtained by setting $h_{eff} = h$ in expression (4.4). The numerical values of this coefficient, denoted $C_{D_{wave}}$, are reported in table 4.4.

Fr	$C'_{D_{\text{wave}}}$	$C_{D_{\text{wave}}}$
0.31	0.27	0.01
0.62	0.75	0.15
1.25	0.22	0.09

Table 4.4: Drag coefficient (defined by equation (4.3)) induced by the wave field. Two coefficients are computed, either with h_{eff} varying when Fr varies in equation (4.3) for S (coefficient $C'_{D_{\text{wave}}}$) or with $h_{eff} = h$ in that expression for all Fr (coefficient $C'_{D_{\text{wave}}}$).

[Greenslade, 2000] makes a study for a sphere in a stratified flow,

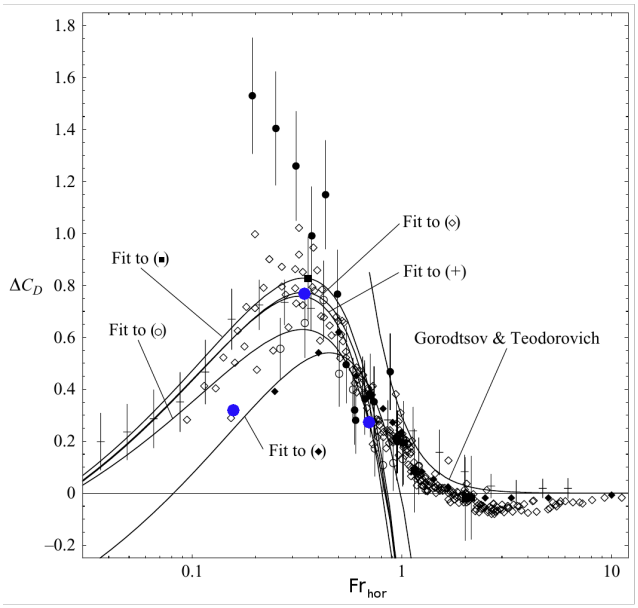

Figure 4.7: Comparison with bibliography of the total Drag coefficient computed from the numerical configuration. Image obtained from [Voisin, 2007], originally adapted from [Greenslade, 2000]. Laboratory measurements of C_D as function of the horizontal Froude number Fr_{hor}. The scatter bars are from [Mason, 1977], the white diamond symbols are from [Lofquist and Purtell, 1984], the black diamond symbols are from [Hanazaki, 1988], the black squares are from [Shishkina, 1996], the circles are from [Vosper et al., 1999]: the black ones for large hemisphere and the white ones for small hemisphere. The blue circles correspond to the wave drag coefficient here computed at $z = 23$ from the bottom.

In this chapter, the total drag coefficient $C_D = C_{D_{\text{waves}}} + C_{D_{\text{wake}}} + C_{D_\infty}$ is also calculated as a function of the horizontal Froude number ($Fr_{\text{hor}} = \frac{U_0}{Nr} = Fr\frac{h}{r} \approx \frac{Fr}{1.75}$). This coefficient depends in a non-trivial way on the Froude number reaching a maximum value for horizontal Froude numbers close to $Fr_{\text{hor}} = 1/3$ ($Fr = 0.62$) as seen in section 4.2.5. The drag coefficient obtained here for the wave field, drawn in blue, is in good agreement with the experimental results for a spherical cap.

Now, as the wave amplitude increases with the Froude number, we might expect that the drag coefficient associated with wave production should increase as Fr increases, but this is not the case. Although the amplitude of the internal waves is maximum in the case $Fr = 1.25$, the induced drag associated with their production is lower than the observed for $Fr = 0.62$. The wave-induced drag coefficient increases for $Fr < 1$ and then it seems to reach a maximum value for a Froude number, Fr, such that $Fr \lesssim 1$. In other words, taking into account the DSL hypothesis, this behavior in the drag force associated with the wave emission, seems to be linked to the fact that there is too much kinetic energy that might be used to produce waves; but, the effective surface of the sphere is not enough to produce them.

4.2.6 Computation of the energy flux

The energy flux associated with the energy transport by the waves is defined by $< p'w' >_{xy}$ where p' is the dynamical pressure and the brackets refer to a spatial integral over the horizontal plane defined in the previous section. We computed this flux at 23 cm above the bottom. This energy flux normalized by U_0^3 is displayed in table 4.5 for the three flow rates we consider. For a monochromatic wave, which is the case for lee waves, the energy and momentum fluxes normalized by U_0^3 and U_0^2, respectively, are equal in absolute value in the linear regime (since $< p'w' >_{xy} /\rho_0 = -U_0 < u'w' >_{xy}$). This is indeed what tables 4.3 and 4.5 show, except for Fr=0.62 where the normalized energy flux is 50% larger than the normalized momentum flux. The peculiar behavior for $Fr = 0.62$ is discussed in section 4.3.3 below.

Fr	$\frac{<p'w'>_{xy}}{U_0^3}$ (cm^2)
0.31	18
0.62	240
1.25	154

Table 4.5: Vertical energy flux $\langle p'w' \rangle_{xy}$ normalized by U_0^3 computed by the three-dimensional simulations for $Fr = 0.31$, $Fr = 0.62$ and $Fr = 1.25$, at 23 cm above the bottom. The flux is integrated horizontally over the surface $[-d, 3d]$ x $[-100\,\text{cm}, 100\,\text{cm}]$ along the $x-$ and $y-$directions, respectively.

We showed in section 4.2.4.1 that the lee wave field has a preferred wave vector. The modulus of this wave vector $|\vec{k}|$ is equal to N/U_0, as was shown easily, but the selection of its angle θ is less clear. It should therefore be understood why a horizontal wavelength $2\pi/k_x = 2\pi/(|\vec{k}|\sin(\theta))$ is selected. For this purpose, we computed the spectrum along the $x-$direction of the wave-induced energy flux, $\overline{\Re(\hat{p'}\hat{w^*})}$, where the $\hat{}$ and * symbols denote the Fourier transform and the complex conjugate, respectively, $\Re$ stands for the real part and the over-bar denotes an average along the $y-$direction. The spectrum is computed at $z = 23$ cm.

Figure 4.8 displays $\overline{\Re(\hat{p'}\hat{w^*})}$ as a function of the horizontal wavenumber k_x, using linear and logarithmic coordinates. The wave-induced energy flux peaks at a maximum value for a horizontal wavelength equal to 44 cm, which does match the value of the preferred horizontal wavelength found previously. This preferred wavelength is therefore the scale at which the wave-induced energy flux is maximum.

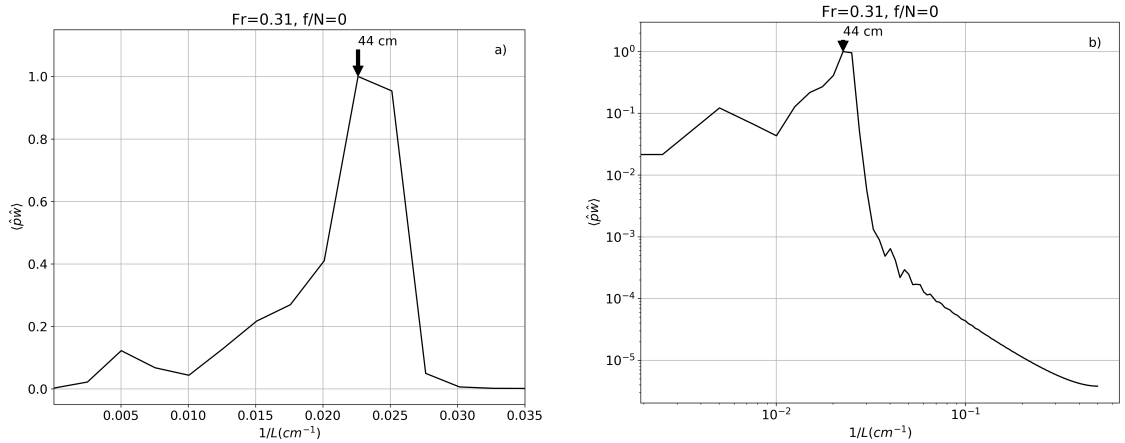

Figure 4.8: Fourier transform along the $x-$direction of the wave-induced energy flux $\overline{\hat{p}'\hat{w}^*}$ as a function of the horizontal wavenumber k_x (a) lin-lin plot, (b) log-log plot. The computation has been performed at $t = 30$ buoyancy periods (during the steady regime), for $z = 23$ cm and using an average over the horizontal $y-$direction.

4.3 Analysis of the wake field

4.3.1 Vertical structure of the wake field

In chapter 3 it was stated that, due to the conservation of energy, a density stratified fluid which encounters an obstacle is divided into two different regions by a DSL. Above the DSL, the fluid parcels with enough kinetic energy to rise over the top of the obstacle produce IGWs, while the fluid parcels below the DSL which do not have enough kinetic energy to rise over it, follow a quasi-horizontal trajectory around the cap with no IGW generation.

The behavior exhibited above the DSL was explored in the previous sections. In this section, the interest is focused on the processes below the DSL, near the bottom of the domain. In this region, the flow that goes around the cap leads to the formation of a wake behind the cap.

A preliminary view of the wake structure was displayed in figure 4.1. However, since the color scale was chosen to display the wave field, it was not well suited to represent the wake field. To better display the latter part of the flow, this figure was reproduced with the color scale now spanning the whole range of values of u', this component being scaled by U_0, see figure 4.9.

The striking feature of figure 4.9 is that the extension and amplitude of the wake decrease as the Froude number increases. Since the flow goes around the cap and creates a wake below the DSL, this result is accounted for qualitatively by the fact that the DSL moves toward the bottom as Fr increases. For $Fr = 1.25$, the DSL is at the bottom (in other words, there is no DSL) implying that the whole flow passes over the cap and almost no wake forms. By contrast, when $Fr = 0.31$, the height of the dividing streamline is close to the top of the cap (at 13.8 cm) so that a substantial part of the flow goes around the cap

which creates the wake. In all configurations, figure 4.9 shows that the streamwise velocity is locally negative in the wake, and therefore associated with a return flow, whose amplitude decays (in absolute value) as Fr increases. This wake extends over a length that decreases and is located closer to the cap as Fr increases. The wake structure is further discussed in section 4.3.2 below.

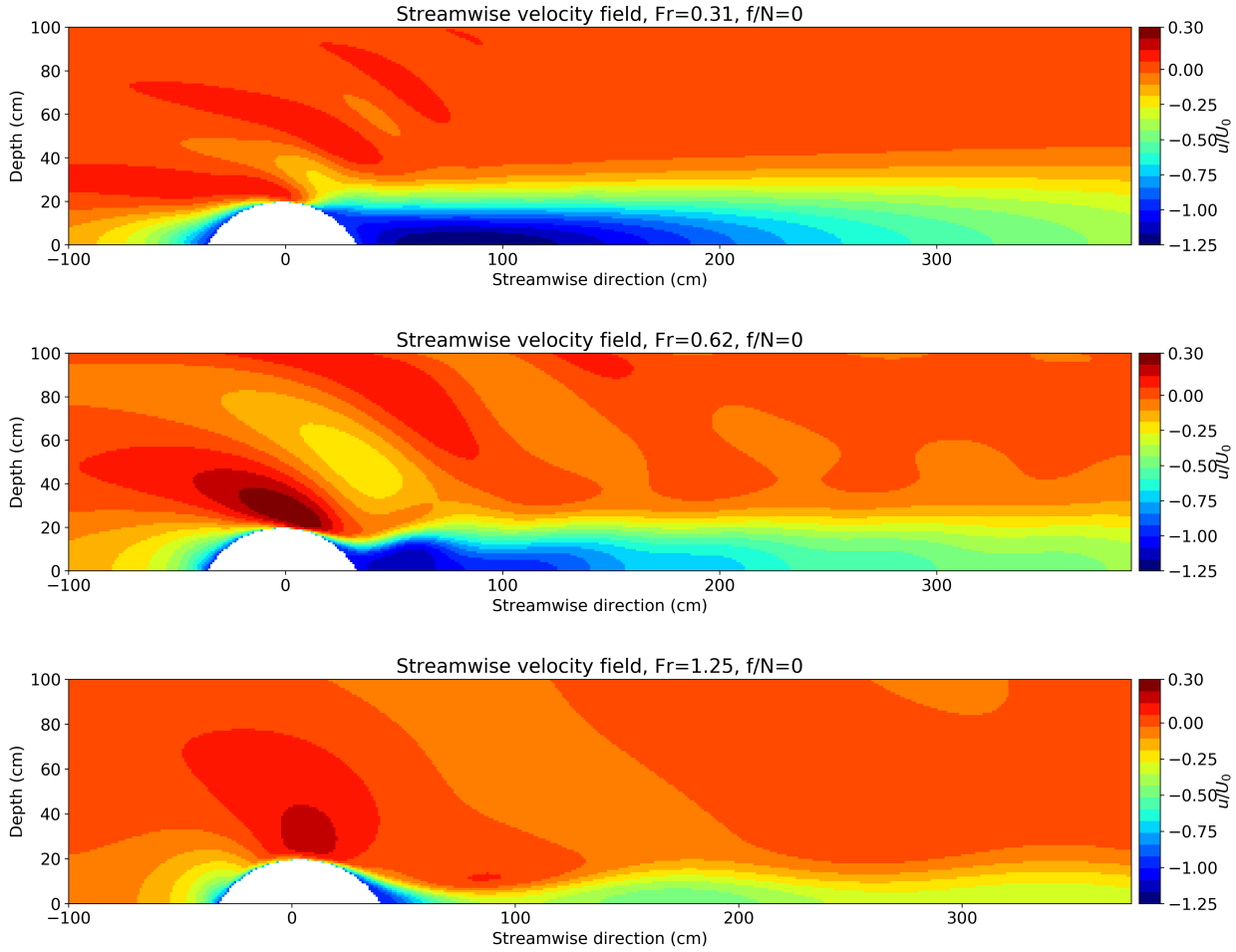

Figure 4.9: Cross-section of the streamwise velocity deviation in the vertical center plane for $Fr = 0.31$ in the first row, $Fr = 0.62$ in the second row and $Fr = 1.25$ at the bottom row. The minimum value of u/U_0 is about -1.27 for $Fr = 0.31$, -1.15 for $Fr = 0.62$, and it is close to 0 for $Fr = 1.25$, thus, the wake amplitude decreases as Fr increases.

4.3.2 Analysis of the blocking effect

The blocking of the flow by the cap is analyzed in this section by displaying again u'/U_0, now in a horizontal plane just above the bottom of the domain for the three flow rates we consider (figure 4.10).

In all three cases an increase of the flow rate occurs along the sides of the obstacle due to the conservation of mass flux. By contrast, this figure shows a flow rate deficit before and after the cap. These effects are more important for low Froude numbers than for high values.

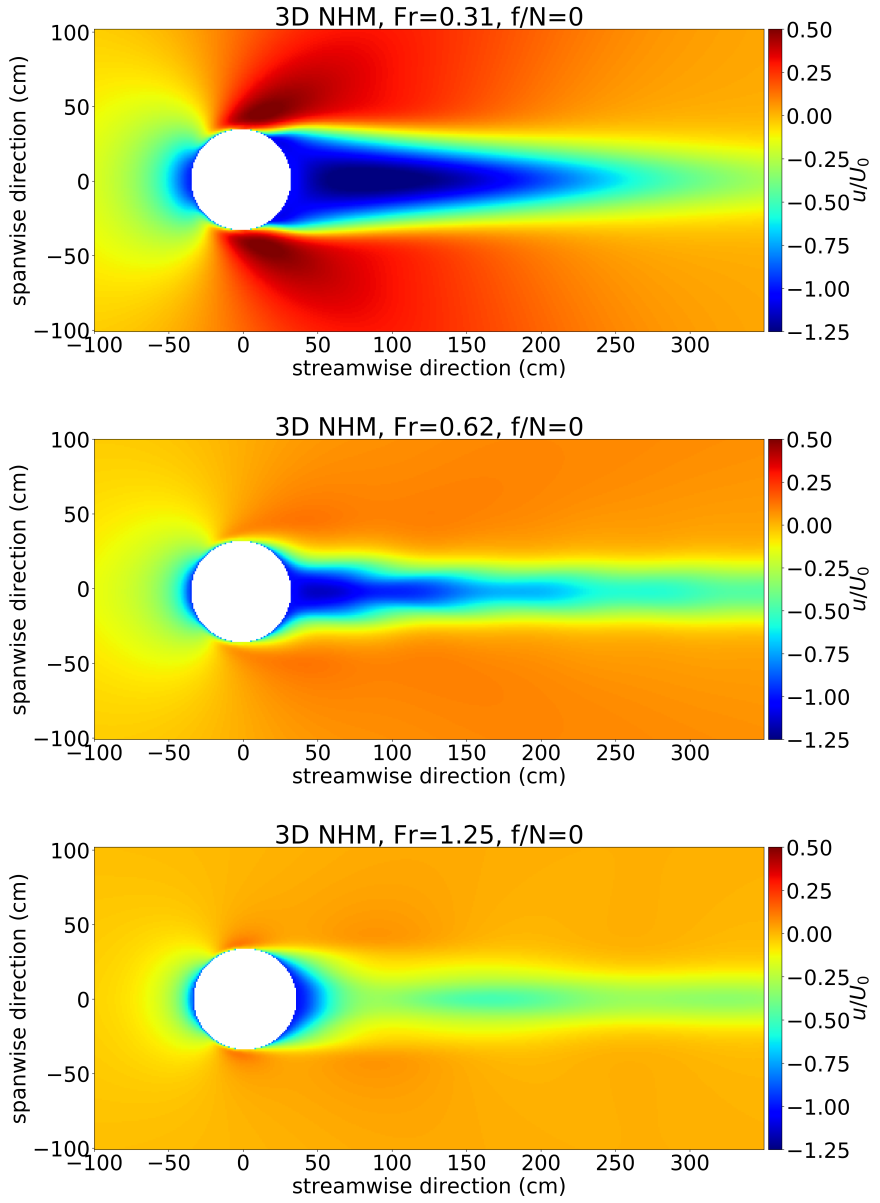

Figure 4.10: Streamwise velocity deviation normalized with the incoming flow showing the blocking of the flow at 1 cm above the bottom of the domain. Computed from the three-dimensional model for a) $Fr = 0.31$ at the top, b) $Fr = 0.62$ in the middle and c) $Fr = 1.25$ at the bottom.

The figure for $Fr = 0.31$ shows a very strong blocking effect behind the cap which even produces a recirculation zone there. The wake extends far away from the obstacle with a reduction of the flow speed of 80% at a distance of 4 topographic diameters and of 50% at about 6 topographic diameters. A similar behavior, but with a weaker intensity, is observed for $Fr = 0.62$: there is a strong decrease of the flow speed in the central axis behind the cap and an acceleration on the sides of the cap. The wake is narrower than for $Fr = 0.31$, and the reduction factor along the central axis at 6 topographic diameters is of 60% (against 50% for $Fr = 0.31$). The reduction in flow speed for $Fr = 1.25$ occurs much closer to the cap: this factor is of 80% for the first 1/3 topographic diameter, and the flow speed recovers

70% of its upstream value just after this location.

4.3.2.1 Comparison with the laboratory experiments

In order to characterize the quasi-horizontal flow in the bottom part of the physical domain, the vertical vorticity component is displayed in figure 4.11 for the three flow rates we consider, for the experimental measurements and the numerical simulations.

The blocking of the lower part of the fluid by the cap results in a wake laterally delimited by two bands of opposite vorticity. The magnitude of the vorticity increases with Fr, the maximum values being reached around the cylinder in the numerical simulations where the streamlines get closer (we remind that no boundary layer forms on the cap in the simulation due to the free-slip boundary condition). In the present case with no rotation, the wake is fairly straight, with no vortex shedding that would result from an unstable behavior. The laboratory experiments display a turbulent wake, while the latter wake is laminar in the numerical simulations. The reason lies in the experimental Reynolds number being 100 times larger than in the three-dimensional simulations, with a value of 6000 against 60 for $Fr = 0.31$. Overall, one can conclude that a qualitatively good agreement is obtained between the laboratory experiments and the numerical simulations.

Despite the horizontal cross-section of the cap resembles that of a horizontal cylinder, the analogy with the wake developing behind a cylinder should be considered cautiously. Indeed, the critical Reynolds number for the wake behind a cylinder to become unstable and lead to the formation of symmetric counter-rotating vortices is about 40 [Kovasznay, 1949a]. This critical value seems to be much higher for the cap obstacle we consider in the present study since the wake remains stable for $Re = 6000$.

4.3.3 Change in the momentum flux due to the cap

The objective of the present section is to compute the change in the momentum flux due to the obstacle and to compare it to the momentum transported vertically by the waves, when the Froude number varies. The latter flux was computed in section 4.2.5.

Since the source of momentum is the mean current U_0 which is along the $x-$axis, we consider the momentum conservation equation for the $x-$component u integrated over a volume comprising the obstacle. Denoting this volume by $\mathcal{V}$ and its bounding surface by $\mathcal{S}$, this momentum budget obeys the following equation (per unit mass), using the divergence theorem:

$$\frac{\mathrm{d}}{\mathrm{d}t}\int_{\mathcal{V}} u\,\mathrm{d}^3\mathbf{x} = -\int_{\mathcal{S}} u\,u_j n_j\,\mathrm{d}\mathcal{S} - \frac{1}{\rho_0}\int_{\mathcal{S}} p'\delta_{1j}n_j\,\mathrm{d}\mathcal{S} - \mathrm{VSS}. \tag{4.5}$$

The terms on the right-hand-side represent the net advective flux across the boundary of the volume $\mathcal{V}$, the pressure force on the boundary normal to the $x-$direction and the viscous shear stress at the boundary (VSS), respectively. The symbol δ_{ij} is the Kronecker delta with $i = 1$ in the present case since the $x-$component is considered.

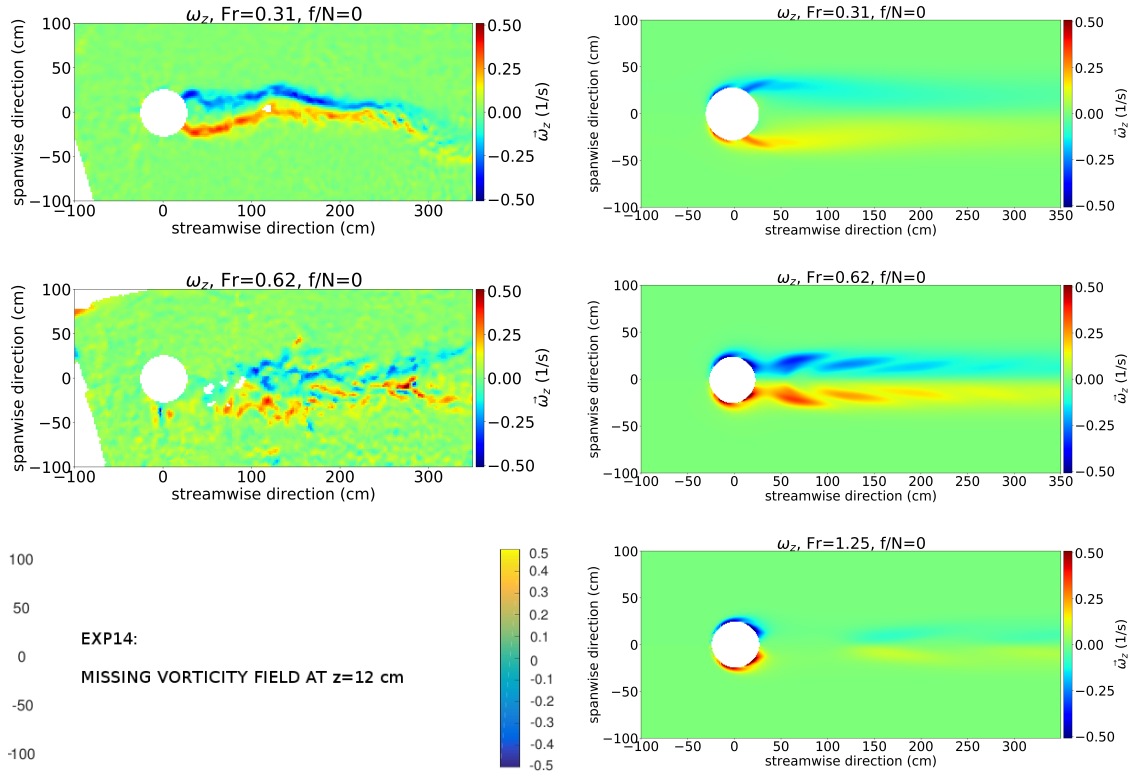

Figure 4.11: Vorticity field at 12 cm above the bottom of the domain for a) $Fr = 0.31$ at the top, b) $Fr = 0.62$ in the middle and c) $Fr = 1.25$ at the bottom. Left column: PIV experiments, right column: three-dimensional numerical simulation. The same values for the color bar are chosen for all cases for comparison purpose. The minimum and maximum values for the numerical simulations are the following: $[-0.52, 0.52]$ for $Fr = 0.31$, $[-0.75, 0.77]$ for $Fr = 0.62$ and $[-0.67, 0.69]$ for $Fr = 1.25$.

The volume $\mathcal{V}$ we consider is a parallelepipedic box lying on the bottom floor whose upper boundary is the horizontal plane located at $z = z_{top}$ with $z_{top} = 23$ cm. The volume extends from $x_0 = -d$ to $x_1 = 3d$ in the $x-$direction and from $y_0 = -100$ cm to $y_1 = 100$ cm along the $y-$direction.

With this choice for $\mathcal{V}$, equation (4.5) becomes:

$$\begin{aligned}
\frac{\mathrm{d}}{\mathrm{d}t}\int_{\mathcal{V}} u\,\mathrm{d}^3\mathbf{x} = \; & - \int_{y_0}^{y_1}\int_{0}^{z_{top}} \left[\, u^2(x_1,y,z,t) - u^2(x_0,y,z,t) \,\right] dy\,dz \\
& - \int_{x_0}^{x_1}\int_{0}^{z_{top}} \left[\, (u\,v)(x,y_1,z,t) - (u\,v)(x,y_0,z,t) \,\right] dx\,dz \\
& - \int_{x_0}^{x_1}\int_{y_0}^{y_1} (u\,w)(x,y,z_{top},t)\,dx\,dy \\
& - \frac{1}{\rho_0}\int_{y_0}^{y_1}\int_{0}^{z_{top}} \left[\, p(x_1,y,z,t) - p(x_0,y,z,t) \,\right] dy\,dz \\
& - D - \mathrm{VSS}.
\end{aligned} \tag{4.6}$$

The momentum flux terms involving the surface integral of uv on the lateral sides of the volume (second line) and of uw at the top of the domain (third line) must be taken

into account since they involve the momentum transport by the lee waves. The velocity component normal to the bottom vanishes due to the impermeability condition so that the flux across this surface is equal to zero as well and does not appear on the third line. The fourth line is the pressure force exerted on the lateral boundaries of the volume. Finally, because the bottom boundary of the volume involves the cap boundary, the horizontal projection of the pressure force on that cap should be considered. This is the term $-D$ which represents the drag force exerted by the cap on the flow, due to wave emission and to the wake formation. This is the term we wish to compute. It will be deduced from the momentum balance, assuming a steady state is reached and ignoring the viscous term, namely

$$\begin{aligned} -D = & \int_{y_0}^{y_1}\int_{0}^{z_{top}} \left[\, u^2(x_1,y,z,t) - u^2(x_0,y,z,t) \,\right] dy\, dz \\ + & \int_{x_0}^{x_1}\int_{0}^{z_{top}} \left[\, (u\,v)(x,y_1,z,t) - (u\,v)(x,y_0,z,t) \,\right] dx\, dz \\ + & \int_{x_0}^{x_1}\int_{y_0}^{y_1} (u\,w)(x,y,z_{top},t)\, dx\, dy \\ + & \frac{1}{\rho_0}\int_{y_0}^{y_1}\int_{0}^{z_{top}} \left[\, p(x_1,y,z,t) - p(x_0,y,z,t) \,\right] dy\, dz. \end{aligned} \tag{4.7}$$

The four terms of the right-hand side have been computed at a given time during the steady regime and their values are reported in table 4.6 for the three Froude numbers we consider. The value of the total drag force is inferred from equation (4.7) and is indicated in the penultimate column of the table. We find again that the drag force is twice larger for $Fr = 0.67$ than for the two other values of Fr.

Fr	$\frac{\Delta\langle u^2\rangle_{yz}}{U_0^2}$ (cm^2)	$\frac{\Delta\langle uv\rangle_{xz}}{U_0^2}$ (cm^2)	$\frac{\Delta\langle uw\rangle_{xy}}{U_0^2}$ (cm^2)	$\frac{\langle w\rangle_{xy}}{U_0}$ (cm^2)	$\frac{D}{U_0^2}$ (cm^2)	$C_{D_{\text{total}}}$
0.31	-676.61244	-487.3504	12.6891	-100.6951	1251.9688	0.1797
0.62	-235.8714	-234.4729	-225.2732	-1121.7437	1817.3613	0.2307
1.25	0.7593	-7.7499	-107.5607	796.1311	-681.5799	0.1008

Table 4.6: Terms involved in the momentum budget of the $u-$component (see equation (4.7)), normalized by U_0^2. $\Delta\langle uw\rangle_{xy}/U_0^2$ refers to the first column, $\Delta\langle uv\rangle_{xz}/U_0^2$ to the second column, $\Delta\langle uw\rangle_{xy}/U_0^2$ to the third column and $\Delta\langle p\rangle_{yz}/U_0^2$ to the fourth column. The 6th column is the horizontal average of w/U_0 on the top boundary of volume $\mathcal{V}$, the 7th column is the total drag force D normalized by U_0^2 defined by equation (4.7) and the last column is the total drag coefficient defined by (4.8).

From this drag force, a drag coefficient denoted $C_{D_{total}}$ can be computed by the expression

$$D = 0.5\, C_{D_{total}}\, S\, U_0^2, \tag{4.8}$$

where S is the whole surface of the cap facing the flow (see equation (4.4) with $h_{eff} = h$).

The values of $C_{D_{total}}$ are indicated in the last column of table 4.6.

The total drag force is contributed both by the waves and by the wake, as mentioned above, and one can assume these contributions to be independent. Thus, the drag coefficient for the wake is simply expressed by

$$C_{D_{wake}} = C_{D_{total}} - C_{D_{wave}}. \tag{4.9}$$

The drag coefficients for the wake are indicated in table 4.7 for the three Froude numbers we consider, and the coefficients for the wave already presented in table 4.4 have been reported for comparison purpose.

Fr	Fr_{hor}	$C_{D_{\text{waves}}}$	$C_{D_{\text{total}}}$	$C_{D_{\text{wake}}}$
0.31	0.177	0.0104	0.1797	0.1692
0.62	0.354	0.1562	0.2307	0.0744
1.25	0.714	0.0963	0.1008	0.0044

Table 4.7: Comparative table of the drag coefficients induced by the wave and the wake fields for the non rotating system.

We observe that the drag coefficient associated with the wake decreases with the Froude number. This is to be expected, since the amplitude of the wake decreases with the Froude number. Likewise, we observe that the drag coefficient associated with the waves increases from $Fr = 0.31$ to $Fr = 0.62$ but then it decreases from $Fr = 0.62$ to $Fr = 1.25$, which is surprising. A priori, as the wave amplitude increases with the Froude number, we might expect that the drag coefficient associated with waves production should increase as the Froude number increases, but this is not the case.

The fact that the drag coefficient associated with waves production is larger for $Fr = 0.62$ than the one found for $Fr = 1.25$ can be explained qualitatively as follows: the wave induced drag is a consequence of the emission of the waves, and the wave induced drag is proportional to the square of its amplitude. We have seen that the amplitude of the internal gravity waves is imposed by the boundary condition on w. Now, even if the amplitude of the waves for $Fr = 1.25$ is larger than the amplitude observed for $Fr = 0.62$, it does not compensate for the factor $U_0^2 = 4$ in the definition of the drag coefficient. Indeed, the amplitude of the internal gravity waves is imposed by the boundary condition on w, from figure 5.3 we observe that there is a factor $2 \times 1.16 = 2.32$ between the wave amplitude for $Fr = 0.62$ and $Fr = 1.25$. Now, as a consequence of the dividing stream line, there is a factor 1.98 between the effective area evolved in the waves production is not for $Fr = 1.25$ and $Fr = 0.62$ (see equation (4.3)). Taking into account these values we get an estimated value for the drag coefficient for $Fr = 1.25$: $C_{D_{\text{total}}}|_{Fr=1.15} \approx C_{D_{\text{total}}}|_{Fr=0.62} \frac{w^2_{Fr=0.62} S_{Fr=1.25}}{w^2_{Fr=1.25} S_{Fr=0.62}} \approx 1.98 \frac{0.7870}{2.32^2} = 0.2894$ and $C_{D_{\text{total}}}|_{Fr=1.15} \approx 0.3262$, for the rotating system and non-rotating system, respectively. As we find a good agreement between these qualitative values and the ones computed from the simulation, we can conclude that the maximum value for the drag

coefficient associated with the waves occurs for a $Fr \lesssim 1$, where there is a balance between the available kinetic energy and the effective surface of the sphere. In other words, this behavior in the drag force associated to the wave emission, is linked to the fact that there is too much kinetic energy that might be used to produce waves but the effective surface of the sphere is not enough to produce them, so there is a sort of wave saturation [Greenslade, 2000].

4.4 Conclusions

In this chapter, the results obtained from the three-dimensional numerical simulation for the system presented in chapter 2, in the absence of rotation, are presented, described and analyzed. As a reminder, the system consists of a spherical cap topography in a fluid that is linearly stratified in density. This fluid flows over the topography at a constant flow rate of U_0. In this study we consider three different flow rates corresponding to three different values of Froude numbers: $Fr = 0.31$, $Fr = 0.62$ and $Fr = 1.25$.

The considered flow is modified by the interaction with the cap that leads to two different behaviors: an oscillating behavior (internal gravity waves) and a turbulent behavior (wake). The internal gravity waves cover most of the physical domain, and the wake is confined to the bottom of the physical domain.

In this chapter, we are interested in studying and quantifying the momentum transfers in the fluid due to this wave and the wake fields. We are also interested in characterizing these fields in the absence of rotation. In order to do it, three different approaches were adopted: experimental PIV measurements, three-dimensional numerical simulations, and linear theory. As justified in chapter 3, the linear theory includes the DSL hypothesis, as it provides an important correction to the amplitude of the waves. The results are presented as a comparison with the experimental results since it was this configuration that motivated this thesis.

For each of the Froude numbers considered here, as expected, the lee wave field remains constant in the frame of reference where the topography is at rest. We recall that through the boundary condition, the topography can be considered as a source of waves that emits waves with the spectrum of this topography. Since it is considered a spherical topography, with a continuous Fourier spectrum, we expect to observe a wide spectrum of wavelengths that satisfy the dispersion relation. However, as in the linear theory results, a preferred wavelength is observed for all Froude numbers. This preferred wavelength is set by the value U_0/N for all the Froude numbers, which for $Fr < 1$, is the effective size of the topography, as it is for a 2D-sinusoidal topography.

We recall that the introduction of the dividing streamline hypothesis involves a significant correction to the amplitude of the waves. That is why its introduction helps us to understand how the amplitude of the waves increases with the Froude number. As the amplitude of the waves can be easily seen from the vertical component of the velocity w, and the amplitude

of this velocity is set by the boundary condition on the topography, then the amplitude of the waves is set by this boundary condition. Hence, the amplitude of the waves depends on the mean flow velocity as $w \sim U_0 h_{\text{eff}} = U_0^2 N$ for $Fr < 1$ and as $w \sim U_0$ for $Fr > 1$.

When a horizontal cross-section of the wave field is taken in the far-field, $z \sim 3h$, we observe a regularly spaced parabolic wave pattern for all the considered Froude numbers. We observe that as Fr increases, the parabolic shape becomes narrower, just as for the linear theory. If we take a vertical cross-section of the vertical velocity field, along the central streamwise axis, we observe that the angle θ that the wave vector makes with the vertical increases as the Froude number increases.

The wake field is confined to the bottom of the physical domain, and its structure is characterized in this chapter for the non-rotating system. A horizontal cross-section of the streamwise velocity, u, is computed at the bottom of the physical domain to characterize the wake. This cross-section shows a flow deficit behind the topography. In the simulation, this flow deficit induces a baroclinic instability, which, even with no boundary-layer leads to the production of the wake. The produced wake, is made of two bands of opposite vorticity. We compute the vertical vorticity for the three-dimensional numerical simulations and the PIV experimental measurements at $z = 13$ cm above the bottom, even if the mechanism of production is different, due to the detachment of the boundary layer, in this case, we observe a similar behavior with the one observed from the numerical simulations.

We observe that as the Froude number increases, the intensity and extension of the wake decreases. The DSL hypothesis provides a good explanation for this observation because it explains the existence of the quasi-horizontal flow that leads to the formation of a wake in a stratified flow. As the height of the DSL, decreases as Fr increases, we expect to observe a decrease in the quasi-horizontal motions as Fr increases. Hence, we expect to observe a decrease in the wake intensity as Fr increases which is our case.

As one of the main objectives of this work is to quantify the momentum transfers in the fluid, we quantify the momentum transfer due to the waves and the wake. These transfers are studied through the wave drag coefficient $C_{D_{\text{waves}}}$ and the wake drag coefficient $C_{D_{\text{wake}}}$, respectively. We observe that the drag induced by the wake decreases as Fr increases. Indeed, for $Fr > 1$ the induced drag by the wake is negligible as expected from [Voisin, 2007].

Now, as the wave amplitude increases with the Froude number, we might expect that the drag coefficient associated with wave production should increase as Fr increases, but this is not the case. The wave-induced drag coefficient increases for $Fr < 1$ and then it seems to reach a maximum value for a Froude number, Fr, such that $Fr \lesssim 1$. In other words, taking into account the DSL hypothesis, this behavior in the drag force associated with the wave emission, seems to be linked to the fact that there is too much kinetic energy that might be used to produce waves; but, the effective surface of the sphere is not enough to produce them.

Taking into account the induced drags by the wake and by the waves we can understand

the existence of a local maximum for the drag coefficient. This local maximum is the result of the combination of the wave and wake drags. One can find indeed that there is a local maximum for the value of the drag coefficient around $Fr = 0.62$, where about half of the height of the topography is involved in active wave emission, and the other half produces the wake. Another experimental and theoretical works (see for further information [Voisin, 2007]) showed that this coefficient depends in a non-trivial way on the Froude number reaching a maximum value for Froude numbers close to $Fr = 2/3$. These results are in a very good agreement with our results.

5

Experimental and numerical study of a lee wave field produced by a spherical cap in a rotating system

5.1 Introduction

In this chapter the effect of background rotation on the three-dimensional numerical simulations and experimental PIV measurements is presented and analyzed for the system described in chapter 2. The comparison with linear theory is also discussed. The non-rotating three-dimensional numerical simulations presented in chapter 4 are used as a reference to understand better the rotation impact on the dynamics of the wave and the wake. Thus, some of the results presented in chapter 4 are compared with the respective rotating fields in the present chapter.

We recall that we consider a constant flow $\vec{U_0} = (U_0, 0, 0)$ flowing over a topography under the influence of rotation. As in the non-rotational case, the flow is modified by the interaction with the topography leading to two different behaviors: an oscillating behavior and a turbulent behavior. The oscillating part is mainly composed of Inertial Oscillations (IOs) and Internal Gravity Waves (IGWs) that cover most of the physical domain. The non-oscillating turbulent behavior, called here a wake, is confined to the bottom of the physical domain.

Like in the non-rotating case, the experimental and numerical results show that the wave and wake fields exist in different zones of the physical domain, with a small zone of interaction. This is why they are described and analyzed in different sections: the wave field analysis is reported in section 5.3 and the wake field analysis is described in section 5.4. Finally, the results are discussed and summarized in section 5.6.

In the following, the *vertical center plane* refers to the vertical (x, z) plane containing

the streamwise symmetry axis. We remind that the *streamwise velocity deviation* u is the departure of the streamwise velocity U with respect to the constant flow U_0.

5.2 Overall flow behavior

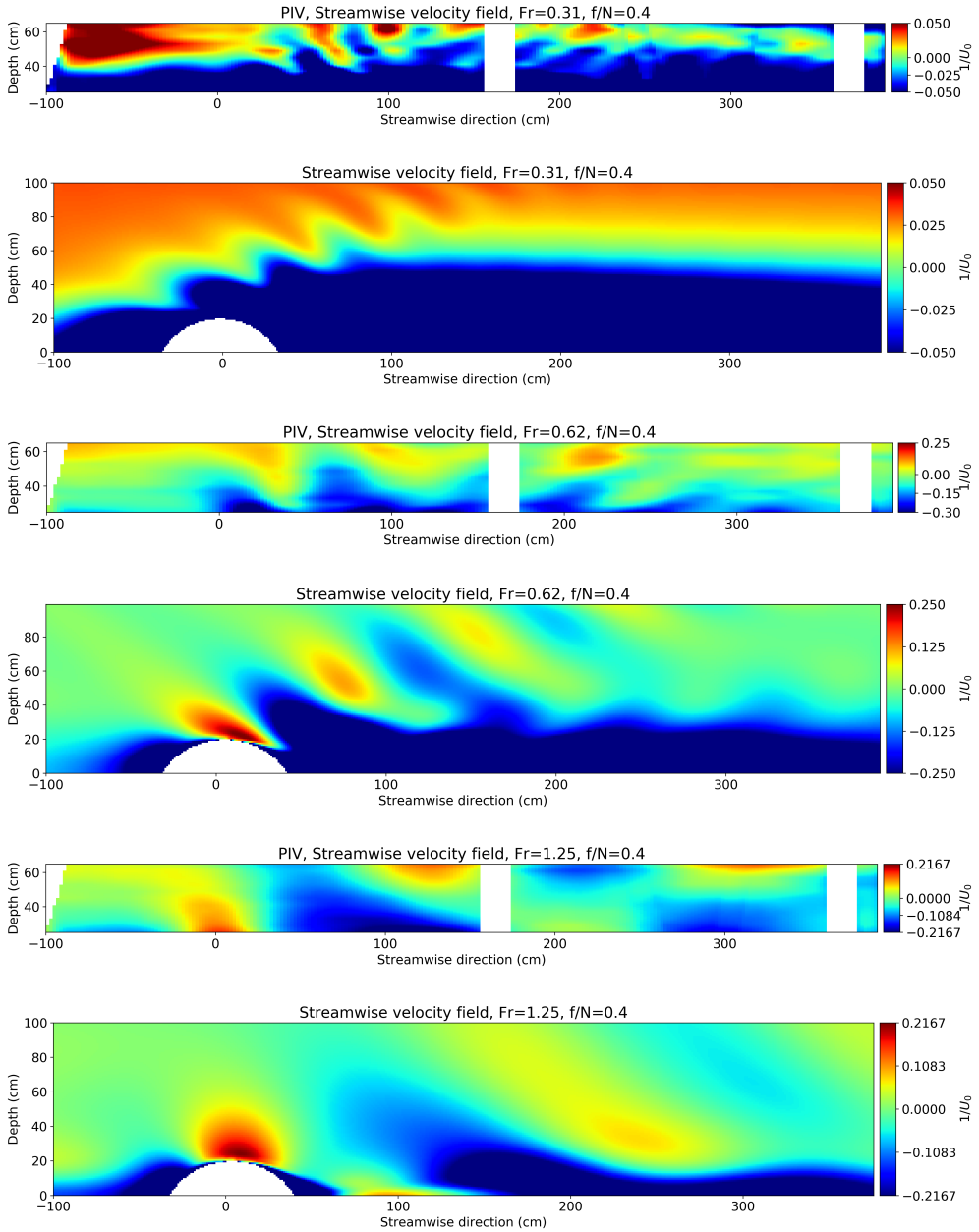

Figure 5.1: This figure shows a vertical cross-section of the streamwise velocity field along the central-streamwise axis for each of the three Froude numbers with rotation. All the streamwise velocity deviations are adimensioned with U_0 to simplify comparisons. It displays the results for $Fr = 0.31$ in the first two rows, the results for $Fr = 0.62$ in the third and fourth lines, and the results for $Fr = 1.25$ in the last two lines. The PIV measurement results are in the odd lines for the depth ranging in $z \in [25, 62]$ cm and the ones from the three-dimensional simulations in the even lines for the depth ranging in $z \in [0, 100]$ cm.

Figure 5.1 shows a general view of flow behavior, with the streamwise velocity deviation (u) being displayed in the vertical central plane for a rotating system with $\frac{f}{N} = \frac{0.19\ s^{-1}}{0.48\ s^{-1}} = 0.4$. The results for $Fr = 0.31$ ($U_0 = 3$ cm/s) are displayed in the first two rows, the results for $Fr = 0.62$ ($U_0 = 6$ cm/s) in the third and fourth lines, and the results for $Fr = 1.25$ ($U_0 = 12$ cm/s) in the last two lines. The PIV measurement results are in the odd lines for the depth ranging in $z \in [25, 62]$ cm and the ones from the three-dimensional simulations in the even lines for the depth ranging in $z \in [0, 100]$ cm. Like the non-rotating case, we observe two different behaviors: one at the upper part of the physical domain, where only waves exist, and another at the lower part, where a wake is observed behind the topography.

Unlike the simulations, where a sponge was included on the surface of the water at $z = 98$ cm from the bottom, in the experimental measurements, the system is delimited by the free surface of the water at $z = 92$ cm. Due to the difference in density between water and air, the free surface of the water is a semi-reflective surface for internal waves. For instance, the frames in the odd lines of figure 5.1, show the wavefield disturbed by the reflections of the waves on the water surface that return to the physical domain and interfere with the rising waves. Despite this wave interference, there is a good qualitative agreement between the experimental and numerical vertical-crossed sections for all the Froude numbers.

The value of u at each of the observed maximum in figure 5.1 is plotted in figure 5.2 as a function of time up to 13 inertial periods. It is plotted for $Fr = 0.31$ on the first line from the 2 inertial periods to the end of the simulation, at 13 inertial periods. Each of the values is drawn with a different colored line. Then, these curves are averaged, and the averaged function is drawn in the same figure with a fat black line. The wave period of this averaged function is measured and shown in this figure. The first frame of this figure shows that the positions of the maximums of the wave field do not vary in time. But, the equilibrium value oscillates with a period of oscillation of one inertial period. This temporal evolution also is plotted for $Fr = 0.62$ in the second line and $Fr = 1.25$ in the bottom line. We observe the same behavior for $Fr = 0.62$ as the one obtained for $Fr = 0.31$. For $Fr = 1.25$, each of the positions of the maximums varies in time with the same period as IOs do. But, they are slightly out of phase damping down the averaged function. It means that we observe a temporal oscillation phenomenon with a long horizontal wavelength, which oscillates at the same frequency as IOs do. From this observation, it is possible to claim that these oscillations are due to the presence of IOs. Unlike the results obtained by [Nikurashin and Ferrari, 2010a], these oscillations do not grow over time, so we do not see an evidence of resonant interactions between these IOs and the IGWs up to the end of our simulations.

Like in the non-rotating case, there is a strong flow deficit at the bottom of the domain (plotted in blue at the bottom of each frame of figure 5.1). This blocking of the flow is due to the wake effect. The mean flow oscillations, shown in figure 5.2, affect the whole vertical column of water. Thus, the wake is modified, and its structure is no longer a wake of two opposite sign vorticity bands, but it is a wake of eddies as will be discussed in section 5.4.

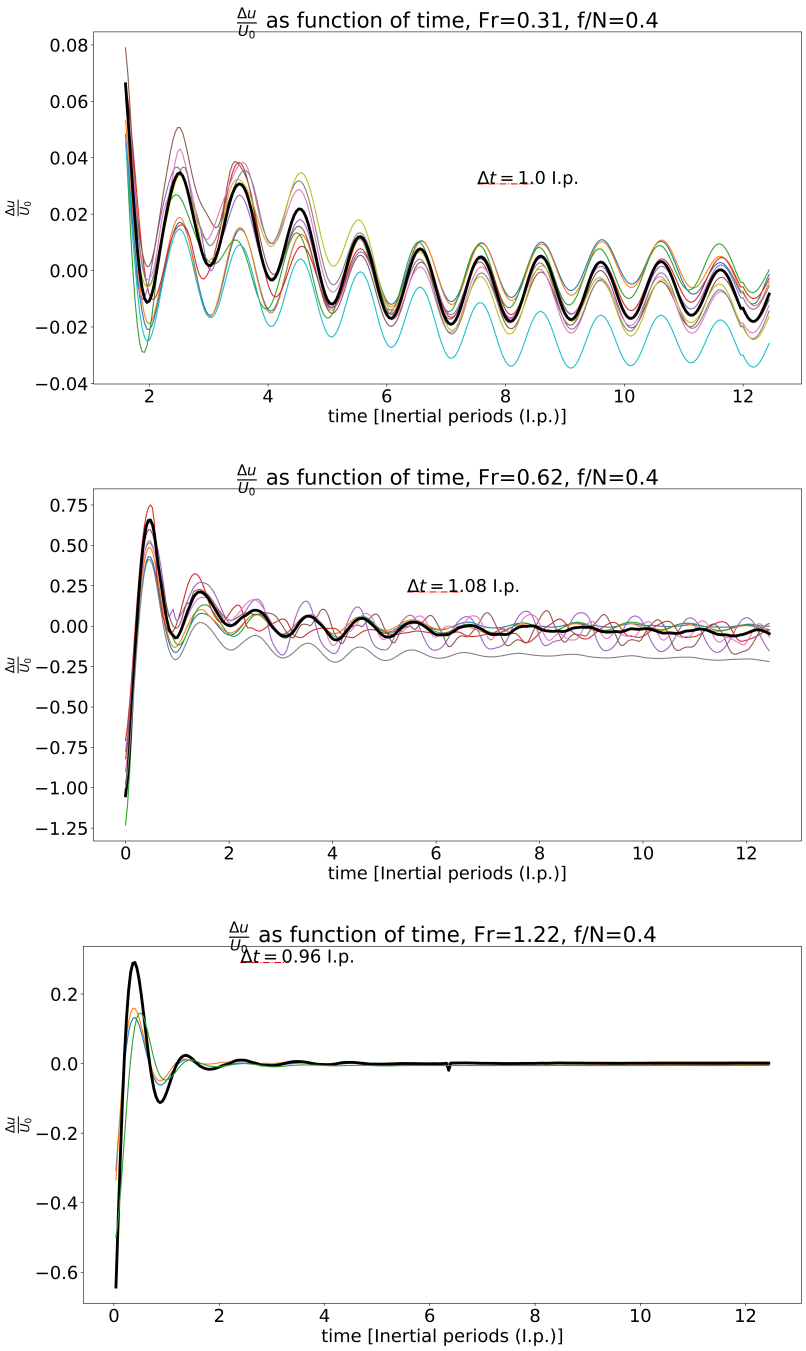

Figure 5.2: Amplitude vs time at six selected points for $Fr = 0.31$ in the first row, $Fr = 0.62$ in the second row and $Fr = 1.25$ in the bottom row.

5.3 Analysis of the lee wave field with $f/N \neq 0$

5.3.1 Structure of the three-dimensional wave field

5.3.1.1 Vertical structure of the wave field

A cross-section of the vertical velocity field in the vertical center plane is displayed in figure 5.3 for the three values of the Froude number we consider. For $Fr < 1$, the very

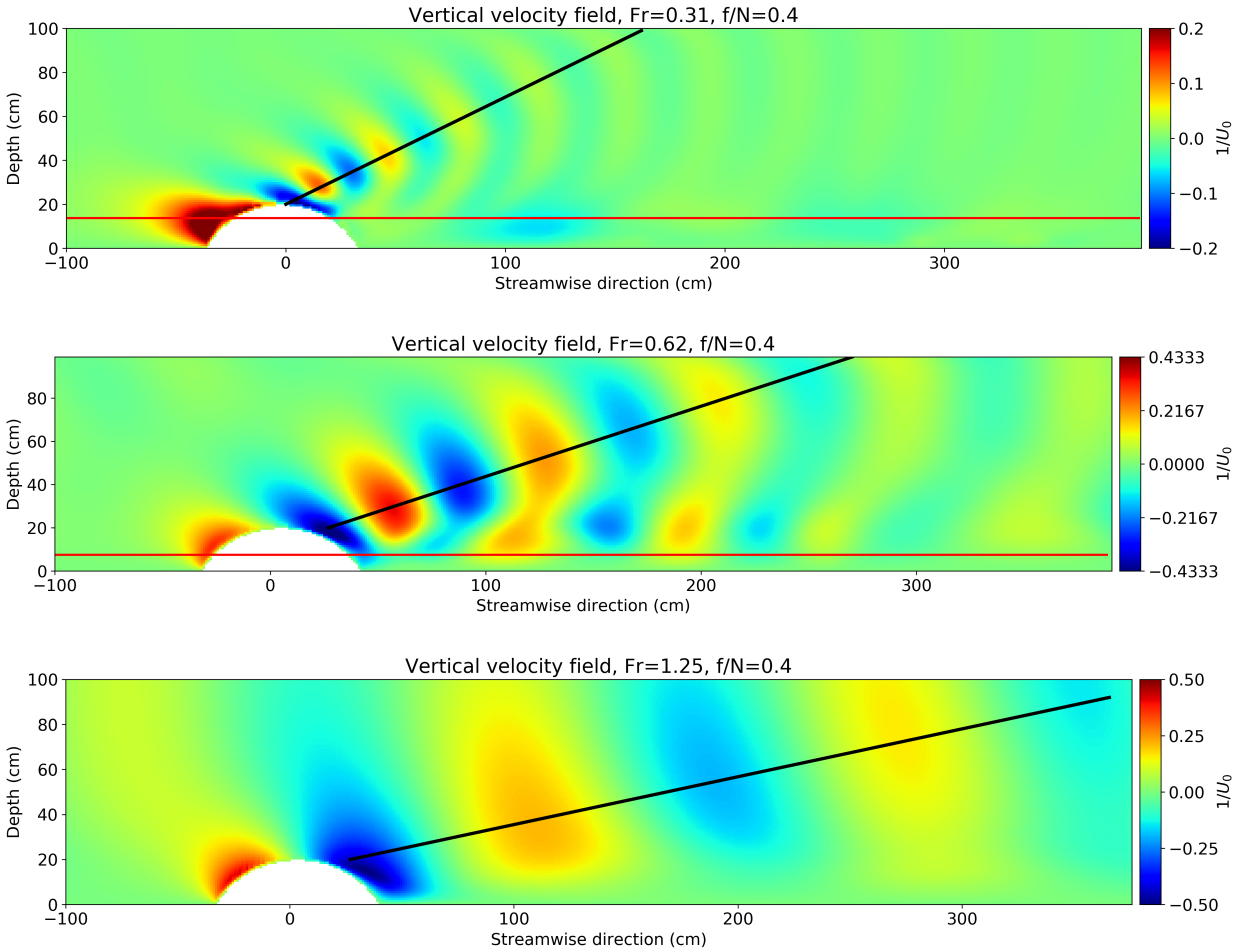

Figure 5.3: Vertical cross-section along the streamwise axis of the vertical velocity field for the rotating system for each of the Froude numbers we consider. All the vertical velocity fields are adimensioned with U_0 to simplify comparisons. In the first row, it is displayed for $Fr = 0.31$, in the middle one for $Fr = 0.62$ and, in the third row for $Fr = 1.25$. The height of the dividing streamline is drawn with a red line in the frames with $Fr < 1$ (for $Fr > 1$, there is no dividing streamline). The black line is normal to phase lines and indicates that there is a preferred wave vector. The angle that this vector makes with the vertical, denoted θ in the text, is indicated in the first frame.

bottom of the physical domain does not show any waves below the height of the dividing streamline (which is a surface here) that divides the flow into the wave and no-wave flow zones, above and below the dividing streamline, respectively. We recall that the height of the dividing streamline (from the bottom plane) is given by $h_s = (1 - Fr)h$, where h is the height of the cap, so that $h_s = 13.8$ cm for $Fr = 0.31$ and $h_s = 7.6$ cm for $Fr = 0.62$. These heights are indicated with a horizontal red line in figure 5.3. Hence, just like in the non-rotating case, waves are emitted only above the dividing streamline, in agreement with the theoretical prediction of [Voisin, 2007].

Like in the non-rotating configuration, for $Fr = 0.31$ and $Fr = 0.62$ (top and middle frames of figure 5.3, respectively), above the wake and far enough from the topography downstream, is observed that the phase lines of lee waves in the vertical plane have a circular

form. Below the dividing-streamline, the form of the phase lines changes, becoming more vertical for $Fr = 0.31$ and for $Fr = 0.62$. Unlike the non-rotating case, shown in figure 4.9, where the wake was associated with a recirculation zone behind the topography, the wake in the rotating case, shown in figure 5.8 is associated with shedding vortices which induce a vertical shear. These ejected vortices rotate alternately, clockwise or counter-clockwise, with positive or negative vorticity along the $z-$axis, respectively. These phase lines are even twisted in the opposite direction when interact with the moving vortices. The corresponding induced shear varies over time as the vortex moves away from the topography and refracts the waves, which may explain the change in shape of the phase lines.

The amplitude of the waves, which can be easily seen from the vertical component of the speed w displayed in figure 5.3, increases with the Froude number. Just like in the non-rotating case, the amplitude of the waves observed for $Fr = 0.62$ is 2 $U_0 = 4$ times greater than the amplitude of the waves for $Fr = 0.31$. We recall that it can be explained qualitatively from the boundary condition on the topography, which imposes the amplitude of w by considering the DSL hypothesis.

As in the non-rotational case, the wave pattern shown in figure 5.3 contains a main beam. This beam has a propagation vector, $\vec{k}$, which is perpendicular to the phase lines. The black line in the figure connects the points of maximum amplitude of the oscillations, and its direction coincides with the propagation direction of the group velocity. As already described in chapter 4, it is surprising to have a main beam in a system in which the topography that drives the waves is a spherical cap. We might expect to have a wide continuous spectrum of waves instead of a beam. In the frame of reference where the fluid is at rest, a propagating wave with wave vector $\vec{k}$ has a frequency $\omega = -k_x U_0$ which satisfies:

$$f < \omega < N \tag{5.1}$$

It follows that, for having propagating inertia gravity waves, $f/N < 1$ which is our case with $f/N = 0.4$ and in the non-rotating case with $f/N = 0$. In these cases we observe that λ_x increases as U_0 increases, and satisfy the dispersion relation:

$$k_x = \frac{\sqrt{N^2 \sin^2\theta + f^2 \cos^2\theta}}{U_0}, \tag{5.2}$$

this relation allows to compute the value of λ_x using the propagation angle θ obtained from the figure figure 5.3. These values for λ_x are registered in table 5.1 as function of the value of θ estimated from the figure.

Like in the non-rotating case, table 5.1 shows that the angle which the propagation vector makes with the vertical axis increases as the incoming mean flow velocity increases. It means that the wave-vector becomes closer to the horizontal mean flow. This table shows as well that θ increases with rotation. This behavior was described by [Redekopp, 1975], where he finds that the maximum slope of the group velocity decreases as f increases. In other words, rotation tends to make the waves propagation vector to be more horizontally

U_0 (cm/s)	$\frac{f}{N}$	Fr	θ (rad)	$k_x = \frac{\sqrt{N^2 \sin^2\theta + f^2 \cos^2\theta}}{U_0}$ $(\frac{1}{\text{cm}})$	$\lambda_x = \frac{2\pi}{k_x}$ (cm)
3	0.0	0.31	0.99	0.1337	46
3	0.4	0.31	1.20	0.1508	42
6	0.0	0.62	1.17	0.0736	85
6	0.4	0.62	1.27	0.0769	82
12	0.0	1.25	1.33	0.0388	161
12	0.4	1.25	1.34	0.0391	160

Table 5.1: Horizontal wavelength and angle with respect to the vertical of the propagating lee wave.

than the waves which propagate in a non-rotating system.

5.3.2 Comparison with the laboratory experiments

5.3.2.1 Comparison of the preferred wavelength between the PIV experiments, numerical simulations and linear theory

In order to measure the horizontal wavelength of the preferred wave vector, the streamwise velocity deviation and the spanwise velocity deviation fields are displayed in figure 5.4(a). These curves correspond to the intersection of two cross-sections of the streamwise velocity deviation field (drawn with a black line): the vertical center plane and the horizontal plane at $z = 60$ cm above the bottom, so as to avoid the influence of the wake. The same intersection of cross-sections is considered for the spanwise velocity field (drawn with a blue line). This figure displays the results for the rotating system for the laboratory experiments, the three-dimensional numerical simulations and the linear theory (with dividing streamline) presented in chapter 3, for the three flow rates we consider.

All curves in figure 5.4 exhibit a set of oscillations after, in most cases, a pronounced minimum after the cap. The wavelength inferred from these oscillations, and measured after this pronounced minimum, is reported in table 5.2. To simplify comparisons between the systems with and without rotation, we include as well the values of the wavelength measured for the non-rotating system.

The lee wave wavelength is measured along the central axis in the streamwise direction with a good agreement between experimental, simulation and theoretical results. An increase in the wavelength is found when the flow rate increases due to a Doppler shift effect as explained in the non-rotating case. The wave amplitude also depends on the velocity in a non-trivial way, and it might be related to the effective size of the topography due to the dividing streamline height.

The wavelength obtained for $Fr = 0.31$ in the PIV experimental measurements is $\lambda^{\text{PIV}}_{3\ \text{cm/s}} = 38$ cm (see figure 5.4(a)). The wavelength obtained for $Fr = 0.31$ in the 3D numerical simulation is $\lambda^{\text{3DNHM}}_{3\ \text{cm/s}} = 50$ cm (see figure 5.4(b)), which represents a difference of

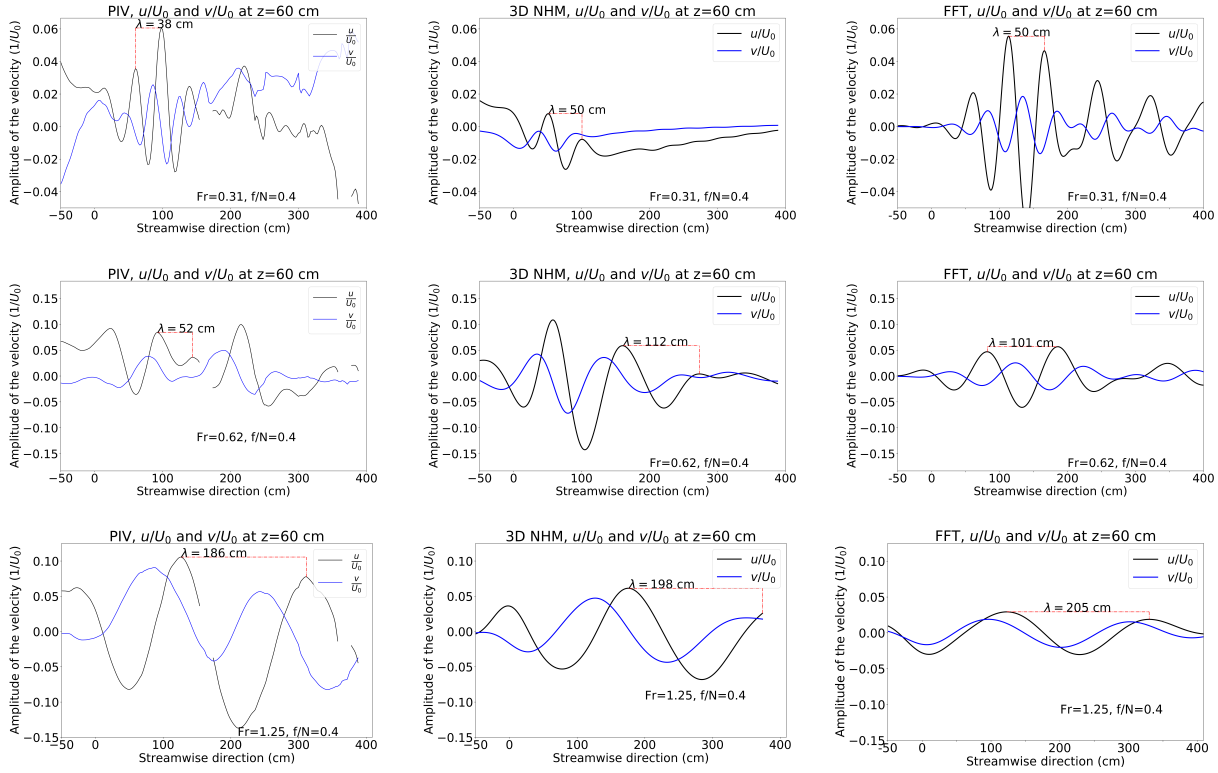

Figure 5.4: Horizontal wavelength measured at 60 cm above the bottom for the rotating case ($f/N = 0.4$) from three different approaches: PIV experiments in the first column, three-dimensional numerical simulations in the middle column and linear model with dividing streamline in the last column. Top row: $Fr = 0.31$, middle row: $Fr = 0.62$, bottom row: $Fr = 1.25$.

32% with the experimental value. In the same way, the wavelength obtained for $Fr = 0.31$ with the linear theory is also $\lambda_{0.31}^{\mathrm{LT+DSL}} = 50$ cm (see figure 3.10(b)), which also represents a difference of 32% with the experimental value. A very good agreement is observed in the wavelengths of the theoretical and numerical results for $Fr = 0.31$. In a similar way, for $Fr = 0.62$, the wavelengths found from the LT+DSL and the one found from the three dimensional numerical simulation are in a very good agreement, whereas the wavelength found from the PIV measurements is only a half of the ones found from the numerical methods. These differences, might be related to the fact that the wave beam has been reflected in the free surface of the water. Thus, the measured wavelength in the PIV measurements, corresponds to the superposition of the reflected and originally emitted wave beams whereas the measured wavelength in the numerical cases correspond only to the emitted wave beam.

By comparing the obtained wavelengths in the rotating and non rotating case, reported in table 5.2, we observe that the numerically obtained wavelengths increase when we consider rotation. As previously observed for the non-rotating system, in the rotating-system, the preferred wavelength increases as Fr increases.

U_0 (cm/s)	Fr	f/N	PIV (cm)	NHM 3D (cm)	Linear theory (cm)
3	0.31	0	50	41	41
3	0.31	0.4	38	50	50
6	0.62	0	78	94	81
6	0.62	0.4	52	112	101
12	1.25	0	162	179	164
12	1.25	0.4	186	198	205

Table 5.2: Comparative table of the wavelength of the lee wave field produced in a non-rotating system with the one obtained for a rotating system with $f/N = 0.4$.

5.3.2.2 Horizontal structure of the wave field

In order to explore the horizontal structure of the wave field, a horizontal cross-section of the divergence of the streamwise velocity field at $z = 60$ cm from the bottom is shown in figure 5.5. Just like for the non-rotating case, the horizontal cut of the waves for $Fr = 0.62$ and $Fr = 1.25$, shows a defined wave pattern. But while for $Fr = 0.31$, for the non-rotating case, a perfectly defined wave pattern was observed, for both: the numerical simulation and the experimental measurements, for the rotating case, in the numerical case, the wake effect is observed together with the wave field, which perturbs the wave structure, making only three maximums distinguishable on the right of the physical domain (the upper part of the frame).

Now, while the wave patterns for the non-rotating case were perfectly symmetric, the wave patterns for the rotating case are not longer symmetric with respect to the central-streamwise axis. For the rotating case, as the flow speed increases, the asymmetry becomes less important as observed for $Fr = 1.25$.

5.3.3 Momentum flux associated with the lee waves

Among the main objectives of the present PhD work stands the comparison of the momentum flux transported away by the propagating waves and that transferred to the wake. The momentum flux transported by the waves is computed in the present section using equation (4.5), for the one we add the volume term: $< vf >= \int fvdxdydz$. This momentum is computed as a function of the Froude number for the rotating system ($f/N = 0.4$) and compared to the one transferred to the waves for the non-rotating system. Just like in the non rotating case, a section is devoted to the moment transferred to wake in section 5.4.3.

We recall that, in three dimensions, the expression of the horizontal momentum transported vertically by the waves is (per unit mass) $< \vec{u'}w' >= (< u'w' >, < v'w' >)$ where the brackets refer to a spatial integral over a horizontal surface encompassing the wave region (we recall that as the waves are not steady a time average over 4 inertial periods is done). The two components of this flux have been computed above the cap, at $z = 23$ cm. For the same horizontal surface as in the non-rotating system: $[-d, 3d]$ along the $x-$direction,

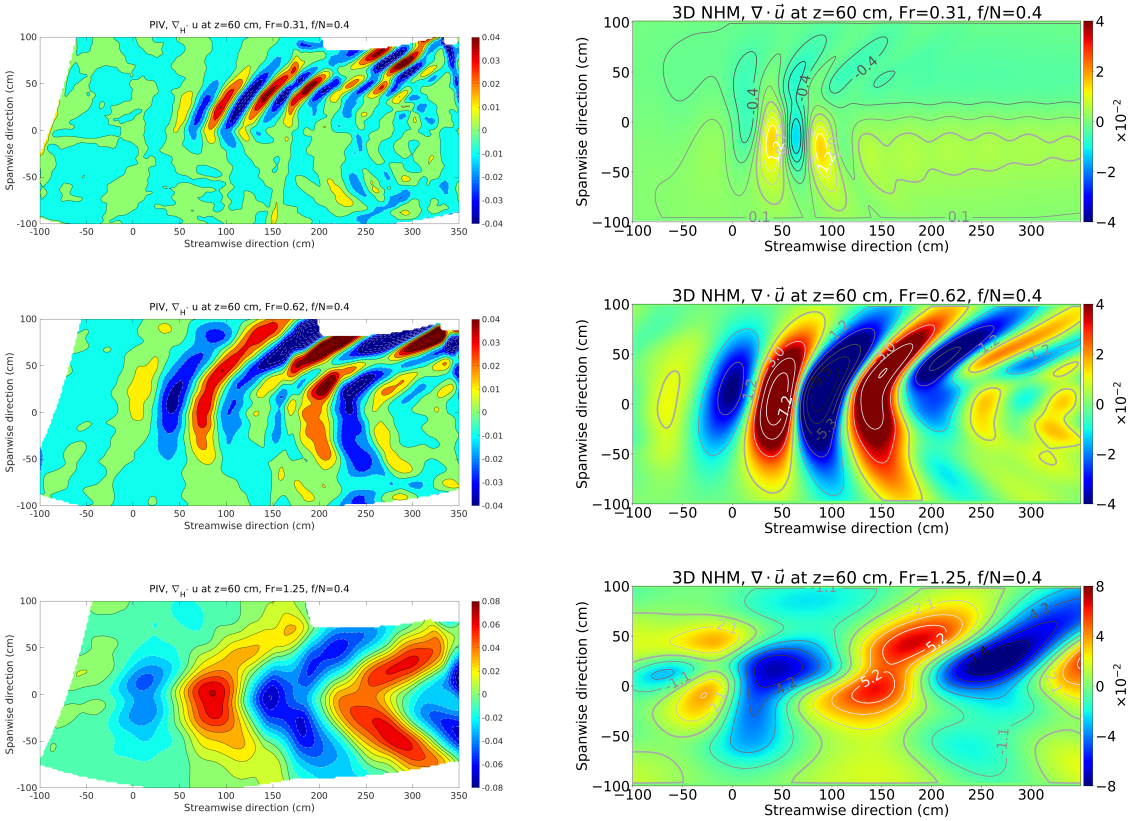

Figure 5.5: Horizontal cross-section at 60 cm above the bottom of the of the divergence of the velocity field for $f/N = 0.4$ with $Fr = 0.31$ $f/N = 0.4$ in the first row, $Fr = 0.62$ in the second row and $Fr = 1.25$ in the third row. On the left hand side the experimental PIV results, and on the right hand side the results from the three-dimensional numerical simulations. Each field is averaged in time over $[40, 60]$ buoyancy periods for $Fr = 0.31$, over $[30, 50]$ buoyancy periods for $Fr = 0.62$ and over $[20, 47]$ buoyancy periods for $Fr = 1.25$.

where d is the horizontal size of the cap at the bottom of the domain and $[-100, 100]$ cm in the $y-$direction. In the non-rotating configuration, the component $< vw >$ is much smaller than $< u'w' >$, due to the symmetry of v in a horizontal plane, nevertheless, in the rotating system is no longer the case, so both fluxes are considered here. These integrated fluxes computed at a given time during the steady regime are reported in table 5.3 for the three flow rates we consider, for the linear model and the three-dimensional simulation. The fluxes are scaled by U_0^2 to allow for comparison between the three cases. Table 4.3 shows that, for $Fr = 0.31$, the value of $< u'w'/U_0^2 >$ is similar for the numerical and linear models.

Fr	f/N	Linear theory		3D NHM	
		$< u'w' >$	$< v'w' >$	$< u'w' >$	$< v'w' >$
0.31	0.0	-103	0.0625	-24.55	0.02
0.31	0.4	-97	42.96	1.85	41.13
0.62	0.0	-177	0.530	-185.28	-0.22
0.62	0.4	-167	111.11	-187.51	30.61
1.25	0.0	-72	1.7009	-109.31	-0.05
1.25	0.4	-186	95	-153.14	19.22

Table 5.3: Computation of the normalized vertical transport of horizontal momentum by the wave field $\langle u'w' \rangle / U_0^2$ (in cm^2) integrated horizontally over the whole numerical domain at 23 cm above the bottom, by the linear model and the three-dimensional numerical model. The flux computed by the linear model does not vary along vertical because the background flow and the buoyancy frequency are constant.

The interpretation of this momentum is usually done through the introduction of a drag coefficient. The momentum transported by the waves is indeed associated with a drag force at the surface, exerted by the topography on the fluid. This drag force is usually characterized by a drag coefficient C_D defined by equation (4.3), where S is the section of the obstacle facing the flow. In the present case, this section is that of the cap over the height of the dividing streamline. Its expression is $S = \frac{1}{2}R^2\left(\alpha - \sin(\alpha)\right)$, with α defined by $\cos(\alpha/2) = \frac{h_s + h}{R}$, where R is the diameter of the sphere of which the cap is the upper part. In the present case, $R = 40$ cm. The corresponding drag coefficient values are registered in table 5.4.

For $Fr = 0.31$, using the value found numerically by the linear model for $< u'w' >$, $h_s = 13.8$ cm, we find $C_{D_{\text{waves}}} = 0.2707$. This is a very large value: in aerodynamic, the drag coefficient of a car for instance is of order 0.25. The part of the cap over the dividing streamline therefore exerts a very strong force on the flow.

This figure shows a comparison between linear theory (in red) and 3D numerical simulations (in blue) for the values of $C_{D_{\text{waves}}}$. On the left hand, the results are presented for the calculation without background rotation and on the right hand with rotation. For both the case with rotation and the case without rotation: the values of the drag coefficient obtained with the linear theory are similar to the ones obtained with the numerical simulation for

Fr	f/N	Linear theory	3D numerical model
0.31	0.0	1.1545	0.2707
0.31	0.4	1.0901	-0.0201
0.62	0.0	0.6950	0.7474
0.62	0.4	0.8378	0.7564
1.25	0.0	0.1465	0.3301
1.25	0.4	0.3785	0.3117

Table 5.4: Comparative table of the drag coefficients for the non rotating system and the rotating system with $f/N = 0.4$.

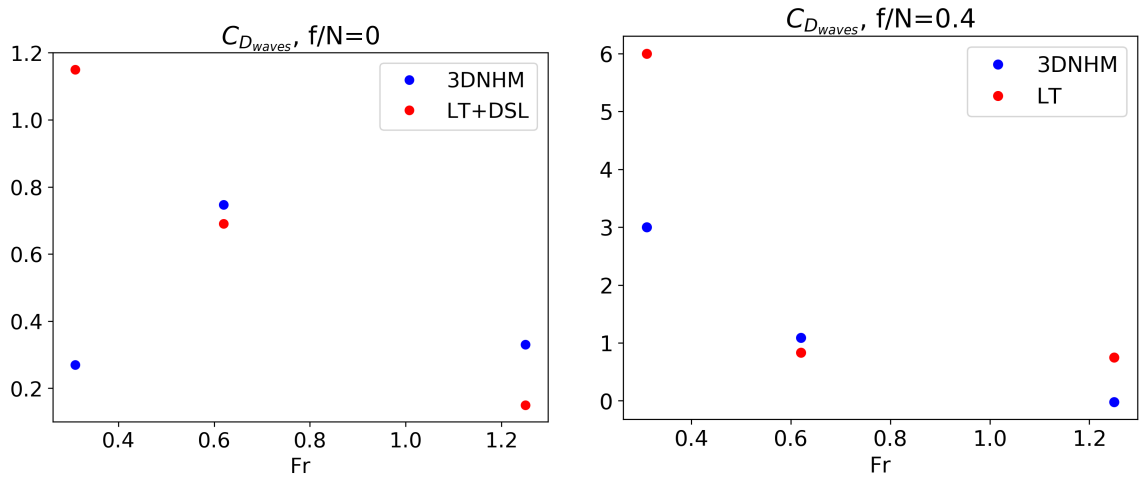

Figure 5.6: Drag coefficient induced by the waves $C_{D_{\text{waves}}}$ computed by the three-dimensional simulations (blue dots) and computed for the Linear theory taking into account the DSL (red dots) for $Fr = 0.31$, $Fr = 0.62$ and $Fr = 1.25$. On the left the results for $f/N = 0$, and on the right for $f/N = 0.4$

Fr=0.62 and for Fr=1.25, however they are very different for Fr=0.31. We observe, that while the linear theory shows that the wave induced drag coefficient is a decreasing function, the numerical simulation shows a maximum for Fr=0.61. If we take into account the figure mismatch, in which a maximum is observed experimentally and theoretically for configurations without background rotation, we can conclude that LT does not provide a description of the momentum transported by waves for small Fr as good as the numerical simulation. Thus, we can claim that the drag coefficient induced by the waves has a similar behavior with and without rotation.

Now, as the wave amplitude increases with the Froude number, we might expect that the drag coefficient associated with waves production should increase as the Froude number increases, but this is not the case. We find that the wave induced drag coefficient seems to reach a maximum value for a Froude number, Fr, such that $Fr \lesssim 1$, as we explained in the previous chapter. In other words, this behavior in the drag force associated to the wave emission, seems to be linked to the fact that there is too much kinetic energy that might be used to produce waves but the effective surface of the sphere is not enough to produce

them as it was theoretically described by [Greenslade, 2000].

5.3.4 Computation of the energy flux

The energy flux associated with the energy transport by the waves is defined by $\overline{p'w}$ where p' is the dynamical pressure (and the $\overline{\ }$ refers again to a spatial average). As in the previous section, we computed this flux at 23 cm above the ground and averaged over the same horizontal plane. The energy flux normalized by U_0^3 is displayed in table 5.5 for the three flow rates we consider.

Fr	f/N	$\frac{<p'w'>_{xy}}{U_0^3}$ (cm^2)
0.31	0	18
0.62	0	240
1.25	0	154
0.31	0.4	11
0.62	0.4	127
1.25	0.4	132

Table 5.5: Comparison of the vertical energy flux $\langle p'w' \rangle_{xy}$ normalized by U_0^3 computed by the three-dimensional simulations for $Fr = 0.31$, $Fr = 0.62$ and $Fr = 1.25$, at 23 cm above the bottom for the rotating and non-rotating systems. The flux is integrated horizontally over the surface $[-d, 3d]$ x $[-d, d]$ along the $x-$ and $y-$ directions, respectively.

Just as in the non-rotational case, when comparing the scaled energy transport with the momentum transport, by U_0^3 and U_0^3, respectively. We find a good agreement between tables 5.5 and 5.3. With exception of Fr=0.62 for f/N=0 and Fr=1.25 for f/N=0.4, which differ by a 50%. As in the non-rotating case, we analyze the fact that we find a preferred well-defined wavelength. To do so, we compute the spectrum along the $x-$direction of the wave-induced energy flux, $\overline{\Re(\hat{p'}\hat{w^*})}$, where the $\hat{}$ and * symbols denote the Fourier transform and the complex conjugate, respectively, and $\Re$ stands for the real part. The idea behind this computation is to investigate whether this preferred wavelength would not be that for which the wave-induced energy flux has a maximum value.

Figure 5.7 displays $\overline{\Re(\hat{p'}\hat{w^*})}$ as a function of the horizontal wavenumber k_x, using linear and logarithmic coordinates. It clearly appears that the wave-induced energy flux has a maximum value for a wavelength equal to 44 cm, which does match the value of the preferred wavelength found above. This preferred wavelength is therefore the scale at which the wave-induced energy flux is maximum, just as in the non-rotating case.

5.4 Analysis of the wake field

In chapter 3 it was stated that, due to the conservation of energy, a density stratified fluid which encounters an obstacle is divided into two different regions by a DSL. Above the DSL,

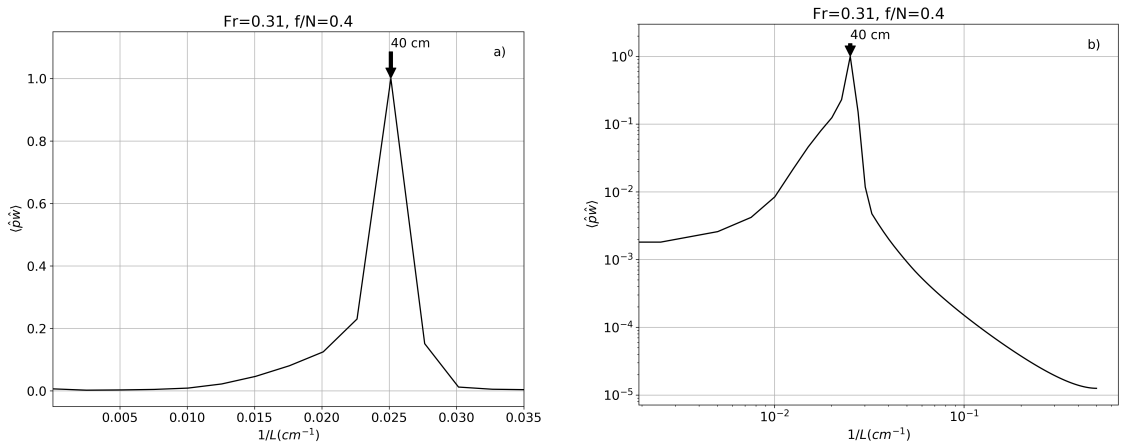

Figure 5.7: Fourier transform along the $x-$direction of the wave-induced energy flux $\overline{\hat{p}'\hat{w}^*}$ as a function of the horizontal wave number k_x (a) lin-lin plot, (b) log-log plot. The computation has been performed at $t = 30$ buoyancy periods (during the steady regime), for $z = 40$ cm and using an average over the horizontal $y-$direction and over -150 cm $\leq x \leq d$.

fluid particles with enough kinetic energy to rise above the topography would produce IGW. While the fluid parcels below the DSL that do not have enough kinetic energy to rise over it, would follow a quasi-horizontal path around the topography, with no IGW generation. Just as in the non-rotating case, for low values of Fr, the lower part of the flow is dominated by the turbulent wake, that is, the flow goes around the obstacle and not above it.

The behavior exhibited above the DSL was explored in the previous sections. In this section, the interest is focused on the processes below the DSL, near the bottom of the domain. In this region, the flow that goes around the cap leads to the formation of a wake behind the cap mainly composed of shedding vortices.

5.4.1 Vertical structure of the wake field

A preliminary view of the wake structure was displayed in figure 5.1. However, since we chose the color scale to show the wave field, it was not well suited to represent the wake field. To better observe the turbulent behavior of the flow, this figure was re-produced with an appropriate color scale. The corresponding frames for the non-rotating system were included in this figure to simplify their comparison, see figure 5.8. The wake is displayed here in the range of colors from blue to orange.

When comparing with the non-rotating system, for the same Froude numbers, a weaker wake is observed for the rotating system. No recirculation zone exists for the rotating system, whereas it was present for $Fr < 1$ in the non-rotating one. We observe as well that as Fr increases, the wake amplitude decreases. It means that the wake amplitude decreases with rotation, and also decreases as Fr increases.

In the first four rows of this figure, the ones corresponding to $Fr < 1$, we observe that the portion covered by the wake along the vertical direction is larger than the one covered by the wake in the non-rotating case. This figure shows that the wake effect stills relevant at 3

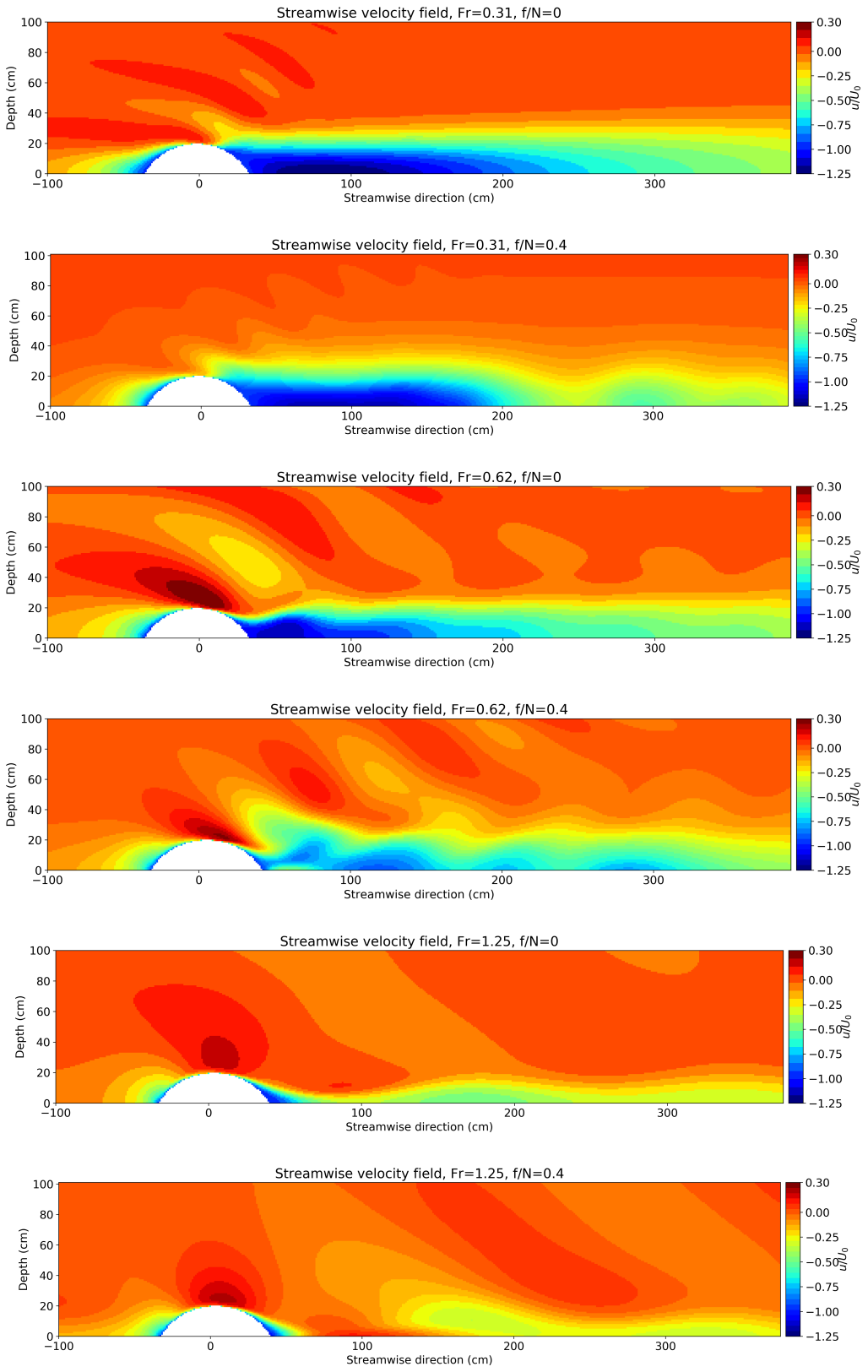

Figure 5.8: Cross-section of the streamwise velocity deviation in the vertical center plane for the non-rotating system in the odd-rows and for the rotating system, $f/N = 0.4$, in the even rows. The minimum value of u/U_0 is about -26.7% for $Fr = 0.31$, $f/N = 0.0$; for $Fr = 0.31$, $f/N = 0.0$ is about -3%; for $Fr = 0.62$, $f/N = 0.0$ is about -15%; for $Fr = 0.62$, $f/N = 0.4$ is about 0%; it is close to 0% for $Fr = 1.25$, $f/N = 0.0$; and for $Fr = 1.25$, $f/N = 0.4$ is about 3%. Thus the wake amplitude decreases as Fr increases.

topographic heights, while for the non-rotating system, its amplitude was already negligible at 2 topography heights. On the other hand, for the rotating system, the wake is no longer steady but is composed of shedding vortices which move away from the topography. These vortices can be seen in this figure as blue-yellow structures as the ones seen at 300 cm for $Fr < 1$. Even if the dividing streamline's height for $Fr = 1.25$ does not predict the existence of a turbulent wake, there is a few centimeters zero flow zone just after the topography for this Froude number.

5.4.2 Analysis of the blocking effect

In the previous subsection, we discussed the vertical structure of the wake. In this subsection, the discussion focuses on its horizontal structure at the bottom of the domain. To do so, we quantify the blocking effect, which leads to the wake. We take a horizontal cross-section of the streamwise velocity deviation normalized with the incoming flow at 1 cm above the bottom of the domain. This field is represented in figure 5.9 for both: the non-rotating (in the left column) and the rotating (in the right column) cases. These figures are disposed from top to bottom for $Fr = 0.31$, $Fr = 0.62$ and $Fr = 1.25$.

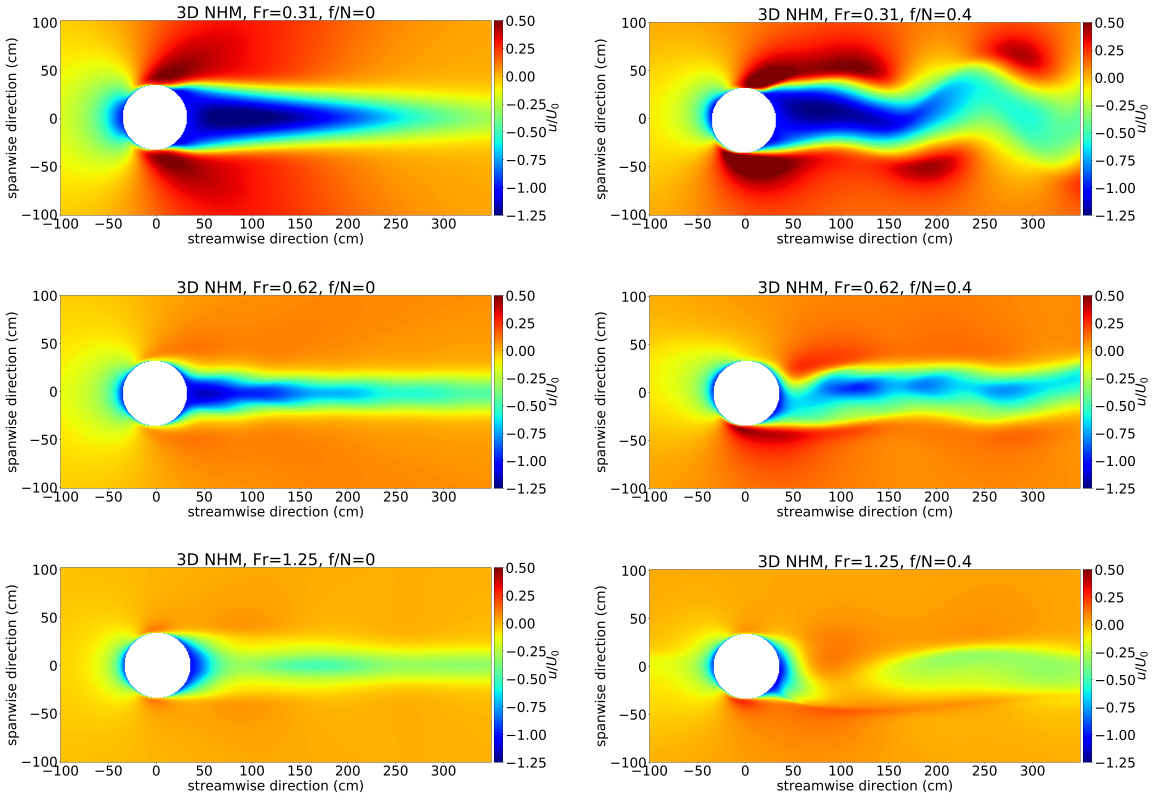

Figure 5.9: Horizontal cross-section of the streamwise velocity deviation field normalized with the incoming flow showing the blocking of the flow at 1 cm above the bottom of the domain. The frames on the left hand side correspond to the non-rotating system, and ones on the right correspond to the rotating system; for $Fr = 0.31$ at the top, $Fr = 0.62$ in the middle and $Fr = 1.25$ at the bottom row.

As in the non-rotating case, there is a flow deficit along the center streamwise axis. Due to momentum conservation, the flow rate increases on the sides of the topography for all the considered Froude numbers. Due to rotation, this over-flow is no longer symmetric, for instance, for $Fr < 1$ oscillates with the vortex shedding while for $Fr = 1.25$ the flow rate on the right of the topography is bigger than on the left side.

Just like the non-rotating case, the rotating case figure for $Fr = 0.31$ shows a strong blocking effect behind the topography, which even produces a recirculation zone behind the topography. Along the center-axis, the wake extends far away from the obstacle. In the rotating case, the wake structure exhibits a flapping effect, which breaks it into alternatively rotating vortices. This vortex shedding occurs at 3 topographic diameters, with a flow deficit factor being around 80%. At 4 topographic diameters, in the rotating case, the flow deficit oscillates between 50% and 60%, even at distances larger than 6 topographic diameters, unlike the non-rotating case, in which fluctuations are negligible.

While in the non-rotating case, the wake for $Fr = 0.31$ behaves like the wake for $Fr = 0.61$; in the rotating case, the wake behaves differently. The blocking effect gets fully dominated by the alternating dynamics of the vortex shedding. In this case, the detaching of the wake occurs near the topographic edge. Regarding the blocking effect factor, for the rotating system, it remains around 70% along the center axis even at 5 topographic diameters while for the non-rotating case decays to 50% at 3 topographic diameters away from the topography.

While for $Fr < 1$, vortex shedding is observed, there is no vortex evidence for $Fr > 1$. Nevertheless, when comparing with the non-rotating case, the flow deficit structure is no longer symmetric because of rotation, which also breaks down the wave symmetry. Apart from this asymmetry, for $Fr > 1$, we do not observe differences in the blocking factor when comparing the rotating and non-rotating systems.

5.4.2.1 Comparison with the laboratory experiments

In order to characterize the quasi-horizontal flow in the bottom part of the physical domain, the vertical vorticity component is displayed in figure 5.10 for the three flow rates we consider, for the experimental measurements and the numerical simulations.

The vertical vorticity $\vec{\Omega}_z$ is computed and shown in figure 5.10 for the rotating system with $f/N = 0.4$. In this figure, the vertical vorticity for the numerical simulations (on the right hand side) is compared with the computed vertical vorticity for the PIV experimental measurements (on the left hand side) for each of the Fr numbers here considered. The frames are organized as follows: in the first row the results for $Fr = 0.31$ are displayed, in the middle for $Fr = 0.62$, and at the bottom for $Fr = 1.25$.

In this figure, the flow goes from left to right, then, just like in the non-rotating case, when the fluid goes around the topography, in the rotating case, the current is split in two. The flow that goes on the right of the topography produces a counter-clockwise-rotating current, associated to a positive vorticity, and the flow on the left, produces a clockwise

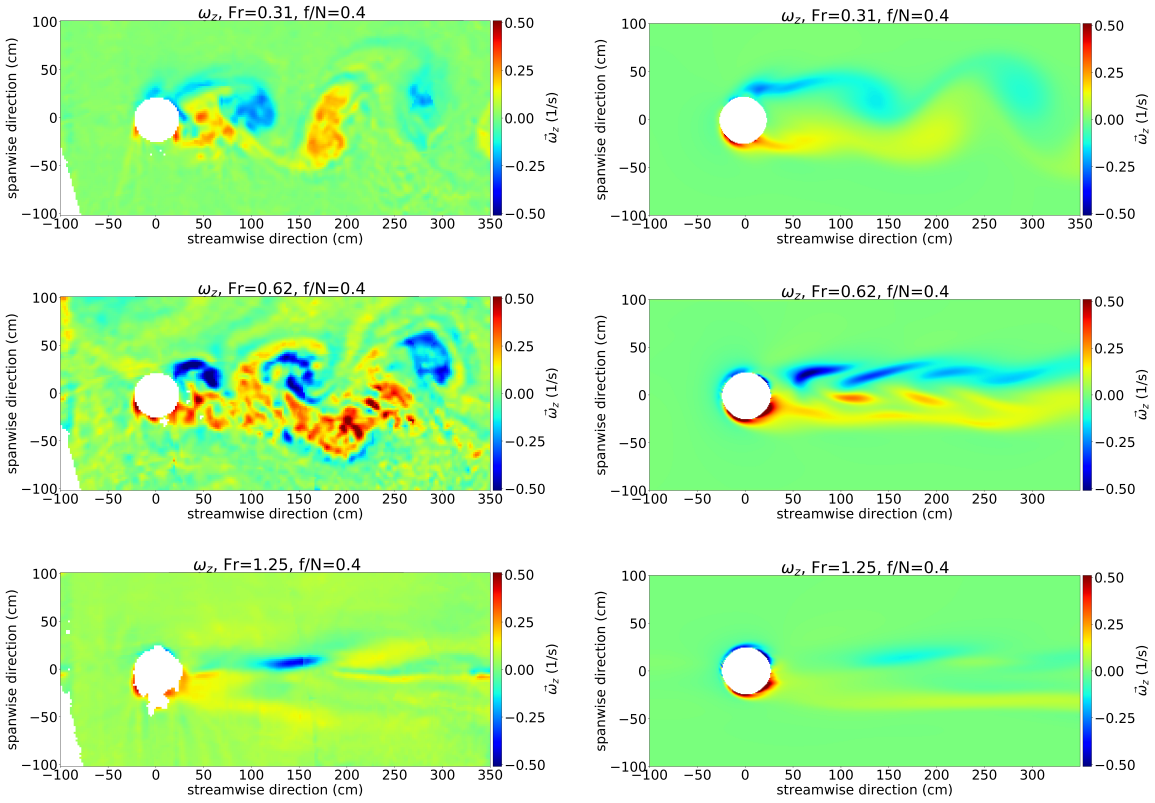

Figure 5.10: Vertical vorticity field computed at 12 cm above the domain's bottom. Comparison between PIV results (in the left column) and the 3D-NHM (in the right column) for $Fr = 0.31$ in the first row, for $Fr = 0.62$ in the second row and for $Fr = 1.25$ in the third row.

current with a negative vorticity. Unlike the non-rotating system, where the blocking of the lower part of the fluid results in a wake laterally delimited by two bands of opposite vorticity, counter rotating alternated vortices (positive and negative vorticity vortices) are ejected away from the topography, as shown in figure 5.10.

As in the non-rotating system, for $Fr < 1$, the magnitude of the vorticity increases with Fr, the maximum values being reached around the cap in the numerical simulations where the streamlines get closer (we remind that no boundary layer forms on the cap in the simulation due to the free-slip boundary condition). Despite the horizontal cross-section of the cap resembles that of a horizontal cylinder, the analogy with the wake developing behind a cylinder should be considered cautiously. Indeed, the critical Reynolds number for the wake behind a cylinder to become unstable (without rotation) and lead to the formation of symmetric counter-rotating vortices is about 40 [Kovasznay, 1949b], but in our case with no rotation, the wake is fairly straight, with no vortex shedding that would result from an unstable behavior. This critical value seems to be much higher for the cap obstacle we consider in the present study since the wake remains stable for $Re = 6000$.

The vortices produced behind the topographic obstacle produce vertical circulations at the bottom of the domain which are consistent with the ones observed in figure 5.3. One can conclude that a qualitatively good agreement is obtained between the laboratory

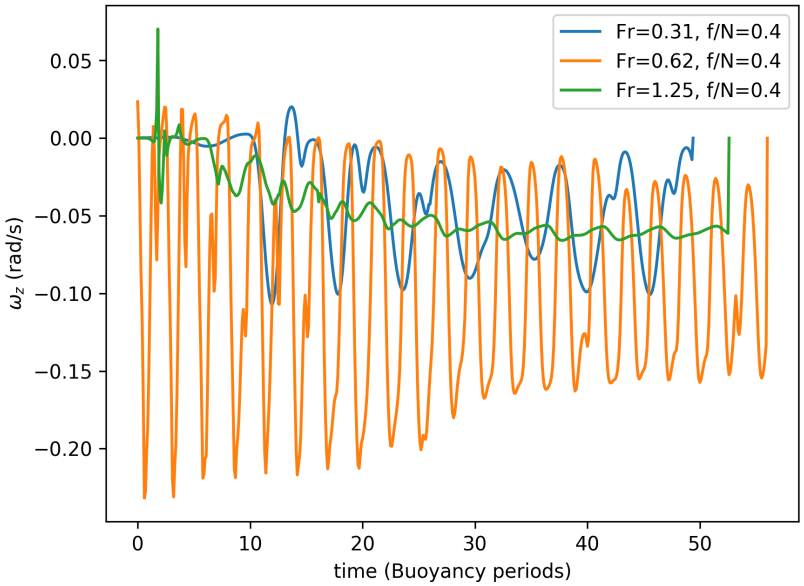

Figure 5.11: Impact of variation in U_0 in the vertical vorticity field.

experiments and the numerical simulations.

In order to quantify the vortex shedding frequency, the vertical vorticity is plotted as a function of time at $z = 12$ cm above the bottom at $x = 200$ cm downstream of the topography, and $y = 69$ cm on the right of the central streamwise axis for the three different Fr values. This plot is displayed in figure 5.11. This figure shows a periodic time evolution of vorticity field as a consequence of the vortex shedding, thus the oscillation frequency corresponds to the vortex shedding frequency f_{vortex}.

U_0 (cm/s)	Fr	f/N	Ro	f_{vortex} (b.p.$^{-1}$)	St
3	0.31	0.4	0.23	0.18	0.32
6	0.62	0.4	0.46	0.36	0.32
12	1.25	0.4	0.92	–	–

Table 5.6: Vortex shedding frequency f_{vortex}.

Table 5.6 summarizes the vortices shedding frequencies as a function of Fr and the Rossby number ($Ro = \frac{U_0}{fd}$). This table shows that for the explored interval $0.31 \geq Fr \geq 1.25$ ($0.33 \geq Ro \geq 0.87$), vortex shedding frequency depends linearly with Fr. But, the system does not show any vortex shedding for $Fr = 1.25$ ($Ro = 0.91$) as observed by [Sommeria et al., 2016].

In figure 5.10 a Karman vortex street is observed behind the topography [Von Kármán, 1963]. The frequency f_{vortex} at which the vortices are emitted away from the topography is usually characterized by the Strouhal number $St = \frac{f_{\text{vortex}} d}{U_0}$, where d is the sphere's diameter. The size of the vortices is comparable with the diameter of the topography and they are alternated. Thus, just like the non-rotating case, figure 5.10 shows the same behavior as an infinite cylinder with the same radius as the sphere's one at a height $h = 12$ cm above the

bottom. There is vortex shedding due to the influence of rotation. For $Fr < Ro$, shedding is controlled by stratification and for $Fr > Ro$, by rotation [Sommeria et al., 2016]. Also the shedding is observed only for $Fr < 0.4$ [Etling, 1990] but in [Ajayi, 2016] they got shedding for $Fr = 0.31$ and for $Fr = 0.62$ also. Nevertheless, a re-definition of the computed Froude number can be done, because topographic steepness is more important for linearity than height itself.

5.4.3 Change in the momentum flux due to the cap

The total flow deficit is due to two different sources, the wave emission and a blocking effect, which leads to a turbulent wake. Both of these effects damp-down the flow, i.e. the topographic obstacle induces a drag force on the flow [Durran, 2003]. The objective of the present section is to compute the change in the momentum flux due to the obstacle and to compare it to the momentum transported vertically by the waves, when the Froude number varies. The latter flux was computed in section 5.3.3. To do so, we consider the momentum conservation equation for the $x-$component integrated over the volume $\mathcal{V}$ comprising the obstacle and is enclosed by surface $\mathcal{S}$, using the divergence theorem for the volume $\mathcal{V}$. This volume is a rectangular prism with lower and upper boundaries the bottom of the domain ($z = 0$) and the horizontal plane located at $z = z_{top}$ with $z_{top} = 23$ cm, respectively. This volume extends along the $y-$direction from $y_l = -d$ to $y_r = d$ cm. Along the $x-$ direction, the left boundary of the volume is located at a position x_0 where the presence of the cap has no effect on the current, and we choose $x_0 = -2d$. The right boundary is located downstream the cap, at $x_1 = 3d$, with d the diameter at the base of the topography. The momentum budget (per unit mass) is given by section 4.3.3. From this equation, because of the size of the domain of integration, the contribution of $< p >_{x.y}$ can be neglected. As we already said, we are interested into compute only the contribution due to the wake which corresponds to the term D in this equation. Assuming that the contribution of VSS is negligible, we can estimate the value of D as.

$$D \approx - < uw >_{x.y} - < uv >_{x.z} - < u^2 >_{y.z} - f < v >_{x.y.z},$$

As previously stated, we are not interested in the drag force itself, but in the drag coefficient that is calculated $D = \frac{1}{2} C_{D_{\text{wake}}} S U_0^2$ and for the waves it was calculated in the 5.3.3. These coefficients are calculated as well as the total drag coefficient corresponding to the sum of these two coefficients and the three are recorded in the table 5.8 for the rotating and non-rotating systems.

We recall the definition for the total drag coefficient, explained in chapter 4, for a sphere in a stratified flow, given by $C_D = C_{D_{\text{waves}}} + C_{D_{\text{wake}}}$, where $C_{D_{\text{waves}}}$ is the waves induced drag coefficient, $C_{D_{\text{wake}}}$ is the wake induced drag coefficient. We register its value in table 5.8. In this table we included as well the drag coefficients obtained in chapter 4, to simplify the comparisons with the non-rotating system. We recall as well the definition of the horizontal

Fr	f/N	$\frac{\Delta\langle u^2\rangle_{yz}}{U_0^2}$	$\frac{\Delta\langle uv\rangle_{xz}}{U_0^2}$	$\frac{\Delta\langle uw\rangle_{xy}}{U_0^2}$	$\frac{f<v>_{xyz}}{U_0^2}$	$\frac{\langle w\rangle_{xy}}{U_0}$	$\frac{D}{U_0^2}$	$C_{D_{\text{total}}}$
0.31	0.00	-676.61244	-487.3504	12.6891	0	-100.6951	1251.9688	0.1797
0.62	0.00	-235.8714	-234.4729	-225.2732	0	-1121.7437	1817.3613	0.2307
1.25	0.00	0.7593	-7.7499	-107.5607	0	796.1311	-681.5799	0.1008
0.31	0.40	-632.0933	-582.1737	-9.7447	-1938.1123	-52.374	1276.3865	0.0607
0.62	0.40	-508.9495	-363.1289	-83.7754	-127.9458	-1340.4143	2296.2681	0.2336
1.25	0.40	-198.1236	-84.5680	-71.6249	16.0646	851.9128	-497.5964	0.1884

Table 5.7: Terms involved in the momentum budget of the $u-$component (see equation (4.7)), normalized by U_0^2. $\Delta\langle uw\rangle_{xy}/U_0^2$ refers to the first line, $\Delta\langle uv\rangle_{xz}/U_0^2$ to the second line, $\Delta\langle uw\rangle_{xy}/U_0^2$ to the third line, and $f<v>_{xyz}$ refers to the volume term associated to Ekman pumping. The 7th column is the horizontal average of w/U_0 on the top boundary of volume $\mathcal{V}$, the 8th column is the total drag force D normalized by U_0^2 defined by equation (4.7) and the last column is the total drag coefficient defined by (4.8).

Fr	Fr_{hor}	f/N	$C_{D_{\text{waves}}}$	$C_{D_{\text{total}}}$	$C_{D_{\text{wake}}}$
0.31	0.177	0.0	0.0104	0.1797	0.1692
0.62	0.354	0.0	0.1562	0.2307	0.0744
1.25	0.714	0.0	0.0963	0.1008	0.0044
0.31	0.177	0.4	0.0023	0.0607	0.0583
0.62	0.354	0.4	0.1211	0.2336	0.1125
1.25	0.714	0.4	0.1054	0.1884	0.0830

Table 5.8: Comparative table of the drag coefficients for the non rotating system and the rotating system with $f/N = 0.4$.

Froude number $Fr_{\text{hor}} = \frac{U_0}{Na_{\text{eff}}}$, where a_{eff} is the bottom radius of the topography which is involved in wave production, i.e. above the dividing streamline. As we consider a flat topography, we find that this horizontal Froude number can be computed simply by dividing the vertical Froude number Fr by $h_{\text{eff}}/a_{\text{eff}} = 1.75$, then, $Fr_{\text{hor}} = \frac{Fr}{1.75}$.

While in the case without rotation, we observed that the drag coefficient associated with the wake decreases with the Froude number, in the case with rotation is not the case. The drag coefficient induced by the wake behaves like the one induced by the wave. The drag coefficient associated with the waves and the one associated with the wake in the rotating case increase from $Fr = 0.31$ to $Fr = 0.62$ but then decrease from $Fr = 0.62$ to $Fr = 1.25$. As both drag coefficients behave like that, we observe the same behavior with the total drag coefficient.

Taking into account the induced drags by the wake and by the waves we can understand the existence of a local maximum for the drag coefficient. This local maximum is the result of a reinforcement between wave and wake drags. This reasoning also explains section 4.2.5, where a local maximum is systematically found around $Fr_{\text{hor}} = 0.35$, that is, our $Fr = 0.62$, where about half of the height of the topography is involved in active wave emission and

the other half produces the wake.

Now, when comparing the values of each of the drag coefficients associated with the waves for the non-rotating and rotating system, we do not find a clear tendency. We observe the same behavior with the drag coefficients associated with the wake, and therefore, with the total drag coefficients. We observe that as Fr increases, the difference between the total drag coefficient with and without rotation decreases, this means that impact of rotation becomes less important as the Fr increases. This is consistent with the results of [Bluemink et al., 2010], who did not find a relevant impact on the drag coefficient for a sphere when the solid body rotation of a non stratified fluid is considered. Please note that no stratification means $Fr = \infty$, but also, $Fr \to \infty$, when $U_0 \to \infty$ for a fixed non-zero N. So, based on [Bluemink et al., 2010] observations, we would no expect to have an important effect of rotation for large values of U_0, which is our case.

5.5 Sensibility study

5.5.1 Simulation parameters

In the previous sections, the results of numerical simulations are presented for three different flow rates: corresponding to the Froude numbers $Fr = 0.31$, $Fr = 0.62$ and $Fr = 1.25$ under the influence of rotation with a Coriolis parameter $f = 0.19$ s^{-1}. In order to have a better understanding of the impact of rotation on the wave and wake dynamics, five additional simulations were done for $Fr = 0.31$ keeping all the parameters constant but at different rotating rates. These simulations were run at a lower spatial resolution (Δx=Δy=Δz = 2 cm) for the same domain size. The considered rotating ratios correspond to the following Coriolis parameter values: $f = 0.05$ s^{-1}, $f = 0.10$ s^{-1}, $f = 0.15$ s^{-1}, $f = 0.25$ s^{-1} and $f = 0.40$ s^{-1}. As the stratification was kept constant ($N = 0.48$s^{-1}) into these simulations, the simulations were done for the following dimensionless ratios: $f/N = 0.1$, $f/N = 0.2$, $f/N = 0.3$, $f/N = 0.5$ and $f/N = 0.8$, respectively. We recall that in the previous sections we already presented results for $f/N = 0$ and $f/N = 0.4$. The vertical vorticity for $Fr = 0.31$ for these different rotation ratios is shown in figure 5.12. This figure shows that for $f/N = 0$ and $f/N = 0.1$, the wake oscillates perpendicularly to the flow direction. Nevertheless, these oscillations are not strong enough to produce vortex shedding. But when the Coriolis parameter is increased to $f/N = 0.2$ and so on, the vortex shedding appears, then vortices are ejected away from the topography.

5.5.2 Vortex shedding analysis

In order to quantify the vortices shedding frequency, the vertical vorticity is plotted as a function of time at $z = 12$ cm above the bottom, 200 cm downstream of the topography, and 50 cm on the right from the central streamwise axis. This plot is displayed in figure 5.13. This figure shows the periodic time evolution of the vorticity field as a consequence of an

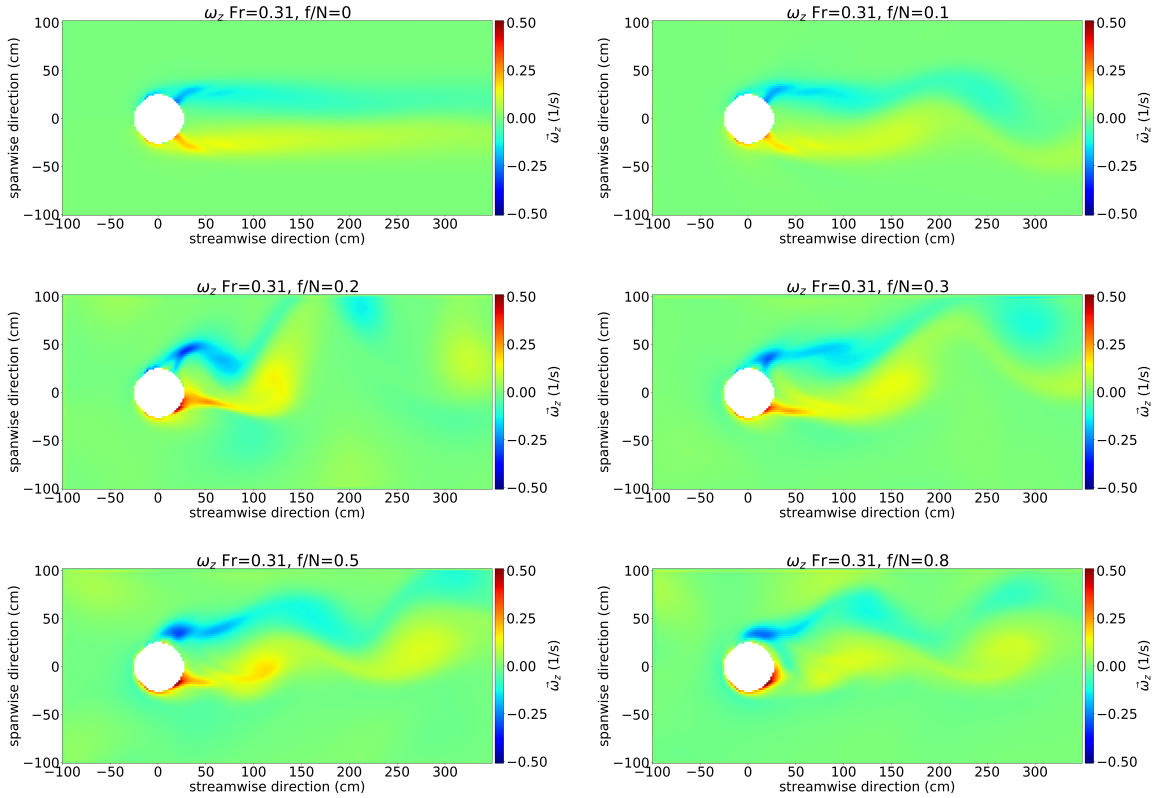

Figure 5.12: Horizontal cross-section of the vertical vorticity field at $z = 12$ cm for $Fr = 0.31$ at different rotation ratios. We show in the first line the results for $f/N = 0$, in the second one for $f/N = 0.1$, and so on up to $f/N = 0.8$ which is at the bottom.

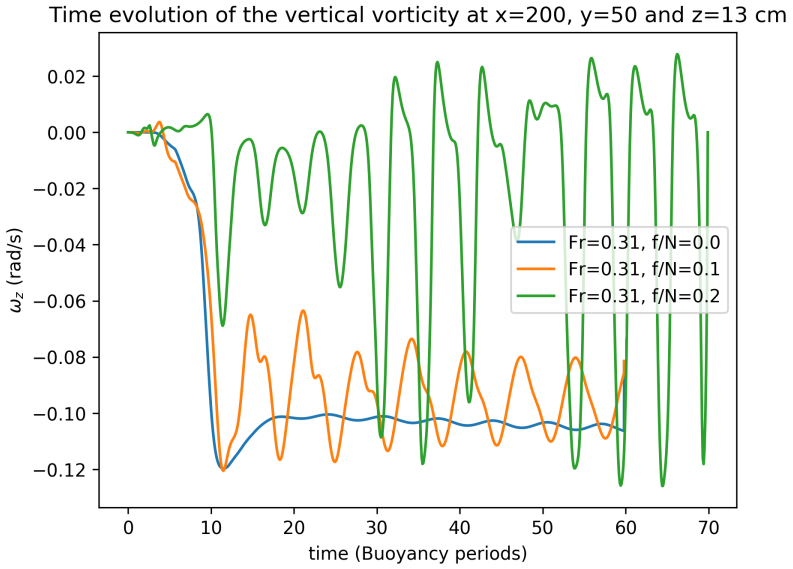

Figure 5.13: Temporal evolution of the vertical vorticity at $\vec{p} = (200, 50, 13)$ cm for different rotation rates.

oscillation in the wake structure seen in figure 5.12. The blue line in figure 5.13, corresponding to the non-rotating case, shows a small fluctuation around a negative value in the vorticity field. Similarly, the orange line, corresponding to $f/N = 0.1$ oscillates as well around a negative value, but its amplitude of oscillation is bigger than the observed for the non-rotating case. The green line, corresponding to $f/N = 0.2$, shows an oscillatory phenomenon that quickly increases in amplitude as the wake develops. After 35 buoyancy periods, the oscillations become so intense that they lead to a change in the sign of the vertical vorticity value. From that moment, the local vertical vorticity value continues changing of the sign leading finally to the vortex detachment at 55 buoyancy periods. The emitted vortices have a vortex shedding frequency $f_{\text{vortex}} = 0.18\ (b.p.)^{-1}$. The rotating cases with ratios corresponding to $f/N = 0.3$, $f/N = 0.5$, and $f/N = 0.8$ exhibit similar behavior to the one that exhibits the $f/N = 0.2$ with the same vortex shedding frequency. Thus, they are not included in this figure, but they are reported in table 5.9.

U_0 (cm/s)	Fr	f/N	Ro	f_{vortex} (b.p.$^{-1}$)	St
3	0.31	0.0	–	–	–
3	0.31	0.1	0.87	–	–
3	0.31	0.2	0.43	0.18	0.32
3	0.31	0.3	0.24	0.18	0.32
3	0.31	0.4	0.23	0.18	0.32
3	0.31	0.8	0.11	0.18	0.32

Table 5.9: Vortex shedding frequency f_{vortex}.

Table 5.9 summarizes the vortices shedding frequencies as a function of f/N and the Rossby number ($Ro = \frac{U_0}{fd}$). This table shows that for the explored interval $0.2 \geq f/N \geq 0.8$ ($0.11 \geq Ro \geq 0.87$), vortex shedding frequency does not seem to depend on the rotation ratio. But, the system does not show any vortex shedding for the non-rotating case neither for $f/N = 0.1$ ($Ro = 0.87$). Rotation seems to play an important role in the vortex shedding process, as we observed as f approaches to 0 no vortex shedding occurs, but f_{vortex} does not vary with f, it instead varies linearly with Fr.

5.6 Conclusions

One of the fundamental question in ocean dynamics is how the internal gravity waves generated by the mean flow over the oceanic topography transport momentum vertically, and what is their influence over the mean flow. In the intend to answer to this question, a set of experimental measurements were done by [Sommeria et al., 2016]. They did PIV over horizontal laser sheets and hence they could not quantify the vertical momentum flux. That is why, in the context of the experimental measurements done in Coriolis platform, we studied the topographic effects on the current. We modeled Coriolis rotating platform by

introducing a spherical cap as bottom topography. Numerical simulations were done with and without background rotation for different values of Froude numbers.

In this chapter, the results for the system presented in chapter 2, for the rotating system, are presented, described and analyzed. In order to simplify this analysis comparisons with the non-rotating system (reported in chapter 4) are done. As a reminder, the system rotates at a constant rate with Coriolis parameter $f = 0.19$ s^{-1}, and consists of a spherical cap topography in a fluid that is linearly stratified in density, $N = 0.48$ s^{-1}. Thus we consider the dimensionless ratio $f/N = 0.4$. This fluid flows over the topography at a constant flow rate of U_0. In this study we consider three different flow rates corresponding to three different values of Froude numbers: $Fr = 0.31$, $Fr = 0.62$ and $Fr = 1.25$. Additionally, for $Fr = 0.31$ we did an analysis of sensibility for different rotation rates corresponding to $f/N = 0.1$, 0.2, 0.3, 0.5 and 0.8.

The considered flow is modified by the interaction with the cap that leads to two different behaviors: an oscillating behavior (internal gravity waves+Inertial oscillations=inertia gravity waves) and a turbulent behavior (wake). The inertia gravity waves cover most of the physical domain and the wake is confined to the bottom of the physical domain. In this chapter we are interested in studying and quantifying the momentum transfers in the fluid due to this wave and the wake fields, as well as in characterizing these fields.

In order to analyze the system, it was treated from three different approaches: the experimental PIV measurements done by [Sommeria et al., 2016], three-dimensional numerical simulations and linear theory. As justified in chapter 3, the linear theory includes the DSL hypothesis, as it provides an important correction to the amplitude of the waves. The results are presented as a comparison with the experimental results, since it was this configuration that motivated this thesis.

Just as in the non-rotating case, the wave field has a preferred wavelength. We recall that through the boundary condition, the topography can be considered as a source of waves that emits waves with the spectrum of this topography. Since a spherical cap topography is considered, which has a continuous Fourier spectrum, we expect to observe a continuous spectrum of wavelengths that satisfy the dispersion relation. However, the wave field has a preferred wavelength for all Froude numbers. For the non-rotating system, this wavelength was set by the value U_0/N, as predicted by [Long, 1955]. Whereas for the rotating system, the value U_0/N sets the maximum value of the wavelength. For each Froude number, all wavelengths satisfy the dispersion relation. The measured wavelengths obtained from linear theory and the three dimensional numerical simulations are in good agreement for all the Froude numbers for the rotating and non-rotating system. The experimental measurements of the wavelength do not agree as well with the wavelengths obtained from linear theory and the numerical simulations for the rotating system as they were for the non-rotating system.

As in the non-rotating system, in the rotating system, the amplitude of the waves, which can be easily seen from the vertical component of the speed w, increases with the Froude number as well. In particular, the amplitude of the waves observed for $Fr = 0.62$ is

four times greater than the amplitude of the waves for $Fr = 0.31$. This can be explained qualitatively for the rotating and non-rotating systems from the boundary condition on the topography by using the dividing streamline hypothesis, which imposes the amplitude of w.

From the vertical plane, we observe that rotation modifies the preferred wave propagation angle, increasing the angle θ that the preferred wave vector makes with the vertical, which is consistent with our observations in chapter 3. We recall that at the end of this chapter we did a ray analysis using the theory of [Redekopp, 1975], who observed that as f/N increases the more horizontal becomes the wave vector. From the horizontal cross-section at $3h$, we observed that for the rotating case, the emitted lee waves are asymmetric with respect to the streamwise axis, whereas the emitted ones in the non-rotating system were symmetric.

Internal lee waves are emitted from the top part of the spherical cap while the bottom part makes the flow go around the cap creating a wake of eddies for the rotating case whereas it was a wake composed of two opposite vorticity bands in the non-rotating system. The dividing streamline height is given by $h_s = h(1 - Fr)$ where h is the height of the spherical cap. To characterize the wake, vertical vorticity is computed and the deficit of the horizontal velocity component, u', is studied.

For both, the rotating system and the non-rotating system, we observe that as the Froude number increases, the intensity and extension of the wake decreases. For example, $Fr = 0.31$, $f/N = 0$ there is an important recirculation zone. For $Fr = 0.62$, $f/N = 0$ the wake competes with the internal waves that shape the material surface of the wake. And for $Fr = 1.25$, the wake is barely visible and the back of the topography is dominated by internal waves. In a similar way for $Fr < 1$ with $f/N = 0.4$, we notice that the wake of eddies is clearly visible in the bottom part of the cap (below the dividing streamline). Whereas for $Fr = 1.25$ (dividing streamline height is below the cap height), no vortex behavior is observed. From our results we can conclude that no vortex shedding occurs for $Ro > 0.87$, and its frequency f_{vortex} increases linearly with Fr. This is in agreement with previous studies of stratified flow over an obstacle. Nevertheless a stationary turbulent wake with a zero flow speed confined to the very bottom of the domain is observed instead.

While for the non-rotating case, the lee wave field remains constant in the frame of reference where the topography is at rest, we observe inertial oscillations in the rotating case. These inertial oscillations are weak in amplitude, and their amplitudes do not grow in time, differently to reported for 2D-sinusoidal topography in which the amplitude increases with time due to resonant interactions [Nikurashin and Ferrari, 2010b] which lead to wave breaking. As we consider a flat topography, and in the absence of resonant interactions, the wave amplitude remains small, so we do not observe wave breaking. In the experimental setup an enhanced internal wave reflexion is observed in the water surface. This reflexions lead to breaking because of the non linear superposition of the reflected waves.

As one of the main objectives of this work is to quantify the momentum transfers in the fluid, we quantify the momentum transfer due to the waves and the wake. These transfers are studied through the wave drag coefficient $C_{D_{\text{waves}}}$ and the wake drag coefficient $C_{D_{\text{wake}}}$,

respectively. For $Fr < 1$ we observe that the drag induced by the wake increases with Fr. While, for $Fr > 1$ the induced drag by the wake is negligible as expected from [Voisin, 2007]. Now, as the wave amplitude increases with the Froude number, we might expect that the drag coefficient associated with waves production should increase as the Froude number increases, but this is not the case. We find that the wave induced drag coefficient seems to reach a maximum value for a Froude number, Fr, such that $Fr \lesssim 1$. In other words, this behavior in the drag force associated to the wave emission, seems to be linked to the fact that there is too much kinetic energy that might be used to produce waves but the effective surface of the sphere is not enough to produce them.

Taking into account the induced drags by the wake and by the waves we can understand the existence of a local maximum for the drag coefficient. This local maximum is the result of the combination of the wave and wake drags. One can find indeed that, there is a local maximum for the value of the drag coefficient around $Fr = 0.62$, where about half of the height of the topography is involved in active wave emission and the other half produces the wake.

We observe that as the Fr increases, the value of the drag coefficient associated with the wake decreases for the non-rotating and rotating case, and it tends to zero for $Fr > 1$. We observe the same behavior with the drag coefficients associated with the wave, and therefore, with the total drag coefficients. On the other hand, we do observe a non trivial tendency of the drag coefficients with rotation.

6

Conclusions

One of the fundamental questions in ocean dynamics is how the internal waves generated by the mean flow over the ocean topography, transport momentum vertically and influence the mean flow itself. In the intend to answer this question, a set of experimental measurements was done by [Sommeria et al., 2016]. They did PIV over horizontal laser layers and, hence they could not quantify the vertical momentum flux. That is why, in the context of the experimental measurements done in the Coriolis platform, we studied the topographic effects on the current. We modeled Coriolis rotating platform by introducing a spherical cap of height h as bottom topography. Numerical simulations were done with and without background rotation for different values of Froude numbers. The topography is submerged in a fluid that is linearly-stratified in density with buoyancy frequency N. This fluid flows over the topography at a constant flow rate of U_0. In this study we consider three different flow rates corresponding to three different values of Froude numbers, $Fr = \frac{U_0}{Nh}$: $Fr = 0.31$, $Fr = 0.62$ and $Fr = 1.25$.

Because of the chosen Froude numbers, the considered flow is modified by the interaction with the cap that leads to two different behaviors: an oscillating behavior and a turbulent behavior (wake), and they are divided by a dividing streamline (DSL). In the non-rotating system: this oscillating behavior consists of internal gravity waves, and the wake consists of two opposite sign vorticity bands. In the rotating system, the oscillating part consists of internal gravity waves and inertial oscillations, and the wake is composed of shedding vortices. In both of the cases, the oscillating behavior covers most of the physical domain, and the wake is confined to the bottom of the physical domain. In this thesis, we are interested in studying and quantifying the momentum transfers in the fluid due to this wave and the wake fields, characterizing these fields and understanding the role that plays rotation.

In order to analyze the system, three different approaches were studied: experimental PIV measurements, three-dimensional numerical simulations, and linear theory. The linear theory was presented in detail in chapter 3. The results of the numerical simulations for

the non-rotational system were described and analyzed in chapter 4. In this chapter, these simulations were compared with both: the experimental and the linear theory results. The numerical simulations for the rotating system were presented in chapter 5. In this chapter, the results were compared with the laboratory experiments and the linear theory for the rotating-system. As well, to have a better understanding of the impact of rotation, we made comparisons between the most important results for the non-rotating system with the rotating ones in chapter 5. In this chapter, we consider the system rotating at a constant rate with $f/N = 0.4$ for the three Froude numbers. Additionally to this rotating rate, we made an analysis of sensibility for $Fr = 0.31$ for different rotation ratios corresponding to $f/N = 0.1$, 0.2, 0.3, 0.5 and 0.8.

In chapter 3 the study of the system is done in the context of the linear theory, thus a study for the wave field with $Fr < 1$ is presented. In this chapter, the importance of the DSL is evaluated by comparing the numerical Fourier solution of the linear theory without (LT) and with the dividing streamline hypothesis (LT+DSL). From this comparison we conclude that the DSL hypothesis represents a considerable improvement to the model. Although LT predicts the wavelength correctly, it overestimates the amplitude of the waves. On the other hand, LT+DSL provides a good estimate for both. For this reason, we decided to study the system by including the DSL hypothesis in the linear theory. The study of the non-rotating system is complemented by the Bruno Voisin's analytic solution using LT+DSL in the far-field approximation. This approximation agrees well with the experimental results for distances of the order of 10 times $\frac{U_0}{N}$. At the end of this chapter, we computed the velocity field deviations for the system with rotation and we compared the results with the experimental ones.

The topography can be considered as a source of waves, that emits waves with the spectrum of this topography. Since we considered a spherical cap topography which has a continuous Fourier spectrum, we expected to observe a spectrum of wavelengths that satisfy the dispersion relation. However, we observed a preferred wavelength for the all the Froude numbers for the rotating and non-rotating systems. This preferred wavelength is set by the ratio U_0/N, which for $Fr < 1$ corresponds to the topographic size, just like as for a sinusoidal topography. For each Froude number, the wavelengths obtained by the different approaches agree well between them and satisfy the dispersion relation. In the case with rotation, the linear theory wavelengths agree, but not as well as in the non-rotational case. It is in part because it was difficult to select properly the maximums and minimums from the experimental results.

In chapter 3, we observed that the angle θ that the preferred wave vector makes with the vertical increases as Fr increases. For the rotating case, we observed that θ increases as f/N increases. We can conclude from here that the wave vector becomes more horizontal as either Fr or f increase.

For the non-rotating system, a horizontal cross-section of the wave field in the far field shows a parabolic profile. This profile becomes narrower as Fr increases. The same hori-

zontal cross-section for the rotating system, does not show a parabolic shape, in this case the emitted lee wave field is asymmetric with respect to the streamwise axis. This occurs because the rotation breaks the horizontal symmetry of the velocity. Due to the same cause, we observe that the $y-$component of the velocity is no longer zero in the rotating system whereas it is in the non-rotating one.

The amplitude of the waves, which can be easily seen from the vertical component of the speed w, increases as Fr increases. This can be explained qualitatively for the rotating and non-rotating systems from the boundary condition on the topography by using the dividing streamline hypothesis, which imposes the amplitude of $w \sim U_0 h_{\text{eff}}$. From this, we can conclude that including the DSL hypothesis predicts correctly the wave amplitude, and not including it implies an overestimation of the wave amplitude by a factor of $1/Fr$.

For both, the rotating system and the non-rotating system, we observe that as the Froude number increases, the intensity and extension of the wake decreases. For example, $Fr = 0.31$, $f/N = 0$ there is an important recirculation zone. For $Fr = 0.62$, $f/N = 0$ the wake competes with the internal waves that shape the material surface of the wake. And for $Fr = 1.25$, the wake is barely visible and the back of the topography is dominated by internal waves. In a similar way for $Fr < 1$ with $f/N = 0.4$, we notice that the wake of eddies is clearly visible in the bottom part of the cap (below the dividing streamline). Whereas for $Fr = 1.25$ (dividing streamline height is below the cap height), no vortex behavior is observed. From our results we can conclude that no vortex shedding occurs for $Ro > 0.87$, and its frequency f_{vortex} increases linearly with Fr. This is in agreement with previous studies of stratified flow over an obstacle. Nevertheless a stationary turbulent wake with a zero flow speed confined to the very bottom of the domain is observed instead.

While for the non-rotating case, the lee wave field remains constant in the frame of reference where the topography is at rest, we observe inertial oscillations in the rotating case. These inertial oscillations are weak in amplitude, and their amplitudes do not grow in time, differently to reported for 2D-sinusoidal topography in which the amplitude increases with time due to resonant interactions [Nikurashin and Ferrari, 2010b] which lead to wave breaking. As we consider a flat topography, and in the absence of resonant interactions, the wave amplitude remains small, so we do not observe wave breaking. In the experimental setup an enhanced internal wave reflexion is observed in the water surface. This reflexions lead to breaking because of the non linear superposition of the reflected waves.

As one of the main objectives of this work is to quantify the momentum transfers in the fluid, we quantify the momentum transfer due to the waves and the wake. These transfers are studied through the wave drag coefficient $C_{D_{\text{waves}}}$ and the wake drag coefficient $C_{D_{\text{wake}}}$, respectively. For $Fr < 1$ we observe that the drag induced by the wake increases with Fr. For $Fr > 1$ the induced drag by the wake is negligible as expected from [Voisin, 2007]. On the other hand, the drag induced by the waves increases as Fr increases for all the studied Froude numbers.

Now, as the wave amplitude increases with the Froude number, we might expect that

the drag coefficient associated with wave production should increase as the Froude number increases, but this is not the case. We find that the wave-induced drag coefficient seems to reach a maximum value for a Froude number, Fr, such that $Fr \lesssim 1$. In other words, this behavior in the drag force associated with the wave emission seems to be linked to the fact that there is too much kinetic energy that might be used to produce waves but, the effective surface of the sphere is not enough to produce them. Thus, a sort of wave saturation occurs in this case.

Taking into account the induced drags by the wake and by the waves we can understand the existence of a local maximum for the drag coefficient. This local maximum is the result of a good compromise between wave and wake drags. One can find indeed that, there is a local maximum for the value of the drag coefficient around $Fr = 0.62$, where about half of the height of the topography is involved in active wave emission and the other half produces the wake for both: the rotating and non-rotating systems.

Now, when comparing the values of each of the drag coefficients associated with the waves for the non-rotating and rotating system, we do not find an evident increase or decrease of the drag coefficients. While the total drag coefficient for $Fr = 0.31$ is smaller in the rotating case, we barely observe a difference for $Fr = 0.62$, and for $Fr = 1.25$ it is slightly lower in the rotating case. On the other hand, as the Fr increases, the asymmetries due to the effect of rotation seemed to decrease suggesting that the effect of rotation decreases as Fr increases. Nevertheless, further studies in this context are needed.

For $Fr < 1$, exists a region where both, a wake and a wave field co-exist. The co-existence of them produces a modification in the IGW field near the cap which is not well explained with linear theory. Nevertheless, in the far-field, this influence is no longer visible, leading to a good agreement with linear theory. For $Fr > 1$, we did not expect to see a wake, but we observe a very small zone where the flow behaves as a turbulent wake would behave. Even if the wake interacts with the wave field, stratification keeps the wake dynamics at the bottom of the physical domain, while the wave field is mainly present in the upper part of the physical domain.

Although there is overall good agreement between the results obtained with linear theory and experimental measurements, we observe an important difference in the first minimum that is not as intense in the LT+DSL solution as in the PIV results. This difference might be due to a non-linear process, induced by the upstream wake, but a more detailed study in this context is needed. On the other hand, the linear theory numerical study can also be used to obtain the velocity deviation fields by including the viscosity. The calculation of pressure and density can also be done as the calculation for velocity deviations was done.

Even if we observe a good agreement in the different approaches for the wave and wake fields, the interaction between them is not fully understood. The only qualitative observation can be done at the moment is that the wake seems to modify the effective topographic profile. This modified structure is much more complex than the dividing stream line hypothesis. It is necessary to perform more numerical simulations with better spatial resolution near the

topography as well as to consider a non-slip boundary condition.

In order to consider a more realistic configuration, with the ocean floor as a reference, [Sommeria et al., 2016] considered a configuration with multiple spheres. In this configuration the wave field produced above a cap superposes with the one produced at the surrounding caps enhancing the non linear wave-wave interactions that can lead to energy transfers across scales. Also, due to the proximity of the topographic obstacles, there is a strong interaction of the wake fields enhancing mixing on their own. A set of numerical simulations were carried out in this context, which were not included in this thesis document. However, a publication will be done in this context.

Numerical simulations and the Linear Theory Analysis showed that IGWs pattern for a 1 m depth layer is strong enough to deform the free surface of the water, thus an analysis of the waters surface in the Coriolis platform would be interesting in order to have an experiment to couple the bottom measurements with the deformed surface. This is interesting spatially because in ocean is easier to measure SSH than do ship measurements in ocean.

A

Appendix

A.1 Grid stretching

To have a better understanding of the grid-stretching the uniform vertical grid size definition is included below

```
   do k = KM0, KL, -1
      cz_w(k) = cz_w(k+1) - CELL_DZ
   end do

   do k = KKP0
     cz_p(k) = (cz_w(k)+cz_w(k+1))*0.5d0
   end do
```

Now, let's study the section of code that was used to impose the vertical grid-stretching. Two auxiliary variables are defined

```
#define CELL_DZ_SPONGE (5.0*CELL_DZ)
#define K_TRAN (KM-50)
```

Then the value of the top is established as was in the constant dz case

```
  cz_w(KM) = 0.0d0
```

Finally in the loop over all the $z - values$ the stretching function is introduced as an additive term to the constant `CELL_DZ`

```
  do k = KM0, KL, -1
     cz_w(k) = cz_w(k+1) - CELL_DZ  &
 &  -0.5*(CELL_DZ_SPONGE-CELL_DZ)(1+tanh((k-K_TRAN)/10.0))
  enddo

  do k = KKP0
```

```
    cz_p(k) = (cz_w(k)+cz_w(k+1))*0.5d0
enddo
```

Bibliography

[Aiki et al., 2006] Aiki, H., Takahashi, K., and Yamagata, T. (2006). The red sea outflow regulated by the indian monsoon. *Continental Shelf Research*, 26(12-13):1448–1468.

[Aiki and Yamagata, 2004] Aiki, H. and Yamagata, T. (2004). A numerical study on the successive formation of meddy-like lenses. *Journal of Geophysical Research: Oceans*, 109(C6).

[Ajayi, 2016] Ajayi, A. (2016). Laboratory Model of the Antarctic Circumpolar Current. Master's thesis, The Laboratoire des Écoulements Géophysiques et Industriels (LEGI), Grenoble, France.

[Arbic et al., 2018] Arbic, B. K., Alford, M. H., Ansong, J. K., Buijsman, M. C., Ciotti, R. B., Farrar, J. T., Hallberg, R. W., Henze, C. E., Hill, C. N., Luecke, C. A., et al. (2018). *Primer on Global Internal Tide and Internal Gravity Wave Continuum Modeling in HYCOM and MITgcm*. New frontiers in operational oceanography.

[Arfken and Weber, 2005] Arfken, G. B. and Weber, H. J. (2005). *Mathematical methods for physicists*. Elsevier, 6th edition.

[Baines, 1995] Baines, P. (1995). *Topographic effects in stratified flows*. Cambridge University Press.

[Baines and Hoinka, 1985] Baines, P. G. and Hoinka, K. P. (1985). Stratified flow over two-dimensional topography in fluid of infinite depth: a laboratory simulation. *Journal of the atmospheric sciences*, 42(15):1614–1630.

[Bluemink et al., 2010] Bluemink, J., Lohse, D., Prosperetti, A., and Van Wijngaarden, L. (2010). Drag and lift forces on particles in a rotating flow. *Journal of fluid mechanics*, 643:1.

[Boury et al., 2019] Boury, S., Peacock, T., and Odier, P. (2019). Excitation and resonant enhancement of axisymmetric internal wave modes. *Physical Review Fluids*, 4(3):034802.

[Brekhovskikh and Goncharov, 1993] Brekhovskikh, L. M. and Goncharov, V. (1993). *Mechanics of continua and wave dynamics*, volume 1. Springer-Verlag, second edition.

[Cheng, 1977] Cheng, H. (1977). On inertial wave and flow structure at low rossby number. *Zeitschrift für angewandte Mathematik und Physik ZAMP*, 28(5):753–770.

[Cheng and Johnson, 1982] Cheng, H. and Johnson, E. (1982). Inertial waves above an obstacle in an unbounded, rapidly rotating fluid. *Proceedings of the Royal Society of London. A. Mathematical and Physical Sciences*, 383(1784):71–87.

[Clark et al., 2002] Clark, P. U., Pisias, N. G., Stocker, T. F., and Weaver, A. J. (2002). The role of the thermohaline circulation in abrupt climate change. *Nature*, 415(6874):863–869.

[Clary et al., 2018] Clary, V., Oudart, T., Maître, T., Sommeria, J., Zeidan, W., Morocho, L., Makhour, A., Larroudé, P., Vandenberghe, T., Vignal, L., et al. (2018). A simple 3d river/tidal turbine model for farm computation–comparison with experiments.

[Couto et al., 2020] Couto, N., Alford, M. H., MacKinnon, J., and Mickett, J. B. (2020). Mixing rates and bottom drag in bering strait. *Journal of Physical Oceanography*, 50(3):809–825.

[Dalziel et al., 2011] Dalziel, S. B., Patterson, M. D., Caulfield, C., and Le Brun, S. (2011). The structure of low-froude-number lee waves over an isolated obstacle. *Journal of Fluid Mechanics*, 689:3–31.

[Dong and McWilliams, 2007] Dong, C. and McWilliams, J. C. (2007). A numerical study of island wakes in the southern california bight. *Continental Shelf Research*, 27(9):1233–1248.

[Dossmann et al., 2016a] Dossmann, Y., Bourget, B., Brouzet, C., Dauxois, T., Joubaud, S., and Odier, P. (2016a). Mixing by internal waves quantified using combined piv/plif technique. *Experiments in Fluids*, 57(8):132.

[Dossmann et al., 2016b] Dossmann, Y., G Rosevear, M., Griffiths, R. W., Hughes, G. O., Copeland, M., et al. (2016b). Experiments with mixing in stratified flow over a topographic ridge. *Journal of Geophysical Research: Oceans*, 121(9):6961–6977.

[Durran, 2003] Durran, D. R. (2003). Lee waves and mountain waves. *Encyclopedia of Atmospheric Sciences*, pages 1161–1170.

[Ermanyuk et al., 2017] Ermanyuk, E. V., Shmakova, N., and Flór, J.-B. (2017). Internal wave focusing by a horizontally oscillating torus. *Journal of Fluid Mechanics*, 813:695–715.

[Etling, 1990] Etling, D. (1990). Mesoscale vortex shedding from large islands: a comparison with laboratory experiments of rotating stratified flows. *Meteorology and Atmospheric Physics*, 43(1-4):145–151.

[Ferrari and Boccaletti, 2004] Ferrari, R. and Boccaletti, G. (2004). Eddy-mixed layer interactions in the ocean. *Oceanography*.

[Fortuin, 1960] Fortuin, J. (1960). Theory and application of two supplementary methods of constructing density gradient columns. *Journal of Polymer Science Part A: Polymer Chemistry*, 44(144):505–515.

[Greenslade, 2000] Greenslade, M. (2000). Drag on a sphere moving horizontally in a stratified fluid. *Journal of Fluid Mechanics*, 418:339–350.

[Greenslade, 1992] Greenslade, M. D. (1992). Strongly stratified airflow over and around mountains. *Stably Stratified Flows: Flow and Dispersion over Topography*, pages 25–37.

[Hanazaki, 1988] Hanazaki, H. (1988). A numerical study of three-dimensional stratified flow past a sphere. *Journal of Fluid Mechanics*, 192:393–419.

[Heikes and Maxworthy, 1982] Heikes, K. and Maxworthy, T. (1982). Observations of inertial waves in a homogeneous rotating fluid. *Journal of Fluid Mechanics*, 125:319–345.

[Hide et al., 1968] Hide, R., Ibbetson, A., and Lighthill, M. (1968). On slow transverse flow past obstacles in a rapidly rotating fluid. *Journal of Fluid Mechanics*, 32(2):251–272.

[Howell et al., 2012] Howell, E. A., Bograd, S. J., Morishige, C., Seki, M. P., and Polovina, J. J. (2012). On north pacific circulation and associated marine debris concentration. *Marine Pollution Bulletin*, 65(1-3):16–22.

[Hunt et al., 1997] Hunt, J., Feng, Y., Linden, P., Greenslande, M., and Mobbs, S. (1997). Low-froude-number stable flows past mountains. *Il nuovo cimento C*, 20(3):261–272.

[Hunt et al., 2006] Hunt, J., Vilenski, G., and Johnson, E. (2006). Stratified separated flow around a mountain with an inversion layer below the mountain top. *Journal of Fluid Mechanics*, 556:105–119.

[Johnson, 1982] Johnson, E. (1982). The effects of obstacle shape and viscosity in deep rotating flow over finite-height topography. *J Fluid Mech*, 120:359–383.

[Kovasznay, 1949a] Kovasznay, L. (1949a). Hot-wire investigation of the wake behind cylinders at low reynolds numbers. *Proceedings of the Royal Society of London. Series A. Mathematical and Physical Sciences*, 198(1053):174–190.

[Kovasznay, 1949b] Kovasznay, L. (1949b). Hot-wire investigation of the wake behind cylinders at low reynolds numbers. *Proceedings of the Royal Society of London. Series A. Mathematical and Physical Sciences*, 198(1053):174–190.

[Labreuche, 2015] Labreuche, P. (2015). *Ondes de relief dans l'océan profond: mélange diapycnal et interactions avec les oscillations inertielles*. PhD thesis, The Laboratoire des Écoulements Géophysiques et Industriels (LEGI), Grenoble, France.

[Landau and Lifshitz, 1986] Landau, L. and Lifshitz, E. (1986). *Curso de Fısica Teórica, Volumen 6: Mecánica de Fluidos*. Reverté.

[Landau and Lifshitz, 1970] Landau, L. D. and Lifshitz, E. M. (1970). *Mecánica*, volume 1. Reverté.

[Largeron et al., 2013] Largeron, Y., Staquet, C., and Chemel, C. (2013). Characterization of oscillatory motions in the stable atmosphere of a deep valley. *Boundary-layer meteorology*, 148(3):439–454.

[Leclair et al., 2019] Leclair, M., Raja, K., and Staquet, C. (2019). Nonlinear reflection of a two-dimensional finite-width internal gravity wave onto a slope.

[Lefauve et al., 2015] Lefauve, A., Muller, C., and Melet, A. (2015). A three-dimensional map of tidal dissipation over abyssal hills. *Journal of Geophysical Research: Oceans*, 120(7):4760–4777.

[Lighthill, 1978] Lighthill, J. (1978). *Waves in fluids*. Cambridge University Press.

[Lighthill, 1967] Lighthill, M. J. (1967). On waves generated in dispersive systems by travelling forcing effects, with applications to the dynamics of rotating fluids. *Journal of Fluid Mechanics*, 27(4):725âĂŞ752.

[Lighthill, 1970] Lighthill, M. J. (1970). The theory of trailing taylor columns. *Mathematical Proceedings of the Cambridge Philosophical Society*, 68(2):485âĂŞ491.

[Lofquist and Purtell, 1984] Lofquist, K. E. and Purtell, L. P. (1984). Drag on a sphere moving horizontally through a stratified liquid. *Journal of Fluid Mechanics*, 148:271–284.

[Long, 1955] Long, R. R. (1955). Some aspects of the flow of stratified fluids: Iii. continuous density gradients. *Tellus*, 7(3):341–357.

[Machicoane et al., 2018] Machicoane, N., Labarre, V., Voisin, B., Moisy, F., and Cortet, P.-P. (2018). Wake of inertial waves of a horizontal cylinder in horizontal translation. *Physical Review Fluids*, 3(3):034801.

[MacKinnon, 2013] MacKinnon, J. (2013). Oceanography: Mountain waves in the deep ocean. *Nature*, 501(7467):321–322.

[MacKinnon et al., 2017] MacKinnon, J. A., Zhao, Z., Whalen, C. B., Waterhouse, A. F., Trossman, D. S., Sun, O. M., St. Laurent, L. C., Simmons, H. L., Polzin, K., Pinkel, R., et al. (2017). Climate process team on internal wave–driven ocean mixing. *Bulletin of the American Meteorological Society*, 98(11):2429–2454.

[Mani, 2012] Mani, A. (2012). Analysis and optimization of numerical sponge layers as a nonreflective boundary treatment. *Journal of Computational Physics*, 231(2):704–716.

[Marshall et al., 1997] Marshall, J., Hill, C., Perelman, L., and Adcroft, A. (1997). Hydrostatic, quasi-hydrostatic, and nonhydrostatic ocean modeling. *Journal of Geophysical Research: Oceans*, 102(C3):5733–5752.

[Mason, 1977] Mason, P. (1977). Forces on spheres moving horizontally in a rotating stratified fluid. *Geophysical & Astrophysical Fluid Dynamics*, 8(1):137–154.

[Mason and Sykes, 1981] Mason, P. and Sykes, R. (1981). A numerical study of rapidly rotating flow over surface-mounted obstacles. *Journal of Fluid Mechanics*, 111:175–195.

[Maxworthy, 1977] Maxworthy, T. (1977). Topographic effects in rapidly-rotating fluids: flow over a transverse ridge. *Zeitschrift für angewandte Mathematik und Physik ZAMP*, 28(5):853–864.

[Mercier et al., 2011] Mercier, M. J., Vasseur, R., and Dauxois, T. (2011). Resurrecting dead-water phenomenon. *Nonlinear Processes in Geophysics*, 18(2):193–208.

[Munk and Wunsch, 1998] Munk, W. and Wunsch, C. (1998). Abyssal recipes ii: Energetics of tidal and wind mixing. *Deep-sea research. Part I, Oceanographic research papers*, 45(12):1977–2010.

[Naveira-Garabato et al., 2004] Naveira-Garabato, A. C., Polzin, K. L., King, B. A., Heywood, K. J., and Visbeck, M. (2004). Widespread intense turbulent mixing in the southern ocean. *Science*, 303(5655):210–213.

[Newley et al., 1991] Newley, T., Pearson, H., and Hunt, J. (1991). Stably stratified rotating flow through a group of obstacles. *Geophysical & Astrophysical Fluid Dynamics*, 58(1-4):147–171.

[Nikurashin and Ferrari, 2010a] Nikurashin, M. and Ferrari, R. (2010a). Radiation and dissipation of internal waves generated by geostrophic motions impinging on small-scale topography: Application to the southern ocean. *Journal of Physical Oceanography*, 40(9):2025–2042.

[Nikurashin and Ferrari, 2010b] Nikurashin, M. and Ferrari, R. (2010b). Radiation and dissipation of internal waves generated by geostrophic motions impinging on small-scale topography: Theory. *Journal of Physical Oceanography*, 40(5):1055–1074.

[Nikurashin et al., 2014] Nikurashin, M., Ferrari, R., Grisouard, N., and Polzin, K. (2014). The impact of finite-amplitude bottom topography on internal wave generation in the southern ocean. *Journal of Physical Oceanography*, 44(11):2938–2950.

[Nikurashin et al., 2013] Nikurashin, M., Vallis, G. K., and Adcroft, A. (2013). Routes to energy dissipation for geostrophic flows in the southern ocean. *Nature Geoscience*, 6(1):48.

[Perfect et al., 2020] Perfect, B., Kumar, N., and Riley, J. (2020). Energetics of seamount wakes. part i: Energy exchange. *Journal of Physical Oceanography*, 50(5):1365–1382.

[Polzin et al., 1997] Polzin, K., Toole, J., Ledwell, J., and Schmitt, R. (1997). Spatial variability of turbulent mixing in the abyssal ocean. *Science*, 276(5309):93–96.

[Polzin et al., 1995] Polzin, K. L., Toole, J. M., and Schmitt, R. W. (1995). Finescale parameterizations of turbulent dissipation. *Journal of physical oceanography*, 25(3):306–328.

[Redekopp, 1975] Redekopp, L. (1975). Wave patterns generated by disturbances travelling horizontally in rotating stratified fluids. *Geophysical and Astrophysical Fluid Dynamics*, 6(4):289–313.

[Reid et al., 1978] Reid, J. L., Brinton, E., Fleminger, A., Venrick, E. L., and McGowan, J. A. (1978). Ocean circulation and marine life. In *Advances in oceanography*, pages 65–130. Springer.

[Richet et al., 2018] Richet, O., Chomaz, J.-M., and Muller, C. (2018). Internal tide dissipation at topography: triadic resonant instability equatorward and evanescent waves poleward of the critical latitude. *Journal of Geophysical Research: Oceans*, 123(9):6136–6155.

[Roach et al., 1995] Roach, A., Aagaard, K., Pease, C., Salo, S., Weingartner, T., Pavlov, V., and Kulakov, M. (1995). Direct measurements of transport and water properties through the bering strait. *Journal of Geophysical Research: Oceans*, 100(C9):18443–18457.

[Sharman and Wurtele, 1983] Sharman, R. and Wurtele, M. (1983). Ship waves and lee waves. *Journal of the Atmospheric Sciences*, 40(2):396–427.

[Sheppard, 1956] Sheppard, P. (1956). Airflow over mountains. *Quarterly journal of the Royal Meteorological society*, 82(354):528–529.

[Shishkina, 1996] Shishkina, O. (1996). Comparison of the drag coefficients of bodies moving in liquids with various stratification profiles. *Fluid dynamics*, 31(4):484–489.

[Shriver et al., 2012] Shriver, J., Arbic, B. K., Richman, J., Ray, R., Metzger, E., Wallcraft, A., and Timko, P. (2012). An evaluation of the barotropic and internal tides in a high-resolution global ocean circulation model. *Journal of Geophysical Research: Oceans*, 117(C10).

[Smith, 1989] Smith, R. B. (1989). Hydrostatic airflow over mountains. In *Advances in geophysics*, volume 31, pages 1–41. Elsevier.

[Sommeria et al., 2016] Sommeria, J., Ajayi, A.-O., Raja, K. J., Staquet, C., Viboud, S., and Voisin, B. (2016). Laboratory modelling of momentum transport by internal gravity waves and eddies in the antarctic circumpolar current. In *VIIIth International Symposium on Stratified Flows*, volume 1.

[Staquet, 2005] Staquet, C. (2005). Internal gravity waves in geophysical fluids. *Environmental Stratified Flows*, 479:75–132.

[Stewartson and Cheng, 1979] Stewartson, K. and Cheng, H. (1979). On the structure of inertial waves produced by an obstacle in a deep, rotating container. *Journal of Fluid Mechanics*, 91(3):415–432.

[Struik, 1961] Struik, D. J. (1961). *Lectures on classical differential geometry*. Dover Publications.

[Sutherland and Linden, 2002] Sutherland, B. and Linden, P. (2002). Internal wave excitation by a vertically oscillating elliptical cylinder. *Physics of Fluids*, 14(2):721–731.

[Sutherland, 2010] Sutherland, B. R. (2010). *Internal gravity waves*. Cambridge University Press.

[Thorpe, 2005] Thorpe, S. A. (2005). *The turbulent ocean*. Cambridge University Press.

[Trossman et al., 2013] Trossman, D. S., Arbic, B. K., Garner, S. T., Goff, J. A., Jayne, S. R., Metzger, E. J., and Wallcraft, A. J. (2013). Impact of parameterized lee wave drag on the energy budget of an eddying global ocean model. *Ocean Modelling*, 72:119–142.

[Voisin, 1994] Voisin, B. (1994). Internal wave generation in uniformly stratified fluids. part 2. moving point sources. *Journal of Fluid Mechanics*, 261:333–374.

[Voisin, 2007] Voisin, B. (2007). Lee waves from a sphere in a stratified flow. *Journal of Fluid Mechanics*, 574:273–315.

[Voisin, 2016] Voisin, B. (2016). Lee wave generation in fourier space. *Private communication*.

[Von Kármán, 1963] Von Kármán, T. (1963). *Aerodynamics*, volume 9. McGraw-Hill New York:.

[Vosper et al., 1999] Vosper, S., Castro, I., Snyder, W., and Mobbs, S. (1999). Experimental studies of strongly stratified flow past three-dimensional orography. *Journal of Fluid Mechanics*, 390:223–249.

[Woods, 1985] Woods, J. D. (1985). The world ocean circulation experiment. *Nature*, 314(6011):501–511.

[Wurtele, 1957] Wurtele, M. G. (1957). The three-dimensional lee wave. *Beitr. Phys. Atmos*, 29:242–252.

[Wurtele et al., 1993] Wurtele, M. G., Datta, A., and Sharman, R. (1993). Lee waves: Benign and malignant. *Meteorology and climatology, NASA*.

[Zhao et al., 2016] Zhao, Z., Alford, M. H., Girton, J. B., Rainville, L., and Simmons, H. L. (2016). Global observations of open-ocean mode-1 m2 internal tides. *Journal of Physical Oceanography*, 46(6):1657–1684.